Master's Degree in Aerospace Engineering

Politecnico di Torino

SIEMENS energy

Master's Degree Thesis

Investigation of the Effect of Additive Manufacturing Induced Surface Roughness on Local Heat Transfer Properties Using IR Thermography

---

Candidate:
Alberto Brogliato
(s300275)

Supervisors:
Dr.-Ing. Mats Kinell
Prof. Gaetano Iuso

Thursday 25^{th} July, 2024

Acknowledgments

A Mauro e Caterina, i miei genitori, dai quali ho imparato l'importanza di porsi degli obiettivi.

A Sara, mia sorella, che mi ha insegnato a seguire sempre i miei valori.

A Benito, Lia, Giovanni e Adriana, i miei nonni, che mi hanno insegnato quanto la cultura e il lavoro nobilitino l'uomo.

A tutti quelli che hanno fatto parte della mia vita fin'ora dandomi sempre la possibilità di scoprire qualcosa di nuovo.

Ad maiora.

Declaration

I hereby declare that this thesis is my own work and effort and that it has not been submitted anywhere for any award. Where other sources of information have been used, they have been acknowledged.

Abstract

Additive manufacturing (AM), in particular laser powder bed fusion (L-PBF), enables the fabrication of more complex geometries compared to traditional manufacturing methods, such as casting or milling. This is beneficial in the development of cooling channels in high-temperature components of gas turbines (GT), as the thermal efficiency can be enhanced. A consequence of this manufacturing process is a high surface roughness (SR) influencing both pressure loss and heat transfer (HT). To gain a better understanding of forced convective HT on surfaces with AM-induced SR, the Surface-Roughness-Heat-Transfer rig (SRHT) has been built and employed in the *Fluid Dynamics Laboratory* at *Siemens Energy AB*. It allows the investigation of HT phenomena on an upscaled SR by means of infrared (IR) thermography using air as working fluid. In the current dissertation, a new SR upscaled model of an *Aluminium* test object has been developed and tested to obtain a spatial distribution of the heat transfer coefficient (HTC). The results have been compared with the smooth test objects and with previous results of the HTC over an *Inconel 939* model. After being at an initially uniform temperature, the surface was exposed to a sudden change in flow temperature and the heating was recorded by an IR camera (IRC). The local HTC was obtained by a thermal solver which allows to calibrate the measured surface temperatures over the rough plates and solve an optimization problem to iteratively find the correct HTC. The validation of the experimental methodology was conducted by investigating the HT in terms of the Nusselt number on a hydraulically smooth surface. Good agreement was found with the Gnielinski equation for the tested Reynolds numbers $Re = 10000$, $Re = 15000$, $Re = 20000$, and $Re = 25000$. The upscaled SR was modelled according to scanning electron microscope (SEM) pictures and roughness measurement data of a vertically printed channel made of *Aluminium*. For the applied scaling factor of 63.15 , the parameters R_a, R_z and R_q coincided well with the real scale channel. The model is also characterized by clusters of rough elements and wide smooth spots. The Aluminium SR model showed and increased HT with respect to the smooth plates. On the other hand, the HTC was clearly lower than the *Inconel 939*, which is char-

acterized by a high level of roughness. To gain a better understanding of the local HT enhancement, the ratio of the rough surfaces Nusselt over the smooth surfaces results have been plotted. This allowed to consider two main effects responsible for the HT enhancement: the direct impact of the air on the rough elements, and the turbulence induced by SR. Without any flow characterization, the main effect has been considered to be the direct impact of the air, with an enhancement of over 400% in the *IN939* at $Re = 25000$. The *Aluminium* showed a maximum enhancement of 165% for the same flow conditions. Further conclusions will be drawn after the Particle Image Velocimetry (PIV) investigations over the same test objects.

Table of Contents

List of Figures

List of Tables

Nomenclature

Abbreviations

AM	Additive Manufacturing
BB	Black Body
BL	Boundary Layer
CAD	Computer-Aided Design
CFD	Computational Fluid Dynamics
CT	Computed Tomography
DAS	Data Acquisition Systems
DMLS	Direct Metal Laser Sintering
FEM	Finite Element Method
FPS	Frame Per Second
GA	Genetic Algorithm
HT	Heat Transfer
IEA	International Energy Agency
IF	Internal Flow
IGT	Industrial Gas Turbine
IPCC	Intergovernmental Panel on Climate Change
IRW	Infrared Window
K-PDF	Kernel Probability Density Function

L-PBF	Laser Powder Bed Fusion
LBGT	Land-Based Gas Turbines
LDS	Lagrangian Droplet Simulator
MCM	Monte Carlo Method
PIV	Particle Image Velocimetry
QSSHT	Quasi-Steady State Heat Transfer
ROI	Region Of Interest
SEM	Scanning Electron Microscope
SLA	Stereolithography
SLM	Selective Laser Melting
SLS	Selective Laser Sintering
SR	Surface Roughness
SRHT	Surface Roughness Heat Transfer
STL	Standard Triangle Language
TIT	Turbine Inlet Temperature
TSM	Taylor Series Method
UA	Uncertainty Analysis

Greek Symbols

α_{air}	Thermal diffusivity of air	$[m^2\ s^{-1}]$
β	Pressure ratio	$[-]$
γ	Specific heat ratio	$[-]$
λ	Friction facotr	$[-]$
μ	Mean of Statistical Distribution	$[-]$
μ_{air}	Dynamic viscosity	$[Pa\ s^{-1}]$

ρ	Density	$[kg\ m^{-3}]$

Latin Symbols

$\dot{m}$	Mass Flow Rate	$[g\ s^{-1}]$
$\overline{h_0}$	Globally averaged heat transfer coefficient	$[W\ m^{-2}\ K^{-1}]$
$\overline{h}$	Laterally averaged heat transfer coefficient	$[W\ m^{-2}\ K^{-1}]$
$\overline{Nu_0}$	Globally averaged Nusselt	$[-]$
$\overline{Nu}$	Laterally averaged Nusselt	$[-]$
A	Duct cross section	$[m^2]$
C_p	Heat Capacity	$[J\ kg^{-1}\ K^{-1}]$
c_p	Specific heat at constant pressure	$[J\ kg^{-1}\ K^{-1}]$
c_v	Specific heat at constant volume	$[J\ kg^{-1}\ K^{-1}$
D_h	Hydraulic Diameter	$[-]$
h	Convective heat transfer coefficient enthalpy	$[W\ m^{-2}\ K^{-1}]$
k	Thermal conductivity	$[W\ m^{-1}\ K^{-1}]$
k_s	Relative sand grain roughness	$[-]$
k_{air}	Thermal conductivity of air	$[W\ m^{-1}\ K^{-1}]$
k_{ax}	Thermal conductivity through the layers	$[W\ m^{-1}\ K^{-1}]$
k_{rad}	Thermal conductivity along the layers	$[W\ m^{-1}\ K^{-1}]$
Nu	Nusselt	$[-]$
Nu_∞	Nusselt for thermally fully developed channel flows	$[-]$
Nu_r	Nusselt for rough surfaces	$[-]$
Nu_s	Nusselt for smooth surfaces	$[-]$
off	Spheres vertical offset	$[-]$
P	Perimeter	$[m]$

Pr	Prandtl	$[-]$
q	Specific heat	$[J\ kg^{-1}]$
R_a	Average Absolute Deviation from the Mean Line	$[\mu m]$
R_q	Roughness Heights Standard Deviation	$[\mu m]$
R_z	Maximum Peak to Valley Distance	$[\mu m]$
R_{ku}	Roughness Heights kutosis	$[-]$
R_{sk}	Roughness Heights Skewness	$[-]$
Re	Reynolds	$[-]$
S_μ	Sutherland Constant	$[K]$
$S_{\overline{x}}$	Standard Deviation of a Statistical Average	$[-]$
T	Absolute Temperature	[K]
T_∞	Mainflow Temperature	[K]
T_i	Initial Temperature	[K]
T_w	Wall Temperature	[K]
u_∞	Flow Velocity	$[m\ s^{-1}]$
w	Specific work	$[J\ kg^{-1}]$
x/D_h	Dimensionless streamwise coordinate	$[-]$

Chapter 1

Introduction

The introductory chapter outlines the motivation of this work, followed by a review of the literature regarding channel flows and cooling channels. Eventually, the objectives of the thesis will be presented.

1.1 Motivation

According to the International Energy Agency (IEA) , the demand for energy will double by 2030 due to the increasing population and the ongoing energy transition which affects the main energy-consuming sectors: electricity, industry, transport, and buildings. If the rising demand for energy is not counterbalanced by enhancements in energy efficiency in other areas [1], the global energy consumption will persist in its year-on-year growth. This escalating energy consumption amplifies

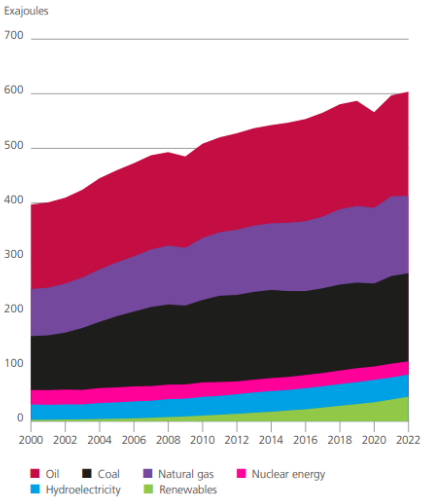

Figure 1.1: World Energy Consumption per source [2]

the complexities of transitioning our energy infrastructure from fossil fuels to en-

vironmentally friendly energy sources. Conversely, there is a growing imperative to minimize carbon footprint in order to achieve the target of net-zero emissions by 2050. The Intergovernmental Panel on Climate Change (IPCC) highlights the urgent need to curb CO_2 and NO_x emissions to mitigate greenhouse effects and set the warming limit at $1.5°C$. [3] While renewable energy sources play a vital role in addressing carbon emissions, challenges persist due to their intermittent availability and reliability. For instance, wind turbines may not generate power on still days, and solar panels may be less effective in regions with limited sunlight or at high latitudes. Despite the promising prospects of renewables, their unreliability necessitates the exploration of hybrid solutions, where green energy sources are combined with fossil fuel sources. In this context, Land-Based Gas Turbines (LBGT) emerge as a significant contributor to the energy supply, serving various purposes, such as meeting peak electricity demand or providing a continuous power source for baseload requirements. [4] LBGT are internal combustion engines that rely on the compres-

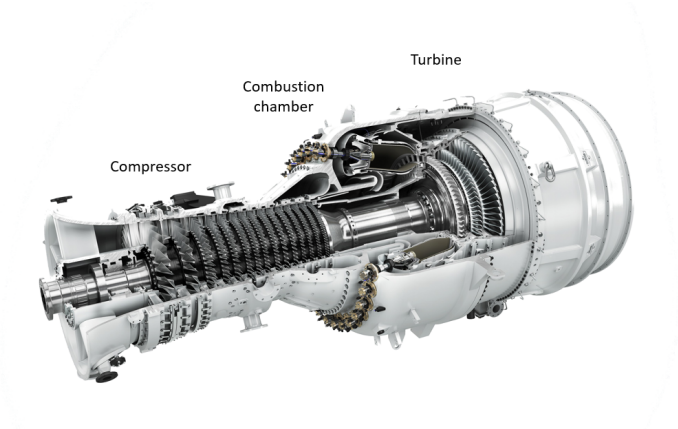

Figure 1.2: Siemens STG 800 gas turbine for power generation

sion of atmospheric air within a turbo-compressor, followed by its mixing with fuel and ignition within a combustion chamber. Subsequently, the resulting combustion gases expand through a turbine, generating power. Historically, Industrial Gas Turbines (IGT) have exhibited lower efficiency compared to their aerospace counterparts, leading to increased emissions and fuel consumption. However, over the past decade, there has been a notable improvement in the performance of IGT, reducing the technological disparity. This improvement can be attributed to the introduction of new coatings, advanced materials, and innovative cooling designs, which have significantly elevated the pressure ratio and Turbine Inlet Temperature (TIT) . [5] These advancements have resulted in a substantial enhancement of thermal efficiency. In modern gas turbines, TIT values can now reach over 2000 K, necessitating the implementation of effective cooling systems within turbine blades.

[6] Traditionally, these blades are manufactured using precision casting, limiting the complexity of the cooling duct geometry.

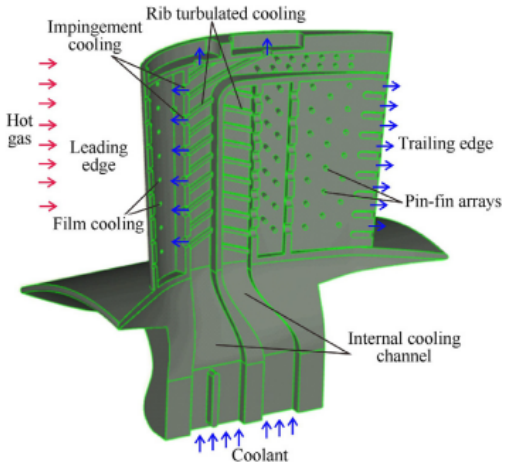

Figure 1.3: Scheme of general cooling techniques

However, the emergence of Additive Manufacturing (AM) has ushered in an era of more intricate cooling duct designs, enabling higher TIT levels. AM allows a layer-by-layer construction of turbine blades, in contrast to subtractive manufacturing methods, thereby enabling the creation of complex geometries and significantly reducing hot corrosion and material usage.[7] Currently, many AM techniques are available according to the material form, the energy source, and the build volume. For turbine blades, the most employed technique is based on Laser Powder Bed Fusion (L-PBF) of metal alloys, wherein a powder bed is spread in thin layers over a certain area, levelled through a re-coater blade, and melted by a laser beam in the near-infrared. After the exposure of the cross-section to the laser beam, the build plate is lowered and another layer of powder is spread and melted. [8]

Without going into detail, while AM can be beneficial for its design freedom and

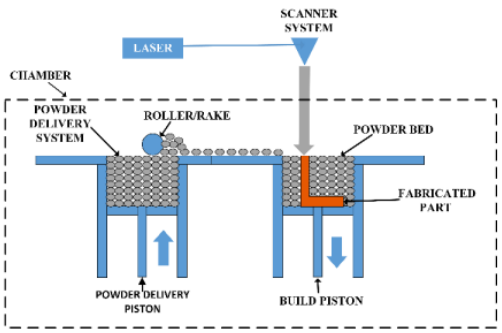

Figure 1.4: Schematic illustration of powder bed fusion methods for AM

the possibility to create fully integrated products by reducing the number of components, many limitations can be encountered such as the need to implement new alloys, and the inferior mechanical properties. Furthermore, the LPB-F process results in an increased level of Surface Roughness (SR) which can be post-processed in external surfaces to avoid a variation in aerodynamic performance but can not be removed from internal channels. This causes early boundary layer transition, increased momentum losses, and flow separation resulting in higher pressure losses. [9]. Even though AM doesn't seem to give a positive consequence from an hydrodynamic point of view, there is also a positive effect of augmenting convective HT of cooling channels with advantageous consequences on turbines' thermal efficiency. Yet, while there have been several experimental and Computational Fluid Dynamics (CFD) studies regarding momentum transfer and friction factor related to rough surfaces, the influence on Heat Transfer (HT) has not been fully comprehended, which leads to the motivation of the following study.

1.2 Literature Review

The effects of SR on the flow have been studied for decades. Numerous investigations regarding turbulent flow in smooth tubes, channels and over plates have been conducted[10] [11] [12], so that our knowledge on velocity distribution, mixing length, loss of head and friction factor have been increased. In particular, Nikuradse's [13] investigations on friction factor due to a relative sand grain roughness have paved the way for future studies on internal flows. The relative roughness, defined as $\frac{k_s}{D}$, where k_s is the diameter of sand grains sieved and adhered to the internal surface and D is the pipe's diameter, has been adopted in many works including Colebrook and White [14], as well as Moody [15], who generated the so called Moody diagram plotting the friction factor over Reynolds number and relative roughness. They eventually found a general pattern of the friction factor decreasing with Reynolds number and the rate of decrease becomes constant in the fully turbulent region. Furthermore, increasing the relative roughness the experiment showed an earlier transition to the fully turbulent region, consequently an higher friction factor. Although $\frac{k_s}{D}$ gives a great indication of the flow behaviour, one needs to take into account the significant difference between physical real roughness from measurements and the sand grain roughness, eventually trying to find the equivalent $\frac{k_s}{D}$ when doing experimental investigation over SR. Many works try to find a correlation between roughness properties, such as the root-mean-square of heights, and the respective sand grain roughness, but more research has to be done to define a consistent relative roughness

parameters. The literature is rich on experiments and investigation of flow features over rough surfaces. Latest studies and literature reviews have been carried out by Kadivar [9] and Bons [16], with an in-depht understanding of the flow behavior especially on external flows for different type of artificial roughness. In these works several correlation to understand the most influencing roughness parameters have been presented. An experimental work has been carried on by Yi Zhu et al. [17] where a corrected Colebrook model is used while plotting the result of the friction factor over Reynolds for different channels fabricated il Selective Laser Melting (SLM) . They showed a matching pattern in the laminar region where the friction factor λ follows the trend $\lambda = \frac{64}{Re}$, and after the transition the flow seems to be suddenly fully turbulent. Overall, the AM introduces an increased roughness, which can be described by several standard parameters. This increased roughness brings to higher friction factors (even for the laminar region), so that a modified version of Colebrook's law needs to be used. While this pattern has been fully understood, there is still lack of knowledge in the way to describe the roughness parameters which best represent the relative roughness, thus more work needs to be done in this direction.

Despite the importance of flow features and friction factor, the aim of this work is to study the HT over additively manufactured surfaces, especially giving a local perspective of HT over rough elements. In the last decades, numerous studies have been conducted regarding the variation of Nusselt number with Reynolds and Prandtl numbers in circular ducts, for both homogeneus fluids and fluids with changing properties. On this purpose, many different correlations have been found, for various ranges of Reynolds and Prandtl, to relate $Nu - Re - Pr$ in laminar and fully turbulent flows. It has been understood that an increased wetted area can bring a proper convective HT enhancement. In the same way, AM dramatically increases HTC, but varying materials and building direction, thus varying the surface roughness, can lead to unexpected results. So, HT needs to be studied with a local perspective, focusing on rough elements and how they interact with fluid to understand the thermal behavior. On this purpose, Rastan et al. [18] investigated the heat transfer characteristics of minichannel-based heat exchangers with longitudinal vortex generators. The test objects printed in *ALSI10Mg* using *DMLS* had an hydraulic dyameter of 2.86 mm and water was used as a medium. The experimental data had been validated and the results for rough channels with vortex generators showed a dramatic increas in HT. On the other hand, still a lot of research needs to be done in order to understand the main reasons of the HT enhancement related

to AM. Thanks to a novel method to implement random rough surfaces based on a Lagrangian Droplet Simulator (LDS) [19], Clemenson et al. [20] were able to perform heat transfer analysis on an analogue rough surface to study the effects of ice accretion on heat transfer on an air-foil. The ice roughness topographies have been unwrapped in the streamwise direction and the surface has been analysed to get the main parameters [21] in order to reproduce and up-scale it. The real and analogue surfaces were statistically confronted and the equivalent sand-grain was predicted using Flack and Schultz [22] correlation. The HT analysis was performed through an IR camera and showed an enhancement of HT over roughness elements. The same approach has been followed by Hanson [23], who developed an up-scaled model of a cooling channel produced in AM. Hanson used x-ray Computed Tomographies (CT) and a LDS to developed the analogue surface focusing on two main ideas: the analogue surface needs to be multi-spectral and the convective and shear enhancements are due to vortex shedding created by roughness elements and the interaction of the eddies with the downstream SR. The research was mainly on flow friction but paved the basis for future comprehension of convective HT enhancements. Moreover, it has been made clear the importance of modelling an analogue rough surface that is representative of the statistical properties of the real one. Further studies on HT in additively manufactured cooling channels have been done by Stimpson et al [24][25]. Different coupons made with Direct Metal Laser Sintering (DMLS) , all having multiple rectangular channels, were evaluated obtaining friction factor and Nusselt number with significant augmentation compared to smooth channels. An important overview regarding turbulent flow over additively manufactured rough surfaces has been presented by Reza [9], where a deep understanding of flow behavior and CFD results can be found.

Several studies for HT on cooling channels can be found in literature, especially regarding nuclear reactors, but a poor literature about local behaviour of HT in upscaled SR of cooling channels highlights the amount of research that has yet to be done.

1.3 Research Objectives

The thesis explores the challenges and advancements associated with the application of AM in the production of turbine blades, specifically studying the local thermal characteristics of upscaled rough surfaces from additively manufactured cooling channels. At the Fluid Dynamic LAB of Siemens Energy AB in Finspång,

research has been conducted for several years on this subject, using a Quasi-Steady State Heat Transfer (QSSHT) rig to investigate real size cooling channels to understand how friction factor and Nusselt number, critical dimensionless parameters in heat transfer and fluid dynamic analysis, vary with respect to Reynolds number and Prandtl number. The study involves micro-channels of different length and diameter, manufactured from different materials including *Aluminium*, *Inconel 939*, and *Stainless Steel* with various printing direction. Both water and air are used as medium, because water's Prandtl number is more sensitive to temperature changes. The correlation found for the friction factor over Re aligns with in literature behaviour, but the ones for Nu over Re and Pr for different materials have shown some critical variations that need to be investigated.A proper dimensionless parameter that describe the SR and the consequent influence on λ and Nu hasn't been fully understood yet. For instance, finding out what are the most relevant roughness parameters that influence HT enhancement can be a key aspect to tailor the materials and the printing direction in order to obtain most effective results. The detailed description of the QSSHT rig is provided in Lehmann [26].

While the QSSHT rig provides valuable averaged data related to thermal and flow behaviour, it has limitations when it comes to local heat transfer information. To address this, a Surface Roughness Heat Transfer (SRHT) rig has been designed, with a focus on understanding the convective heat transfer coefficient and Nusselt number over specific areas of the surface, such as roughness elements and surface valleys. The objective is not only to gain insights into how and why increased surface roughness, as achieved through AM techniques, can be advantageous for enhancing heat transfer efficiency, but also understanding which are the most influencing roughness parameters on HT enhancement. Lehmann [26] assembled and used the SRHT rig for validating the convective HT of a smooth surface. A coarse analogue rough surface was then developed from the Scanning Electron Microscope (SEM) measurement data of a micro-channel made of *Inconel 939*, manufactured by LPB-F at a vertical printing direction (90°). The performed investigation gave promising results, showing augmented HT on rough elements, particularly on the upstream surfaces, and the influence on downstream elements. The research has been carried on by Wen [27], who noticed some issues on the development of the analogue rough surface, and corrected the main parameters and statistical distribution of the surrogate surface in order to match those of the real surface. By doing so, he obtained more coherent results with the QSSHT rig. The outline of his work was the improvement of the surrogate rough surface and the use of a Siemens Energy's

built in solver *C3D* to perform wall temperature calibration for the rough surface. The difference with Lehmann stems from the mathematical model used to solve the thermal equation for rough surfaces. Firstly, a 1D conduction model, i.e. Duhamel's superposition theorem, was used to calculate the heat transfer coefficient both for smooth and rough surface. This is correct for the smooth surface, but many features where lost when resolving the rough plates. Consequently, an in-house adjoint thermal solver for inverse problems (*C3D*) was used to solve 3D transient heat transfer with convective boundary conditions. Wen also presented some interesting insights of the thermal behaviour of smooth plates positioned after rough plates, to understand the influence of the turbulence over rough elements on the HT enhancement.

In the course of the present work:

1. An up-scaled model of surface roughness from SEM pictures of a Aluminum coupon will be modeled replicating the most important statistical features of the real rough surface. More specifically, two surfaces with different matching roughness parameters will be developed. An optimization algorithm will be developed in order to match the roughness parameters;

2. Heat Transfer study using Infrared Thermography will be carried out to obtain the local HTC. This will help understanding the impact of rough elements in the heat transfer enhancement. In particular, the smooth channel will be investigated to validate and get some data useful for a comparison with in literature correlations; in the same way, the rough plates will be studied and the results will be compared with *IN939* roughness plates. The local heat transfer enhancement will be calculated by comparing the smooth channel results with the rough channel;

1.3.1 Thesis Outline

- Thorough theoretical background on gas turbine performance, channel flows, additive manufacturing, heat transfer and dimensionless analysis will be provided;
- The experimental investigation will be described in detail taking into account the setup, the development of an analogue rough surface, and the measurements of convective HT using IR thermography;
- Post-processing of wall temperature data to obtain local heat transfer coefficient with the related theory will be highlighted.
- Discussion of results and presentation of future work will be shown.

Chapter 2

Theoretical Background

The experimental investigation objectives, presented in Section 1.3, needs to be backed-up by a thorough look into the fundamental theory. Firstly, it is important to get the basic knowledge of the GT thermodynamics and the State-Of-Art of cooling channels to understand the reasons why AM is applied to produce turbine blades. Consequently, a brief presentation of AM techniques for turbine blades production and the induced effect on SR are needed to understand how we can reproduce an analogue surface from roughness measurement. Afterwords, Internal Flows HT and Fluid Dynamics must be underlined to understand the physical problem and present the numerical way to solve it, but also to understand why AM gives such a great enhancement in HT phenomena. Eventually, some basic concepts of Infrared Termography are described to understand how to measure wall temperature in the test rig. All in all, these aspects will be valuable to proceed in the experimental study of convective HT over an upscaled model of SR created by SEM roughness measurement, and they will be used to explain all the phases of the experiments: from data acquisition to the outcome of the results.

2.1 Gas Turbine

Among various means of power generation, GT excel for their reliability, availability and versatility over different range of power generation as shown in Table 2.1.

Internal combustion turbines are generally air breathing thermal engines where the working fluid (i.e. air) passes firstly through an intake and a compressor, where pressure and temperature rise. The hot air is then mixed with fuel and ignited inside the combustion chamber where energy of the working fluid is increased. The power generation comes from the expansion of the hot working fluid which occurs in the turbine. An exhaust will conduct the combustion gases in open air or, if the GT is

GT	Power Production
Heavy-Duty	$3 \div 480\ MW$
Industrial Type GT	$2.5 \div 15\ MW$
Small Gas Turbines	$0.5 \div 2.5\ MW$
Micro-Turbines	$20 \div 350\ kW$

Table 2.1: Classification of GT regarding the power output

part of a Combined Cycle Power Plant, they will be used for steam generation or as heating source for other purposes, such as heating buildings.

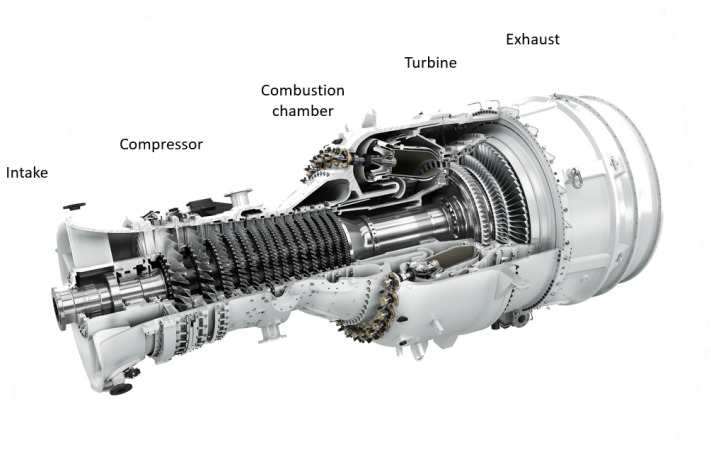

Figure 2.1: STG 800 components' visualization. The GT is produced by Siemens Energy AB

The thermodynamic process of a GT can be ideally represented through the Brayton-Joule cycle. This simple overview of the working principle is satisfying to understand the main parameters influencing the thermal efficiency of the GT, but for a thorough comprehension further information can be found in literature [28] [5] [29].
The four main processes of the simple open-cycle GT for power production can be described following the steps in Figure 2.3 representing the absolute temperature $[K]$ in function of the Specific Entropy $[J\ kg^{-1}\ K^{-1}]$.

There are several assumptions that must be taken into account: (1) the air mass flow is greater than the fuel mass flow $\dot{m}_a \gg \dot{m}_f$, (2) the gas is calorically and thermally perfect, which means there are not variations in the specific heat at constant pressure c_p and in the specific heat at constant volume c_v , so that the specific heat ratio $\gamma = \frac{c_p}{c_v}$ is constant during all the cycle, (3) all the components

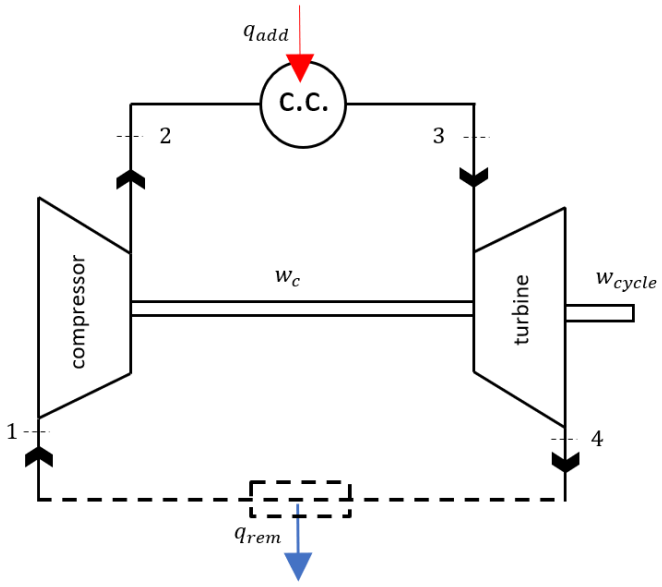

Figure 2.2: Schematic representation of a gas turbine

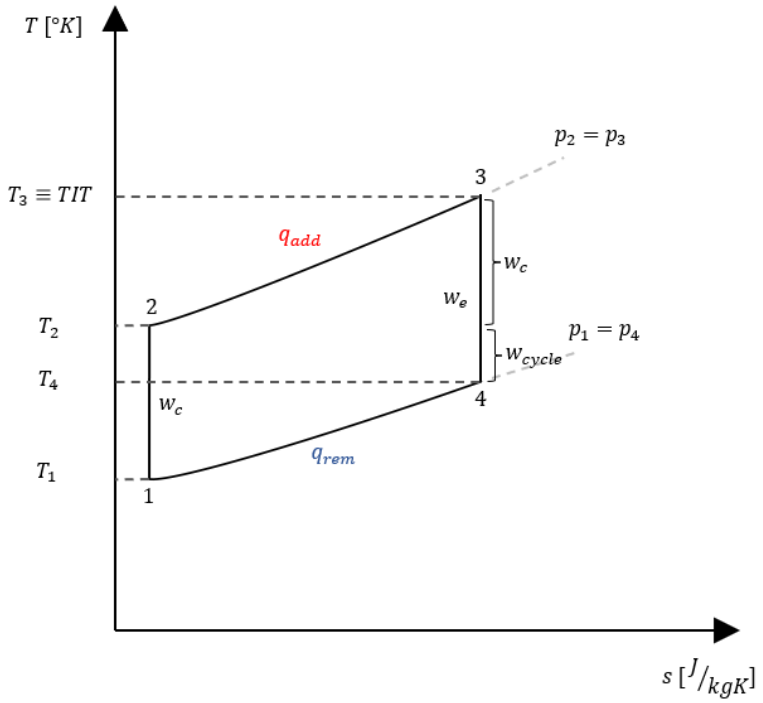

Figure 2.3: Brayton-Joule cycle represented in a diagram of absolute temperature over specific entropy

operate at efficiency of 100%, (4) the turbine and the compressor have same pressure ratio $\beta_c = \beta_t$. With these hypothesis, the air proceeds with the following cycle:

$1 \longrightarrow 2$ Adiabatic, quasi-static and isentropic compression in the compressor. The specific work input to drive the compressor is given by the difference between specific enthalpy of steps 2 and 1:

$$\begin{aligned} w_c &= h_2 - h_1 \\ &= c_p(T_2 - T_1) > 0 \qquad \left[\frac{J}{kg}\right] \end{aligned} \tag{2.1}$$

$2 \longrightarrow 3$ Isobaric combustion in the combustion chamber. The constant pressure specific heat addition is given by the difference between specific enthalpy of steps 3 and 2:

$$\begin{aligned} q_{add} &= h_3 - h_2 \\ &= c_p(T_3 - T_2) > 0 \qquad \left[\frac{J}{kg}\right] \end{aligned} \tag{2.2}$$

$3 \longrightarrow 4$ Adiabatic, quasi-static and isentropic expansion in the turbine with consequent specific work production w_e:

$$\begin{aligned} w_e &= h_4 - h_3 \\ &= c_p(T_4 - T_3) < 0 \qquad \left[\frac{J}{kg}\right] \end{aligned} \tag{2.3}$$

$4 \longrightarrow 1$ Isobaric specific heat removal to cool the air to its initial condition:

$$\begin{aligned} q_{rem} &= h_1 - h_4 \\ &= c_p(T_1 - T_4) < 0 \qquad \left[\frac{J}{kg}\right] \end{aligned} \tag{2.4}$$

As it can be seen in Figure 2.3 the isobaric lines at $p_1 = p_4$ and $p_2 = p_3$ tend to diverge. Thus the work produced with the expansion is greater than the work to drive the compressor. This is the reason why part of the expansion work is used to drive the compressor while the rest is used to generate power $w_e = w_c + w_{cycle}$. For instance, the net specific work is $w_{cycle} = |w_e - w_c|$.The objective now is to get the thermal efficiency of the cycle.

Accordingly with the first law of thermodynamic, which is a formulation of the law of conservation of energy, the change in specific internal energy Δu is equal to the difference between the amount of specific heat q applied or removed and the specific work done or released by the system w:

$$\Delta u = 0 = q_{rem} + q_{add} + w_c - w_e \tag{2.5}$$

So the net specific work produced by the cycle is

$$w_{cycle} = q_{rem} + q_{add} \tag{2.6}$$

Thus, the overall cycle efficiency, considering the correct sign of the added and removed specific heat, is

$$\begin{aligned} \eta_{cycle} &= \frac{w_{cycle}}{q_{add}} \\ &= \frac{q_{add} + q_{rem}}{q_{add}} \\ &= 1 - \frac{c_p(T_4 - T_1)}{c_p(T_3 - T_2)} \\ &= 1 - \frac{T_1(T_4/T_1 - 1)}{T_2(T_3/T_2 - 1)} \end{aligned} \tag{2.7}$$

Considering the hypothesis (4) and considering the isentropic relations for a perfect gas:

$$\begin{aligned} \beta_c &= \frac{p_2}{p_1} = \left(\frac{T_2}{T_1}\right)^{\frac{\gamma}{\gamma-1}} \\ \beta_t &= \frac{p_4}{p_3} = \left(\frac{T_4}{T_3}\right)^{\frac{\gamma}{\gamma-1}} \end{aligned} \tag{2.8}$$

Giving $\beta_t = \beta_c^{-1}$, we can find

$$\frac{T_1}{T_2} = \frac{T_4}{T_3} \qquad \longleftrightarrow \qquad \frac{T_4}{T_1} = \frac{T_3}{T_2} \tag{2.9}$$

So the thermal efficiency can be expressed as a function of the T_3, that is the TIT, or of the compressor pressure ratio:

$$\begin{aligned} \eta_{cycle} &= 1 - \frac{T_4}{T_3} \\ &= 1 - \left(\frac{1}{\beta_c}\right)^{\frac{\gamma}{\gamma-1}} \end{aligned} \tag{2.10}$$

As it can be seen in the Figure 2.4 from [5], the cycle efficiency increases with the increasing TIT while the effect of the pressure ratio is firstly dramatically beneficial, but then this effect tend to diminish. Thus, the object of this study is carried on for the importance of the thermal enhancement that AM is bringing to the GT. In fact, it allows to improve the cooling of turbine blades resulting in higher working TIT.

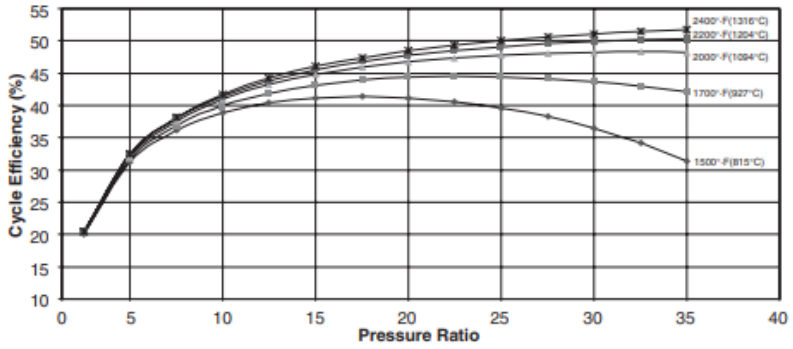

Figure 2.4: Cycle efficiency as function of the compressor pressure ratio and the TIT

2.2 Cooling structures in Turbine Blades

Turbine blades convert the kinetic energy of the hot air and combustion gases mixture to create shaft power. In the 1950's, uncooled blades where used reaching temperatures of around $1000 - 1100\ °K$. Two decades later, with new technologies and materials development, TIT could be around $1300 - 1500\ °K$. Nowadays, the TIT of gases can reach over $2000\ °K$ requesting an effective cooling system to increase thermal efficiency and diminish hot corrosion, prolonging the lifetime of turbine blades.[30] [6] [31].

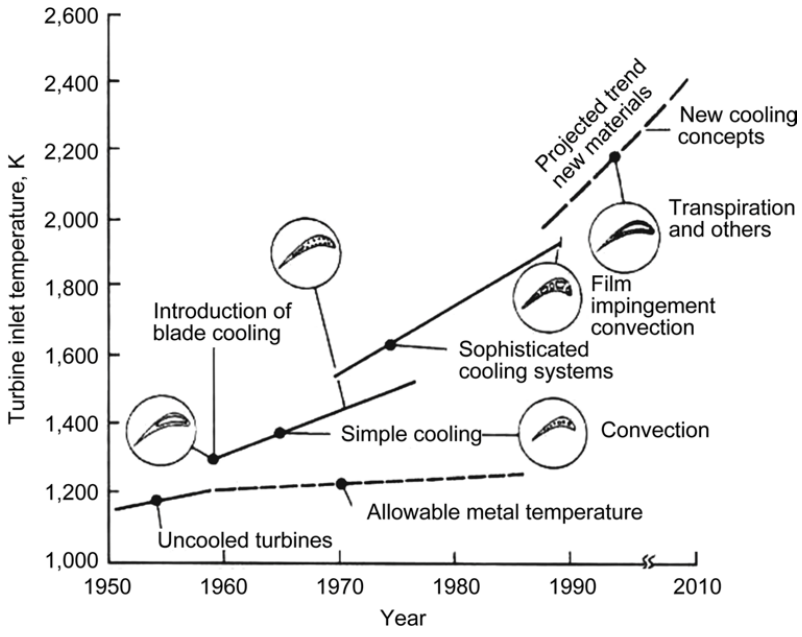

Figure 2.5: TIT variation during the last decades in function of different cooling techniques

Therefore, in the following section the main cooling techniques will be presented. It must be remarked that temperature on a blade can vary from the leading edge

to the trailing edge, and also from the root to the tip. The maximum temperature is in the stagnation point. These key aspects require tailored cooling techniques depending on the working point of the GT.

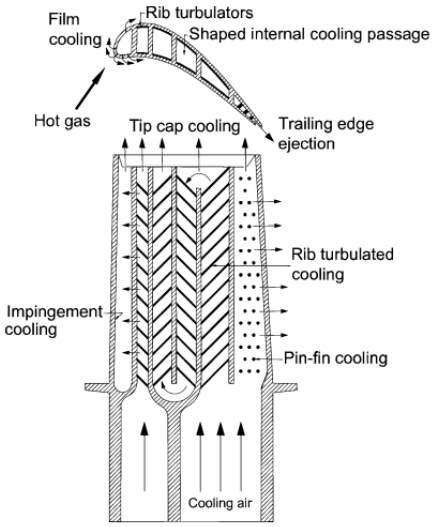

Figure 2.6: Schematic view of cooling techniques. Above: the horizontal section shows internal vanes with holes for film cooling. Below: a vertical section shows the internal vanes for impingement cooling. [32]

2.2.1 Internal Blade Cooling

For this technology, internal vanes are used to cool the blades from inside. Complex geometries can be developed especially using AM [6], resulting in larger available surface, thus in a greater HT. The coolant, i.e. liquids or air, removes heat through convection and impingement.

2.2.1.1 Convection Cooling

Air or liquids flow inside internal cooling ducts. Heat is transferred first via conduction, and then via convection from the material to the coolant. The advent of AM has deeply influenced geometries and HT surfaces regarding this technique.

2.2.1.2 Impingement Cooling

Where temperature reaches high values, such as in the stagnation point at the leading edge, air is blown in the inner part of the turbine hitting the surface to remove a substantial thermal load. After impinging on the internal walls of the

airfoil, the coolant continue its path inside internal vanes toward the trailing edge, acting like a film layer to remove heat.

2.2.2 Film Cooling

Air from compressor stages is bled and channelled to the internal chambers of turbine blades and then released from small holes in the blade wall. This creates a thin layer of cool air which acts as an insulating coat.

2.2.2.1 Discrete Film Cooling

The working principle lays on the creation of a thin cool boundary layer to prevent hot air to be directly in contact with the surface. Thanks to some active holes positioned in a discrete pattern, the cold air is released over the external surface of the airfoil. [33]

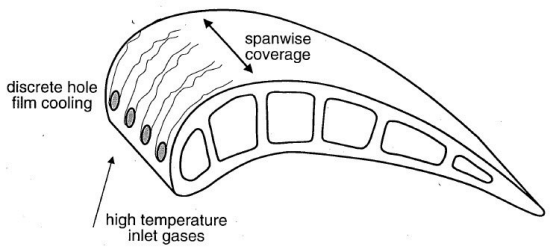

Figure 2.7: Discrete Film Cooling

2.2.2.2 Full Blade Film Cooling

The cooling principle is the same as before, but there is a variation in the positions of the holes. For instance, they are distributed more continuously and they allow to merge the cool air in the turbulent boundary layer.

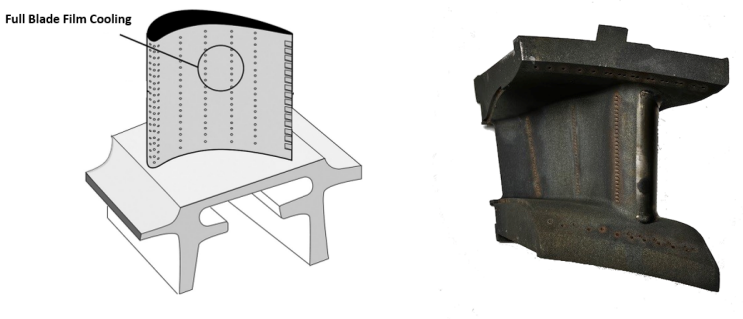

Figure 2.8: Full Blade Film Cooling: the holes are on the entire turbine blade [34] [32]

2.3 Additive Manufacturing

AM can be broadly defined as a manufacturing technique which allows to turn a 3D CAD model into a physical product by slicing the digital model into several 2D cross-sections used to build the final model layer-upon-layer (Figure 2.9). The four main components comprehend a digital model, material in form of powder, wire or liquid droplets, a machine to create the cross-section layers and a control system to build the 3D shape. During the last decade, AM has gained more attention from numerous industry sectors, such as Car Industry, Aerospace, Medicine, Sports Industry and Construction Industry.[35] Although conventional manufacturing processes, such as forging and machining, will always maintain their significant roles, the emergence of AM has opened up new possibilities particularly within the domain of Land Based Gas Turbines. As mentioned in previous sections, AM enables the creation of complex designs for internal turbine blade cooling, thereby enhancing the overall cycle efficiency, reducing fuel consumption, and increasing power generation capabilities. Consequently, comprehending the core principles of AM constitutes a key aspect of this thesis. Replicating an upscaled analogue surface of AM cooling channels necessitates a fundamental understanding of SR measurement parameters and AM techniques employed in the production of turbine blades.

A wide range of AM technologies is available, each tailored to specific applications. A fundamental differentiation exists between polymer-based and metal-based AM methods. A comprehensive examination of these techniques can be found in existing literature, but it falls beyond the scope of this thesis [36].

However, it is important to give a thorough description of L-PBF due to its role in the fabrication of turbine blades and GT components.

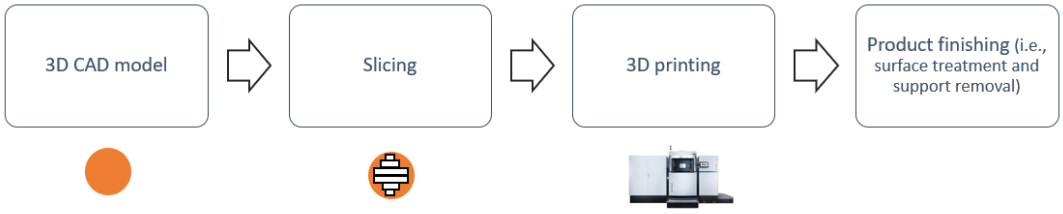

Figure 2.9: Schematic flowchart of the AM process: from design of the component to the finished part.

2.3.1 Laser Powder Bed Fusion (L-PBF)

Nowadays, the most widely spread technique to produce turbine blades and other GT components is L-PBF [1]. The process consist in:

- Creation of a three-dimensional (3D) Computer-Aided Design (CAD) model;
- Conversion of the 3D model into a *.STL* file and the generation of two-dimensional (2D) layers, ranging from 20 μm to 1 mm, using specific computer software;
- Application of a layer of powdered material onto a substrate plate or an already processed layer;
- Precise melting of the powdered particles by directing a high-energy laser beam along the contours of the current layer;
- Lowering of the base plate and addition of another layer of powder;
- Repeating the above steps in a cyclic fashion until the entire model is complete;
- Performing an accurate post-processing such as a surface treatment process, where applicable, and supports separation.

The main advantages of using L-PBF are the possibility of using bed powder as an integrated support, a large range of material options, and its relatively cheap

[1] There is no difference between DMLS, Selective Laser Sintering (SLS) , Selective Laser Melting (SLM) and L-PBF because they all refer to the same technique. Despite the *ISO 529000* group these techniques as Powder Bed Fusion - Laser Beam, this therm is unwieldy and L-PBF is of most common use

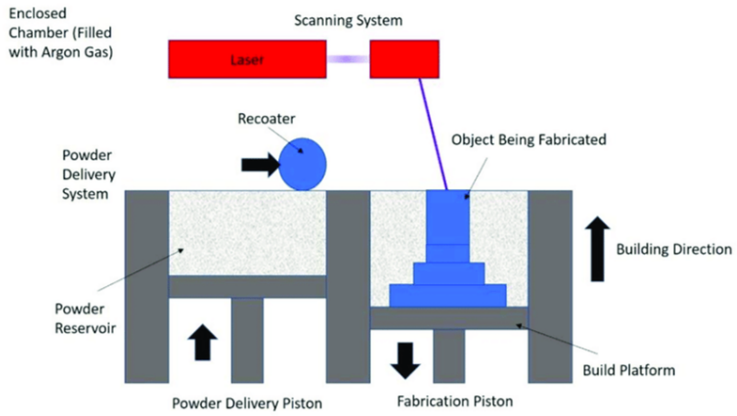

Figure 2.10: Schematic representation of the printing process for L-PBF [37]

implementation with respect to other metal-based techniques. Conversely, the main drawbacks are related to the lack of structural integrity, size limitations, long printing time and the poor surface finishing.

2.3.1.1 Printer

The 3D printer used at *Siemens Energy AB* to produce various components as well as the coupon for the QSSHT rig, later used to create the upscaled analogue SR of the SRHT rig, is the *EOS M 400 Series*. The printer comprehend a printing volume of maximum $400 \times 400 \times 400\ mm^3$, a laser with a maximum power of 1000 W, and a side box for taking out the support and preliminary finishing procedures of the component. [38] The use of different materials or different process parameters can affect the product in its surface finishing, i.e. the surface roughness. For instance, the same material can present huge differences in the surface finishing related to the building angle of the component. For the purpose of this thesis, it is fundamental to describe the main roughness parameters and to give a rough explanation of analogue surface modelling methods.

2.3.2 Surface Roughness

AM objects are usually characterized by a high level of roughness, but generally, every surface, even the smoothest one, is characterized by a certain level of roughness due to geometrical irregularities that can be randomly distributed over the surface. The frequency of these irregularities define the type of surface roughness or surface texture, which can be considered as *"Roughness"* if the frequency is high, or *"Waviness"* if the frequency is medium. When the frequency is low the geometry

Figure 2.11: EOS M 400-4 model used at *SIemens Energy AB*

is no longer considered as a surface texture and takes the name of *"Surface form"*, indicating the proper shape of the surface of an object.[9]

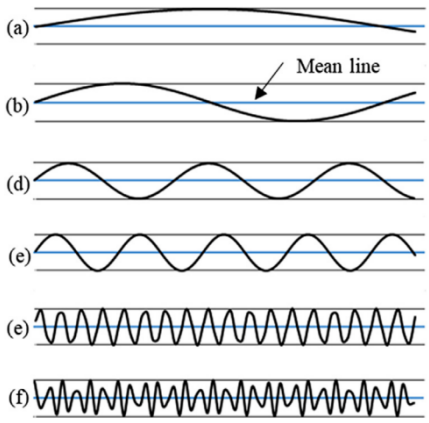

Figure 2.12: Surfaces with different frequencies: (a),(b) surface form; (c),(d) waviness; (e),(f) roughness

The surface roughness is quantifiable and can be calculated along a sampling line or over a sampling area. The parameters defined along a sampling line are more common and can be found in the `ISO 4287:1997` norm. In the following section, the main statistical roughness parameters will be presented. The method used to create an analogue surface model will be presented in Section 3.1, along with the measurement technique used during this thesis.

2.3.2.1 Surface Roughness Parameters

The mentioned ISO standard for roughness parameters describe several statistical properties of a rough surface. The most important features are presented in Table 2.2.

Parameter	**Description**	**Statistical implementation**
R_a	Arithmetic average of profile height deviation from the mean line	$\frac{1}{l_r}\int_0^{l_r} \lvert z(x)\rvert dx$
R_q	Root-mean-square roughness	$\sqrt{\frac{1}{l_r}\int_0^{l_r} z(x)^2 dx}$
R_p	Maximum peak height above the mean line, within a single sampling length	$\sum_{i=1}^{5} \frac{max_i(z(x))}{5}$
R_v	Maximum valley depth under the mean line, within a single sampling length	$\sum_{i=1}^{5} \frac{min_i(z(x))}{5}$
R_z	Average of the five maximum peak to valley height of the profile	$\sum_{i=1}^{5} \frac{R_{p_i}+R_{v_i}}{5}$
R_{sk}	Skewness	$\frac{1}{R_q^3}\left[\frac{1}{l_r}\int_0^{l_r} Z(x)^3 dx\right]$
R_{ku}	Kurtosis	$\frac{1}{R_q^4}\left[\frac{1}{l_r}\int_0^{l_r} Z(x)^4 dx\right]$

Table 2.2: Some of the main roughness parameters in the ISO 4287:1997 standard

For the purpose of this thesis it is interesting to understand what are the most influencing parameters on heat transfer. In fact, the sole use of R_a to describe the surface can lead to some thermo/fluid dynamics misinterpretations, since different surface textures can have the same R_a, but different R_q, R_{sk}, and R_{ku} can lead to a different behavior of the fluid and thermal boundary layer.

The skewness represents the shape of the topography height distribution and it is zero when the heights distribution is like a Gaussian, but it can also be negative or positive. A surface with large valleys and high peaks irregularities, such as deposition on surface during laser sintering, is characterized by $R_{sk} > 0$, while a surface with large peakes and deep valleys, such as corrosion, has $R_{sk} < 0$ as it can be seen in Figure 2.13.

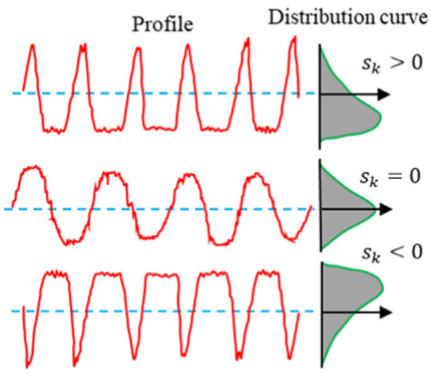

Figure 2.13: Skewness distribution type

The kurtosis is a measure of the sharpness of the surface height distribution. If $R_{ku} = 3$ the distribution is referred to as a Gaussian, while $R_{ku} < 3$ is known as a Platykurtoic distribution where there are few high peakes and low valleys. An $R_{ku} > 3$ is representative of a Leptokurtoic distribution with many high peakes and low valleys. Figure 2.14 shows different kind of distributions.

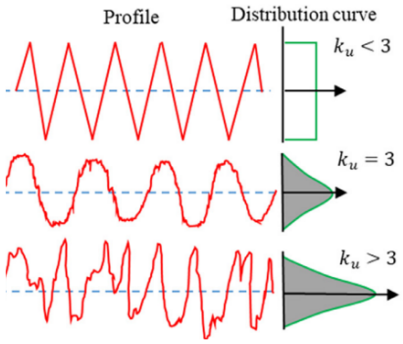

Figure 2.14: kurtosis distribution type

2.4 Fundamentals of Heat Transfer

In [39], the author delves into specific explanations to the main questions that might arise when studying heat transfer: *What is heat transfer? How is heat transferred? Why is it important?* The objective of this thesis is not to accomplish such an ambitious task, but to cover the basics of heat transfer in order to offer a general point of view useful to understand the outline of this project.

2.4.1 Definition of Heat Transfer

Heat transfer is a thermal energy transfer created by a spatial temperature difference. This means that whenever a temperature gradient is present, heat transfer occurs. There are three different modes it can occur: when a temperature gradient exists in stationary media, such as solid or fluid, it is referred to **conduction**. When a temperature gradient occurs between a moving fluid and a surface we refer to **convection**, while we refer to **thermal radiation** when the heat transfer is in form of electromagnetic waves scattered by a surface at a given temperature.

Before delving into each type of heat transfer, it is important to explain a general concept valid for every case. In the most general case, the heat transfer occurs in a system as in Figure 2.15. System A and System B interact through an exchange area. The heat transfer is characterized by some border conditions, such as: Dirichelet condition with a fixed temperature at the border, or Neuman condition with a fixed heat flux at the border, or both conditions in more rare cases known as Cauchy border conditions. The primary objective will be to get the heat transfer between

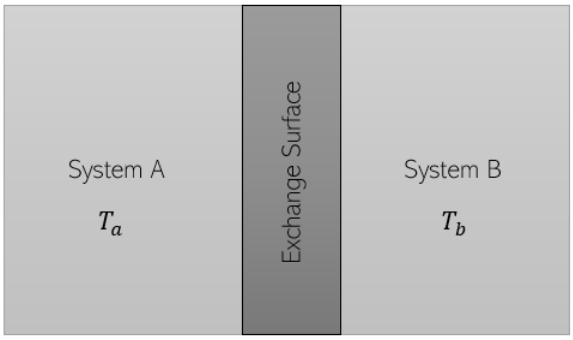

Figure 2.15

the interface of the systems, but also the temperature distribution in the exchange area is a secondary objective. [40]

2.4.1.1 Conduction

Conductive heat transfer takes place in solids or fluids with one main constraint: no macroscopic motion. This is the case of solids, fluids confined in thin places or fluids in micro gravity conditions. The main reason for conductive heat transfer is directly found in particles motion (atoms and molecules). For instance, the temperature at any point of a system can be associated with a certain energy level. The higher the temperature the higher the energy level. Thus, when two systems with different

energy levels, i.e. two different temperatures, are positioned one next to the other, the particles of each system will interact with each other, because the particles move randomly and tend to collide exchanging energy. The flux of energy, i.e. conductive heat transfer, will always go from warmer to colder systems. The heat transfer rate can be quantified by the Fourier law, recognizing that the conductive heat transfer occurs always perpendicularly to the surface of exchange. Without going into any demonstrations, the general Fouriers law states as follows:

$$q = -k\nabla T = -k(i\frac{\partial T}{\partial x} + j\frac{\partial T}{\partial y} + k\frac{\partial T}{\partial z}) \tag{2.11}$$

The conductive heat transfer takes place in every direction when there is a gradient of temperature in that direction. The temperature is, in fact, function of the spatial position $T(x, y, z)$.The constant k is known as thermal conductivity $[W\ m^{-1}\ K^{-1}]$ and represents a thermophysical property of the material. The negative sign in front of the equation denotes that the conductive heat flux is discord with respect to the normal of the surface of exchange, remembering that for the Second Principle the heat goes always from hotter to colder regions.

2.4.1.2 Convection

Convective heat transfer is characterized by two main mechanisms: one is the same as in conduction and has already been mentioned as diffusion taking place at a molecular level, while the other is related to the macroscopic motion of the material. For this simple reason, convective heat transfer occurs in fluids with given temperature gradients. Convective heat transfer can be classified according to the nature of the flow. We refer to forced convection when the flow field is caused by external means, such as a fan. Natural convection, on the other hand, is the case in which the flow field is created as consequence of internal buoyancy forces related to density differences (caused by temperature variations in the fluid). Usually, natural convection occurs in low speed flows or still flows in contact with a surface at different temperature.

An important case of study, useful to understand the convective heat transfer phenomena, is the flow over a heated plate. The motion of the fluid over the surface causes the development of a velocity boundary layer. In the same region, a thermal boundary layer develops due to the temperature gradient and the motion of the fluid. The heat is swept downstream by the moving fluid, while in correspondence of the surface the energy diffuses. Forced convection is prevalent in high speed flows and will be the main reason for heat exchange.

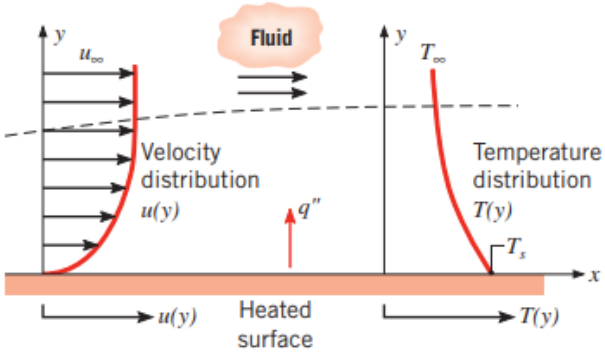

Figure 2.16: Velocity boundary layer and thermal boundary layer development over a heated surface [39]

Convective heat transfer can be expressed, regardless from the nature of convection, by Newtons law of cooling:

$$q = h(T_\infty - T_w) \tag{2.12}$$

where the heat flux $[W\ m^{-2}]$ is proportional to the difference between the main flow temperature and the surface temperature, and to the parameter h $[W\ m^{-2}\ K^{-1}]$ known as the convective heat transfer coefficient. The coefficient depends on the boundary layer, which is itself influenced by the surface geometry, fluid properties, etc.. as it will be better explained in the dimensionless analysis.

2.4.1.3 Radiation

The radiative heat transfer is a phenomena related to electromagnetic fields, which requires only the presence of moving charges and can take place in solids, fluids, and in vacuum. As an antenna generates electromagnetic waves thanks to oscillating charges, in a system with electrons and protons the same can happen, generating radiative heat transfer. This occurs as long as the temperature stays above the absolute zero. The wavelength of the emitted energy depends on the level of energy that the body contains, i.e. from the temperature of the body. Without digging into the main theory about emitted and received signals, it is important to know that there is a difference between the emitted energy and the received energy. Considering valid the antenna analogy, an antenna can emit in certain range of frequencies, but receive in a different one.

The four most important quantities in radiation are listed as follows [40]:

- Global emission: represents the emitted power by a surface for all the frequen-

cies and in all the directions

$$E = \frac{dq}{dA} \tag{2.13}$$

- Monochromatic emission: represents the emitted power by a surface for a single range of frequencies and in all the directions

$$e_\lambda = \frac{dq}{dAd\lambda} \tag{2.14}$$

- Global irradiation intensity: it's the amount of power irradiated in a given direction for all the frequencies

$$I_\delta = \frac{dq}{dAd\omega cos\theta} \tag{2.15}$$

- Monochromatic irradiation intensity: it's the amount of power irradiated in a given direction for a range of frequencies

$$i_{\delta,\lambda} = \frac{dq}{dAd\lambda d\omega cos\theta} \tag{2.16}$$

Considering all the directions and all the wavelengths, and dq_a, dq_r, dq_τ the absorbed heat flux, reflected heat flux and transmitted heat flux respectively, the global optic coefficients can be calculated as follow for a given surface:

$$\begin{cases} \alpha = \frac{dq_a}{dq} \\ \varrho = \frac{dq_r}{dq} \\ \tau = \frac{dq_\tau}{dq} \end{cases} \tag{2.17}$$

These coefficients represent how much power is absorbed, transmitted and reflected by a body irradiated by a certain flux dq.

The Black Body hypothesis

Considering the model of black body (BB), the global absorbing coefficient is ideally equal to 1.

$$\alpha = 1 \tag{2.18}$$

Since the sum of the coefficients is equal to one, for a BB there is neither reflection nor absorption. By Equation 2.18 the receiving behavior of a BB is totally characterized, because every incident radiation will always be absorbed. Furthermore, the emission

of a BB can be easily characterized recognizing that, for the Kirkhoff law, the emission is equal to the absorption coefficient

$$\varepsilon = \alpha \tag{2.19}$$

For BB it is possible to find an analytical solution for the monochromatic irradiation, known as Planck's law for BB:

$$i_{\delta,\lambda} = \frac{b_1}{n^2\lambda^5\left[exp\left(\frac{b_2}{\lambda T}\right) - 1\right]} \tag{2.20}$$

where T is the absolute temperature, n is the refraction index of the mean of radiation, while b_1 and b_2 are two constants with the values of $b_1 = 1.19096\ 10^{-16}$ $[W\ m^{-2}\ sr^{-1}]$ and $b_2 = 1.43879\ 10^{-2}$ $[K\ m]$. For a given value of temperature, and medium ($n = 1$ in vacuum), the monochromatic irradiation is only function of the wavelength, with the typical Gaussian behavior as in Figure 2.17.

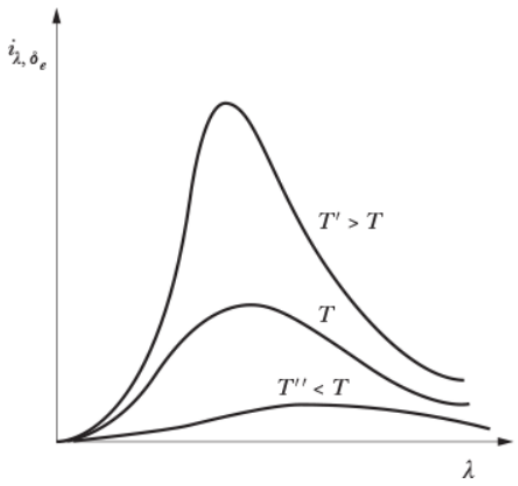

Figure 2.17: Planck law for monochromatic irradiation

If the temperature increases also the monochromatic irradiation will increase. For BB also the monochromatic emission will have the same behavior as the monochromatic irradiation.

$$e_\lambda = \pi i \tag{2.21}$$

From this, it can be understood that a BB emits in all directions in all the wavelengths. The maximum emission occurs at a given wavelength, that can be calculated by Wien law:

$$\lambda^* = \frac{b_3}{nT} \tag{2.22}$$

where $b_3 = 2897.8$ $[\mu m\ K]$.
The global emission can be calculated integrating in all the wavelengths as in Figure

2.18 , and it is known as Stefan-Boltzmann law:

$$\begin{aligned} E &= \int_0^\infty e \, d\lambda \\ &= n^2 \sigma T^4 \end{aligned} \tag{2.23}$$

with $\sigma = 5.67\ 10^{-8}\ [W\ m^{-2}\ K^4]$ known as the Stafan-Boltzmann constant. Every BB is characterized by a certain emission, which is directly proportional to the temperature of the body.

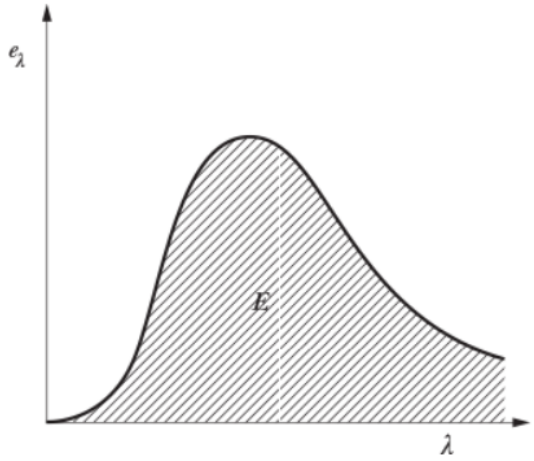

Figure 2.18: Global emission

2.5 Infrared Termography

Infrared Thermography, also known as thermal imaging, is a non-contact technique that uses infrared imaging and measurement cameras to visualize and measure thermal energy emitted from an object. Thermal energy, or heat, is light that is not visible to the naked eye, because its wavelength is too long to be detected. It's the part of the electromagnetic spectrum (Figure 2.19) that we perceive as heat.

IR cameras can capture this light and create a digital image based on information about the temperature differences. The technique is based on radiative heat transfer theory, which has been explained in depth in the previous section, giving more insights on BB assumption. Every wavelength is generally associated with a certain level of emitted thermal energy, which means that also in infrared bands there is always an emission. The monochromatic emission, characterized as e_λ for BB, represents the emitted energy for a given wavelength. In real bodies the emission is far from the BB, as it can be seen in Figure 2.20, thus in IR thermograpy it

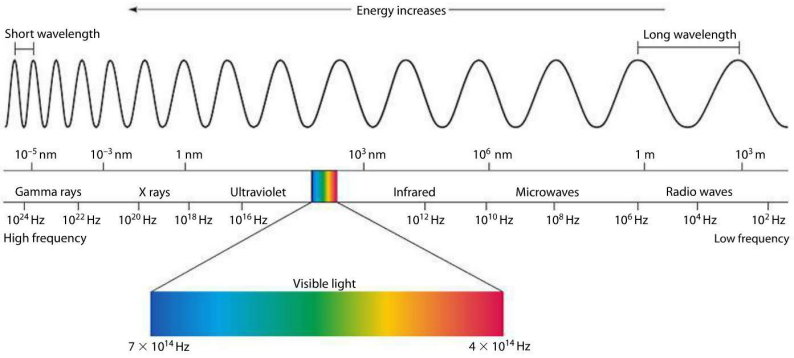

Figure 2.19: Electromagnetic spectrum

is important to introduce the monochromatic emissivity coefficient for real bodies, given by the emission of a real body over the emission of a BB:

$$\epsilon_\lambda = \frac{e_\lambda}{(e_\lambda)_n} \tag{2.24}$$

In IR thermography, the concept of monochromatic emissivity coefficient is more

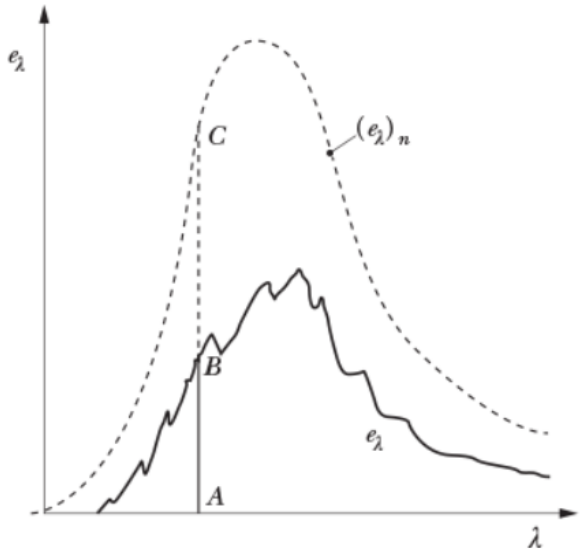

Figure 2.20: Emissivity of real bodies

important than the global emissivity coefficient $\epsilon = \frac{E}{(E)_n}$, because the IR sensors detect only certain ranges of wavelength in a given IR band (NIR, MIR, EIR). In fact, IR detectors are made of thermal energy-sensitive materials, which convert the IR energy in an electrical voltage or current. These are typically photon detectors in which the electrons release is associated with the material level of sensitivity. The performance depends on various factors, which can be expressed as function of thermal sensitivity (noise level), scan speed, image resolution and intensity resolution. They are very sensitive to temperature changes, thus they need a proper

cooling system. Furthermore, they are affected by external disturbances, such as warm bodies in proximity or material positions in between the target body and the sensor.
Since the accuracy of the measurements depends on the calculation of the emissivity of the surface (which is not a BB) it is important, in first instance, to evaluate this parameter.

On a broad level, IR cameras are based on the detection of a radiometric signal corresponding to the energy released by the body. Through a precise calibration of the camera, which will be explained in Section 3.2, the electrical signal can be translated in temperature, to give the spatial representation of the wall temperature.

2.6 Internal flows

As opposed to external flows where the boundary layer is free to develop over a surface without any constraint, in internal flows, such as in pipes, the fluid is constrained, influencing the boundary layer development. Internal flows can be found in many applications, such as heating or cooling ducts. For the purposes of this thesis, it is essential to understand the fundamentals of internal flows in order to better understand the problem of convection. However, the specific thermal solver for the smooth and rough surfaces will be explained in depth in Section 3.4.
The objective of this section is to give a general description of the phenomena from both fluid and thermal dynamic point of view, in order to appreciate the physical behavior and obtain convection coefficients for different flow conditions. Firstly, the velocity features of the flow will be considered, presenting the typical boundary layer development inside channels. In the second part, the thermal boundary layer will be analyzed to determine the convection heat transfer coefficient and the correlations typical of internal flows.

Before delving into the fluid-thermal dynamics of the problem, it's important to present a dimensionless analysis, which will provide the main dimensionless parameters to study internal flows.

2.6.1 Dimensional Analysis and Similarity

Dimensional analysis is a very powerful tool used in numerous fields of study. When approaching an experimental study, one will soon understand the large variety of

parameters influencing the results. Hence, it would be both time and money consuming to carry out experiments varying all the influencing parameters. Furthermore, it is often impossible to test real size objects, such as a full-scale airplane. What is generally used to avoid these problems is the principle of dynamic similarity, which can be stated as follows: if the model and prototype are in geometric similarity, i.e. the prototype is an in scale model, and the independent dimensionless parameters are the same, then also the dependent dimensionless parameters are comparable.

2.6.1.1 Incompressible, Viscous Flow in a Horizontal Pipe with Convective Heat Transfer

This case of study is representative of the conditions investigated in the course of this thesis. The dimensionless analysis must be carried out on a pipe where there are hydrodynamic and thermal effects. Hence the problem will be decomposed into an hydrodynamic dimensionless analysis and a convective heat transfer dimensionless analysis.

1. **Hydrodynamic Similarity**: the main interest in this case is the pressure drop between the inlet and outlet of a pipe. The pipe is geometrically characterized by a length l, an hydraulic diameter D_h and a roughness identified generally by k; the flow properties are the density of the fluid ρ, the dynamic viscosity μ and the bulk velocity u_m. Hence, the pressure drop will be a function of all this parameters, but the explicit form of this correlation has to be determined.

$$\Delta p = f(l, D_h, k, \rho, \mu, u_m) \tag{2.25}$$

   Finding a correlation at this point would mean to carry out a huge quantities of experiments, in fact, choosing around five values for each variable would lead to 10^6 experiments. To simplify the problem, the number of parameters have to be reduced. To accomplish such an ambitious problem, one of the most powerful techniques used is the Π-*Theorem of Buckingham* [41]: if N is the number of dimensional physical quantities and K is the number of fundamental quantities, there can be $N - K$ dimensionless groups Π_i to study the problem. This will dramatically reduce the number of variable, thus the number of experiments that need to be carried out. In our case of study there are $N = 7$ dimensional physical quantities and $K = 3$ fundamental quantities (i.e. mass M, length L and time T). Using the Buckingham Theorem the dimensionless parameters in which the problem can be reduced are in total $7 - 3 = 4$. The calculation of the four dimensionless group is made by using the $\Pi_i -$*Theorem*

and leads to the similarity numbers in Equation 2.26

$$\begin{cases} \Pi_1 = & \frac{\Delta p}{\frac{1}{2}\rho u_m^2} \\ \Pi_2 = & \frac{l}{D_h} \\ \Pi_3 = & \frac{k}{D_h} \\ \Pi_4 = & \frac{u_m \rho D_h}{\mu} \end{cases} \tag{2.26}$$

Consequently, the functional dependence 2.25 can be translated into the dimensionless dependence

$$g(\Pi_1, \Pi_2, \Pi_3, \Pi_4) = const \tag{2.27}$$

and solving for the dimensionless pressure drop Π_1, and considering $\Pi_4 = Re$

$$\frac{\Delta p}{\frac{1}{2}\rho u_m^2} = F(\frac{l}{D_h}, \frac{k}{D_h}, Re) \tag{2.28}$$

If there is a fully developed pipe flow, F must be linear function of $\Pi_2 = \frac{l}{D_h}$, thus the well known friction factor parameter λ will only be a function of Reynolds and the relative roughness.

$$\lambda = \frac{\Delta p/l}{\frac{1}{2}\rho {u_m}^2/D_h} = \lambda(\frac{k}{D_h}, Re) \tag{2.29}$$

Thus, the role of the experiments will be to find a correlation between these dimensionless parameters and the number of experiments will be drastically reduced. Being in geometric similarity and hydrodynamic similarity will be important to compare experimental data of a prototype with the real full-scale test object.

2. **Convective Heat Transfer Similarity**: when studying the convective heat transfer the focus is usually on the convective heat flux q, instead of the heat Q itself. Considering the problem of a pipe, interested by a hot air streaming in it with a certain velocity, the main role is played by forced convection. Natural convection, in fact, is negligible when the velocity is high. (A better explanation about the difference between forced and natural convection can be found in Section 2.4.1.2) Therefore, the most significant variables influencing the resulting heat flux in forced convection are the following:

   - The geometry of the duct, D_h;
   - The extension of the heat transfer surface, A;

- The temperature distribution over the surface on the interface, T_w;
- The bulk main flow temperature distribution, T_∞
- The velocity field, u;
- The fluid properties: thermal conductivity k, specific heat at constant pressure c_p, density ρ, dynamic viscosity μ.

  Considering a fixed geometry and the parameters independent from the temperature, the forced convective heat transfer can be expressed by a functional relation:

$$|q| = f(A, L, T_w, T_\infty, k, c, \rho, \mu, u) \tag{2.30}$$

  It is not excluded to add other parameters if needed, but this must be taken into account during all the experiments and also in the dimensionless analysis. For now, the functional relation presented previously will be considered. Finding the correlation between all the parameters in Equation 2.30 needs a lot of work, probably not worthy a life. In fact, the number of experiments to find a correlation, taking into account five different values for each variable will lead to around $10 \cdot 10^6$ experimental measurements. To simplify the problem one can assume the relation between the heat flux and the other variables a priori. Isaac Newton's relation was proposed long time ago, but it is still valid today and consider the convective heat flux $[W\ m^{-2}]$ directly proportional to the surface area, the arithmetic difference between T_∞ and T_w [40]:

$$|q| = h(T_w - T_\infty) \tag{2.31}$$

  where h is the heat transfer coefficient for forced convective heat transfer $[W\ m^{-2}\ K^{-1}]$. This hypothesis presented by Newton is not based on any physical law, but will be evaluated by the end of experiments. The convective heat transfer coefficient h is function of:

$$h = f(D_h, k, c, \rho, \mu, w) \tag{2.32}$$

  In this way, the number of experiments will be reduced, but still it's not enough to be satisfactory. Once again, the Π-*Theorem of Buckingham* is an helpful tool, which allow to reduce the number of variables acting a main role in the experiments. Without delving into the specific demonstration, the main dimensionless parameters in this case are the

following:

$$\begin{cases} \Pi_1 = & \frac{hD_h}{k} \\ \Pi_2 = & \frac{c_p\mu}{k} \\ \Pi_3 = & \frac{\rho u D_h}{\mu} \end{cases} \tag{2.33}$$

The three dimensionless groups are respectively the Nusselt number, Prandtl number, and Reynolds number:

$$\begin{cases} Nu = & \frac{hD_h}{k} \\ Pr = & \frac{c_p\mu}{k} \\ Re = & \frac{\rho u D_h}{\mu} \end{cases} \tag{2.34}$$

Hence, the correlation for forced convection will be in the form:

$$f(Nu, Pr, Re) = 0 \tag{2.35}$$

If a generic variable x_i plays an important role in the experiment, and it has to be taken into account in the convective heat transfer it can be added to the functional relation. For example, in convective heat transfer in cooling channels also the friction factor λ can play an important role as well as the geometry l/D_h.

Elaborating the results from the experiments some correlations can be found and expressed in the form:

$$Nu = f(Pr, Re) \tag{2.36}$$

If also the friction factor and the geometry parameters are playing a major role:

$$Nu = f(Pr, Re, \lambda, \frac{l}{D_h}) \tag{2.37}$$

2.6.2 Fluid Dynamics of Internal Flows

The hydrodynamic boundary layer of an Internal Flow (IF) is forced to develop within a constrained region. Generally, the first section of the duct is characterized by the development of the boundary layer. Considering a laminar flow entering a duct, as soon as the flow makes contact with the surfaces, the viscous effects

begin to affect the flow. As a consequence to viscosity, the inviscid region shrinks downstream, until the viscous effects merge all over the section of the duct and the velocity profile remain constant along x. When this happens, the flow is considered fully developed and the distance from the inlet at which this is achieved is the hydrodynamic entrance length, $x_{fd,h}$.

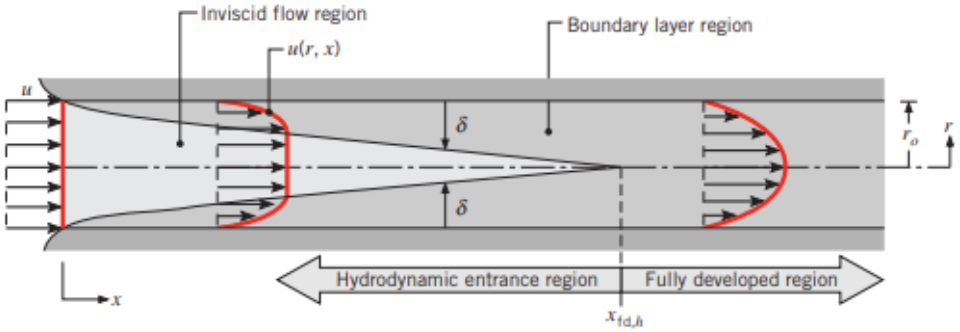

Figure 2.21: Hydrodynamic boundary layer development in a circular pipe

In this regions, for symmetric ducts, the velocity profile has a maximum at the center and then the velocity diminish toward the walls, where the non-slip condition is respected. The extent of the entrance length depends on the Reynolds number of the flow, which is calculated with the bulk velocity u_m, the hydraulic diameter D_h, and the cinematic viscosity ν:

$$Re = \frac{u_m D_h}{\nu} \tag{2.38}$$

Although there is not a general equation to express the entrance length in function of the Reynolds, it is known that its value increases with the increasing Re, and the values can be approximated as

$$10 \lesssim \left(\frac{x_{fd,h}}{D_h}\right) \lesssim 60 \tag{2.39}$$

The value of the Reynolds number is also responsible for the flow regime in the duct. For example, for a circular duct:

- $Re < Re_{critic} = 2300$: laminar regime;
- $2300 < Re < 10^5$: low turbulence regime;
- $Re > 10^5$: fully high turbulent regime.

The critic Reynolds number identifies the transition from laminar to turbulent flow. In a duct with different cross sections these regimes are not addressed in the same Reynolds intervals, thus they need to be determined. However, the three regimes

are always present.

For a steady state laminar flow ($\partial u/\partial t = 0$), in the fully developed region, where the velocity profile is fixed, the momentum conservation in the streamwise direction can be applied taking into account that only pressure and wall shear stress are acting, and there are not inertia forces.

$$\frac{\partial u}{\partial x} = 0 \tag{2.40}$$

For a rectangular duct, with height similar to the width, the force balance on a control volume as in Figure 2.22 is expressed by Equation 2.41

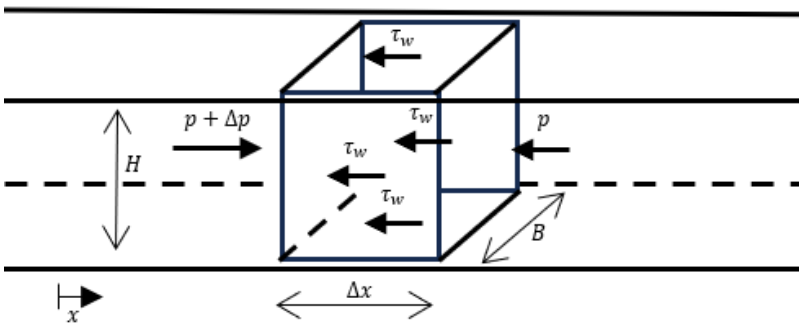

Figure 2.22: Infinitesimal control volume inside the rectangular cross section channel

$$(p + \Delta p)BH - pBH - 2\tau_w \Delta x B - 2\tau_w \Delta x H = 0 \tag{2.41}$$

From Equation 2.41, the wall shear stress can be expressed as

$$\tau_w = \left|\frac{\Delta p}{\Delta x}\right| \frac{BH}{2(B+H)} \tag{2.42}$$

On the other hand, the main interest in channel flows are the pressure losses. As already explained in Section 2.6.1.1 the dimensionless parameter representing pressure losses is the friction factor λ, calculated as in Equation 2.43

$$\lambda = \frac{-dp/dx}{\frac{1}{2}\rho u_m^2 / D_h} \tag{2.43}$$

where the bulk velocity should be calculated as the integral mean

$$u_m = \frac{1}{H}\int_0^H u(y)\, dy \tag{2.44}$$

In engineering applications, it is common to work with the so called Moody diagram, which is a representation of the friction factor as function of the Reynolds number and a relative roughness parameter. For instance, in channel flows it is a main point of interest to find proper correlations, such as

$$\lambda = \lambda\left(Re, \frac{\varepsilon}{D_h}\right) \tag{2.45}$$

For example, in circular smooth pipes the three regimes are identified as:

- Laminar regime: $\lambda = \frac{64}{Re}$
- Low turbulence regime: $\lambda = \frac{0.32}{Re^{1/4}}$
- Fully high turbulence regime: $\lambda = \frac{0.12}{Re^{1/6}}$

In channel flows with different cross sections and a certain level of relative roughness, a different correlation between dimensionless parameters has to be found. The result is usually plotted in the Moody diagram 2.23, where it can be seen that for a given

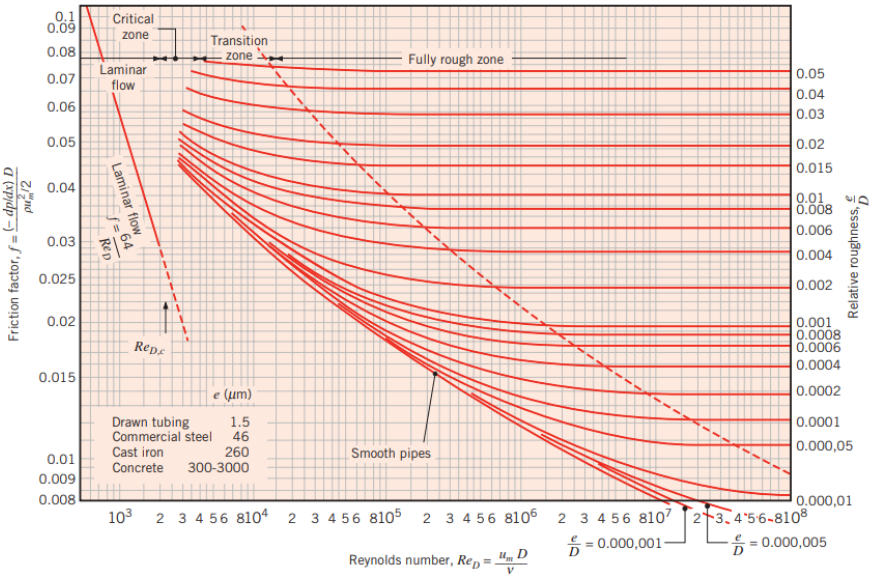

Figure 2.23: Friction factor for circular tubes with varying relative roughness

level of relative roughness, the flow begins as laminar for low Reynolds, it undergoes transition at a given Re_{critic} and reaches the region of low turbulence where the friction factor changes at increasing Reynolds, and eventually reaches a plateau in the high turbulence level. Increasing the level of relative roughness, the high turbulence level is reached at lower Reynolds numbers. Furthermore, the parameter used to describe the relative roughness is not easy to identify if the roughness is random and not uniformly distributed, as it can be seen in Figure 2.24.

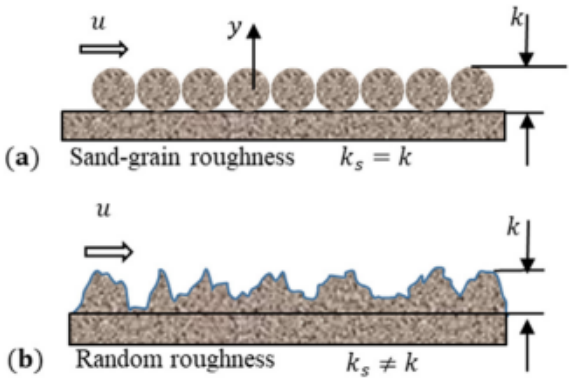

Figure 2.24: Difference between uniformly distributed roughness and randomly distributed roughness

In fact, many experiments has been carried out by Nikuradse, Moody and Colebrook [13] [14] to find a correlation between $\lambda - Re - k_s/D_h$, where k_s is identified as the sand grain roughness, i.e. the diameter of sand grains adhered to the channel surface to conduct the experiments. Yet, for random surface roughness, the sand grain roughness cannot be applied, thus the relative roughness is generally referred to a roughness parameter or a correlation between several of them. For example, Flack and Shulz [22] suggested $\frac{k_s}{D_h} = 18(R_a/D_h) - 0.05(R_a/D_h)$ for additively manufactured surfaces, but the discussion on this topic is still ongoing and there is not a real correlation that is completely accepted.
It is then important to clarify the difference between different flow regimes. For the sake of clarity, the turbulent boundary layer (BL) theory is needed. The turbulent BL is divided into an inner layer and an outer layer. In the inner layer there are three more regions: viscous sublayer in contact with the surface, buffer layer, and logarithmic layer in contact with the outer layer. Considering a randomly distributed roughness, the three regimes can be described as follows:

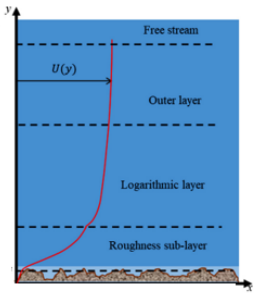

Figure 2.25: Turbulent Boundary Layer representation

- Laminar region: as it can be seen in Figure 2.26a the rough elements are fully

embedded in the viscous sublayer. In this case the skin friction is mainly given by the viscous action of the flow over the surface;

- Low turbulence region: Figure 2.26b shows how the rough elements are still embedded in the viscous sublayer, but its thickness is greatly reduced creating an increased friction, which can be related to both viscous and pressure forces acting on the roughness;
- High turbulence region 2.26c: the rough elements protrude in the viscous sublayer generating a great increase in skin friction. The protrusion of the roughness generate a mixing turbulence which is then responsible for pressure forces acting on the roughness. The pressure losses are no longer varying with the velocity and the viscosity of the fluid. The Reynolds number, which the high turbulence region begins at, decreases with increasing relative roughness.

(a) Laminar regime

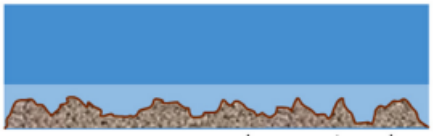

(b) Low turbulence regime

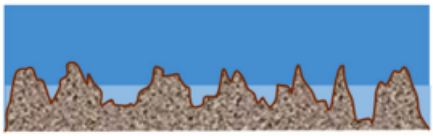

(c) High turbulence regime

Figure 2.26: Different flow regimes

2.6.3 Heat Transfer of Internal Flows

After a deep understanding of the hydrodynamic of internal flows, the thermal effects are presented.

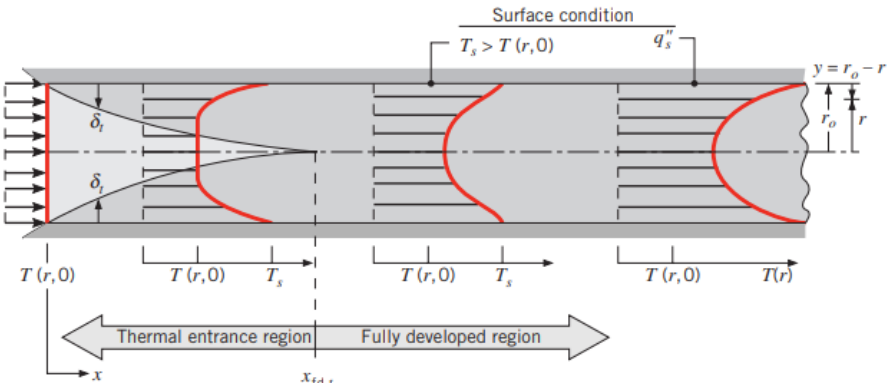

Figure 2.27: Thermal boundary layer development in ducts

When a fluid enters a duct with a uniform temperature T_0, convective heat transfer occurs and the temperature profile develops. The boundary condition on the duct's surface can be a constant temperature T_s or a constant heat flux q_s''. In the first section of the duct the shape of the temperature profile starts to change, due to the interaction with the surface. Considering a warmer surface, i.e. $T_s > T(r,0)$, or a heat flux that heats up the fluid, the temperature is higher on the surface and decreases until reaching the initial value. The more downstream, the more the temperature profile section with $T(r) = T_0$ shrinks, until reaching a point downstream in which there is not a value of initial temperature in the whole temperature profile. This region is known as thermal entrance length $x_{fd,t}$. Further downstream, the temperature profile depends on the boundary condition, as it can be seen in Figure 2.27, and it is called thermal fully developed region.
For laminar flows, the thermal entry length can be expressed as

$$\left(\frac{x_{fd,t}}{D_h}\right)_{lam} = 0.05 Re_D Pr \tag{2.46}$$

For turbulent flows, a good approximation is

$$\left(\frac{x_{fd,t}}{D_h}\right)_{turb} = 10 \tag{2.47}$$

In the **thermally fully developed region** the fluid temperature continues to change downstream, thus one can question why it is called so if none fully developed thermal condition is eventually reached. In fact, as opposed to the hydrodynamic

problem where $\partial u/\partial x = 0$ in the fully developed region, for the thermal fully developed region there is not such a condition in which $\partial T_\infty/\partial x = 0$. Conversely, the temperature profile continues to change, but working with a dimensionless form of the temperature, such as $(T_s - T)/(T_s - T_\infty)$, a formal condition for thermally fully developed flow can be stated as in Equation 2.48

$$\frac{\partial}{\partial x}\left[\frac{T_s(x) - T(r,x)}{T_s(x) - T_\infty(x)}\right]_{fd,t} = 0 \tag{2.48}$$

The temperature ratio is not only indipendent with x. In fact, the derivative with respect to r is independent of x. Thus

$$\frac{\partial}{\partial r}\left[\frac{T_s - T}{T_s - T_\infty}\right]\Bigg|_{r=r_0} = \frac{-\partial T/\partial r\big|_{r=r_0}}{T_s - T_\infty} \tag{2.49}$$

From the Fourier's law $q_s'' = k\frac{\partial T}{\partial r}\big|_{r=r_0}$, leading to

$$\frac{h}{k} \neq f(x) \tag{2.50}$$

Thus, in the thermally fully developed region with constant properties of the flow, the HTC is constant and does not depend on the streamwise coordinate. This is not satisfied in the entry region were the HTC varies with x, being very high at the beginning and decaying rapidly as the thermal boundary layer develops, until it reaches the value associated with the fully developed region, as it can be seen in Figure 2.28

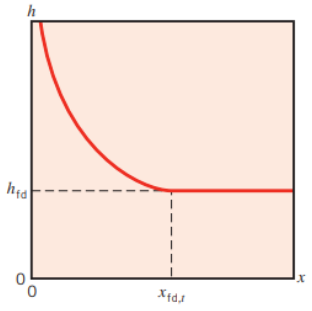

Figure 2.28: Streamwise variation of the HTC for duct flows

While studying convection in the fully developed region with turbulent flow, the main interest is to determine empirical correlations between dimensionless parameters $Nu - Re - Pr$. As explained in the dimensionless analysis, convection is a complicated field to investigate experimentally, thus simplifying the problem reducing the number of variables is helpful to avoid wasting time in too many experiments.

The empirical correlations regard the main dimensionless parameters and have their range of use in terms of flow conditions. For instance, Dittus-Boelter Equation is valid for fully developed (hydrodynamically and thermally) turbulent flows in smooth circular tubes with $0.6 < Pr < 160$, $Re > 10000$, $\frac{L}{D_h} > 10$

$$Nu = 0.023\ Re^{4/5}\ Pr^{n} \tag{2.51}$$

The uncertainty related to Equation 2.51 may result in 25%, but other correlations can be used to reduce the uncertainty, even though they can be more complex. A correlation for smooth ducts over a large number of Reynolds (including the transition region) is provided by Gnielinski:

$$Nu = \frac{(\lambda/8)(Re - 1000)Pr}{1 + 12.7\sqrt{\lambda/8}(Pr^{2/3} - 1)}\left[1 + \left(\frac{D_h}{L}\right)^{2/3}\right]K \tag{2.52}$$

where the friction factor can be determined from the Moody diagram or using Equation 2.53, and the coefficient K is given by Equation 2.54

$$\lambda = (1.84 \cdot log_{10}Re - 1.64)^{-2} \tag{2.53}$$

$$K = (T_b/T_w)^{0.45} \tag{2.54}$$

Gnielinski's correlation has a wide range of validity, which is $0.5 < Pr < 2000$, $3000 < Re < 5 \times 10^6$. Both Dittus-Boelter and Gnielinski equations are used for smooth ducts, but in reality there are also cases with rough surfaces. In these, the heat transfer increases mainly due to the impact of air on the rough elements, and the turbulent effects downstream of the rough elements.

The results for the **entry region** are different from the fully developed ones. Its study is more complicated because both the momentum and the energy equation must be taken into account the streamwise variation in velocity and dimensionless temperature. Solutions have been obtained for a situation in which both the hydrodynamic and thermal boundary layer are developing. The results plotted are usually showing the Nusselt number, or the Stanton number $St = \frac{Nu}{Re\ Pr}$, over the reciprocal of the Graetz number $Gz = (D/x)RePr$.
For example, for a combined entry length problem with constant surface temperature $T_s = cost$ the Baehr-Stephan's correlation can be used, as in Equation 2.55

$$\overline{Nu} = \frac{\frac{3.66}{tanh[2.264Gz^{-1/3} + 1.7Gz^{-2/3}]} + 0.0499\ Gz\ tanh(Gz^{-1})}{tanh(2.432Pr^{1/6}Gz^{-1/6})} \tag{2.55}$$

The Nusselt number is intended as the averaged Nu over the desired region within the entry region. The results should behave as in Figure 2.29

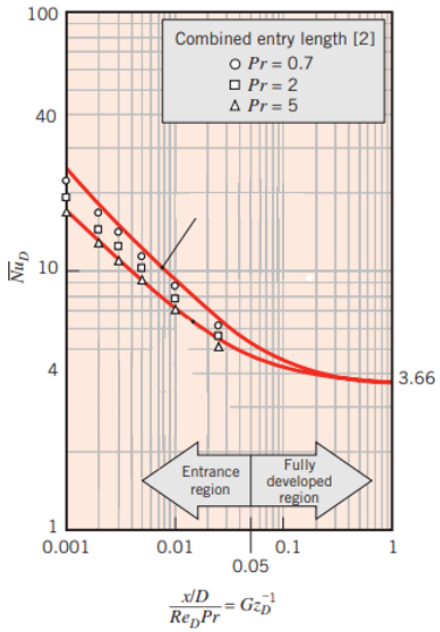

Figure 2.29: Entry region Nusselt over reciprocal of Graetz number for a combined entry region problem

Chapter 3

Experimental Methodology

In the previous sections an extensive theoretical background have been presented, but the experimental methodology has not been explained yet. The objective of the thesis has been outlined, along with the theoretical framework aimed at comprehending the operational principles of the SRHT test rig. Consequently, the following chapter necessitates to blend theory and practice to clarify the procedure to get the results. This will include the generation of the rough surface model, an introduction of the experimental setup and its working principle, as well as a detailed description of the acquired data and their application in determining the HTC of the rough surface. The post-processing of the collected data will be addressed, with distinct solving models for smooth and rough surfaces, which will be deeply explained. Eventually, the results will be presented and discussed.

3.1 Analogue Rough Surface Modeling

Width	90 mm
Length	150 mm

Table 3.1: Dimensions of the upscaled rough surface

The test objects of experiments are rough surfaces, with dimensions shown in Table 3.1, created by upscaling the rough surface of an Aluminum microchannel printed in L-PBF (Table 3.2). The recreation of the surface in an increased size takes the name of analogue (or surrogate) rough surface. In previous works, some Scanning Electron Microscope (SEM) images of the channel inner section have been taken to visually represent the SR and to study the diameter distribution of the

Al cooling channel	
Diameter	1.5 mm
Length	90 mm
Material	Alluminium (Al)
Printing direction	Vertical (90°)

Table 3.2: Technical features of the Aluminium cooling channel

rough elements, which are mainly spherical Aluminum elements created during the AM building process (Figure 3.1).

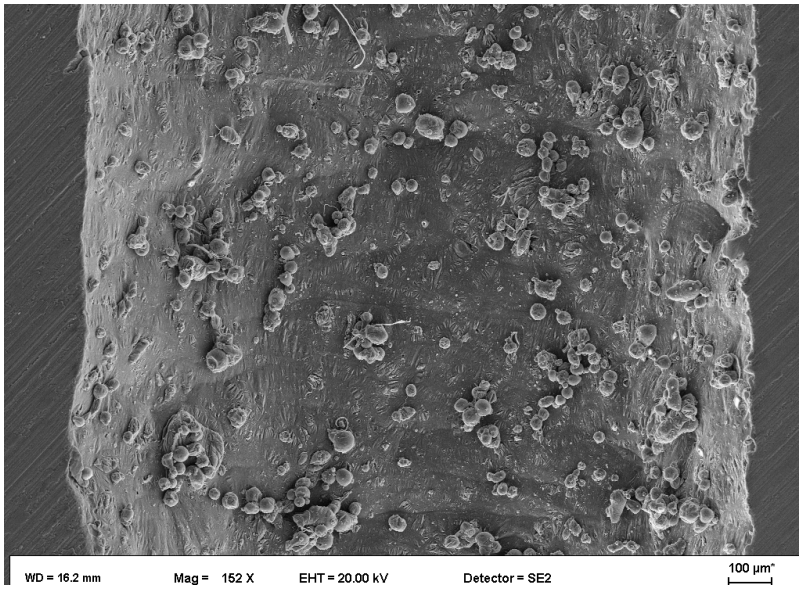

Figure 3.1: SEM image of the internal section of the Aluminium cooling channel

In addition, for the purpose of this thesis, profilometer measurements have been done to get the main roughness parameter presented in Section 2.3.2.1. The process to get an analogue surface model takes inspiration from the work of Clemenson et al. [20] and Hanson [23] with some differences and simplifications:

1. Take profilometer measurement to calculate the average SR parameters and find the upscaling factor for the rough elements;

2. Manually pick up the diameters size from SEM images using a *MATLAB* code, find the most suitable statistical distribution for the upscaled diameters (i.e. Normal, Gamma, etc...), and calculate the density of spheres for square millimetres;

3. Use the diameter statistical distribution and an offset statistical distribution as an input to create a 3D model of the analogue rough surface with a macro [1] in *NX*.

4. Move the spheres that are outside the edges or over the reference points to calculate the output roughness parameters of the analogue SR model.

In the previous thesis work carried out by Wen [27], the analogue rough surface model replicated only three rough parameters out of five that had been selected as the most relevant. For instance, R_a, R_q, and R_z were under 5% error, but R_{sk} and R_{ku} were inaccurate. From the heat transfer results, the average Nu results were comparable with the one from the *QSSHT* rig. Moreover, a CFD thermal analysis highlighted the good fitting of the results. Concerning the development of an analogue rough surface:

- An analogue rough surface with matching R_a, R_q, and R_z will be developed;
- An analogue rough surface with matching R_{sk} and R_{ku} will be created;
- An optimization algorithm based on Genetic Algorithms (GA) to find the perfect vertical positions of the rough elements will be presented in Appendix B;

The idea for the long run is to develop a rough surface that can fully replicate the real one. In the course of this thesis, the choice to develop two models without all the matching parameters stems from two main reasons: firstly, Wen results with matching R_a, R_q, and R_z aligned well with the other test-rig and with CFD results. Secondly, in future the idea is to understand if matching R_{sk} and R_{ku} can lead to good results. However, it is important to know that the experimental research in the course of this dissertation is focused in the analysis of the model with matching R_a, R_q, and R_z. This allow to compare the results with Wen and discuss on local thermal characteristics.

3.1.1 Stylus-Profilometer Measurement

In stylus profilometry a fine-tipped stylus is traced across a straight line on the rough surface of a sample to record its surface profile. The stylus is typically made of diamond, or other hard material, with a sharp tip. A known controlled force is applied

[1] Macro: code to automatically perform actions in a program without giving manual input every time. For example, in *NX* a Python code that generates spherical roughness elements has been used.

on it to ensure consistent contact pressure throughout the measurement. It is moved along the surface of the sample and it moves up and down in response to the surface profile. A transducer, often based on piezoelectric technology, converts vertical movement of the stylus into electrical signal, which contains information of peaks and valleys corresponding to surface features such as ridges, grooves and roughness. The electrical signal is then processed and converted into surface roughness parameters such as R_a, R_q, etc... The measured parameters are typically displayed on a screen, providing a diagram such as in Figure 3.2b. In our case, the Aluminium channel has been cut in half to access the inner surface and one of the two pieces was positioned and blocked to proceed with the measurement.
The measurement were repeated six times in different lines of 4 mm each. The averaged values with the respective errors on the mean are showed in Table 3.3. The values of the error on the average is calculated through the standard deviation of the mean (Equation 3.1), where the i-th value of a rough parameter is x_i, S_x is the standard deviation of the measured rough parameter and N is the number of values ($N = 6$ in this case):

$$S_{\bar{x}} = \sqrt{\frac{\sum_{i=1}^{N}(x_i - \bar{x})^2}{N(N-1)}} = \frac{S_x}{\sqrt{N}} \tag{3.1}$$

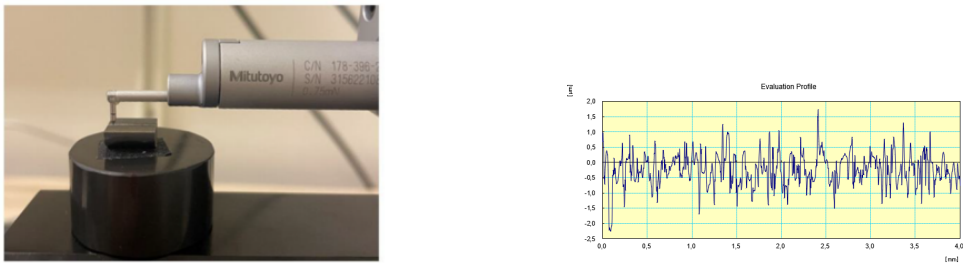

(a) Profilometer Mitutoyo Surftest SJ-410 (b) Example of heigths plot

Figure 3.2: Profilometer measurement of the Aluminium rough surface

R_a $[\mu m]$	R_q $[\mu m]$	R_z $[\mu m]$	R_p $[\mu m]$	R_v $[\mu m]$	R_{sk}	R_{ku}
5.89 ± 0.28	7.44 ± 0.28	36.62 ± 1.05	20.20 ± 0.54	16.42 ± 0.60	0.218 ± 0.08	3.47 ± 0.36

Table 3.3: Roughness parameters of the real-size rough surface

3.1.1.1 Upscaling Factor and Upscaled Roughness Parameters

To create the analogue rough surface it is fundamental to recreate the upscaled surface parameters. Yet, the upscaling factor of our duct needs to be defined in

order to proceed. Given the dimensions of the duct (Table 3.17), considering also the rounded shaped corners with a radius of 5 mm, the upscaling factor is calculated from the ratio of the hydraulic diameters of the upscaled test-rig and the hydraulic diameter of the real channel, which has been calculated with a *MATLAB* code that allows to manually follow the perimeter of the duct. The upscaling factor then results in:

$$\begin{aligned} s &= \frac{D_{h_{upscaled}}}{D_{h_{real-size}}} \\ &= \frac{96.7}{1.53} \\ &= 63.15 \end{aligned} \tag{3.2}$$

By upscaling the measured roughness parameters, except for the skewness and kurtosis of the heights, the roughness parameters that needs to be replicated are shown in Table 3.4.

R_a $[mm]$	R_q $[mm]$	R_z $[mm]$	R_p $[mm]$	R_v $[mm]$	R_{sk}	R_{ku}
0.37 ± 0.04	0.47 ± 0.04	2.32 ± 0.12	1.27 ± 0.06	1.03 ± 0.06	0.218 ± 0.16	3.47 ± 0.72

Table 3.4: Upscaled roughness parameters

3.1.2 SEM Images Analysis

The SEM used in previous works is a Jeol JSM-IT500. More information about the working principle and the specifications can be found in literature [42]. The images from the SEM are collected and the diameters of the spherical rough element are picked up manually using a certain scale distance indicated in the right corner in the bottom. The rough element are not always perfectly spherical, but the assumption of a spherical shape can be used for the objective of this thesis. All the diameters are upscaled using the upscaling factor s and collected in a single vector used to find the correct statistical distribution.

The following steps are followed:

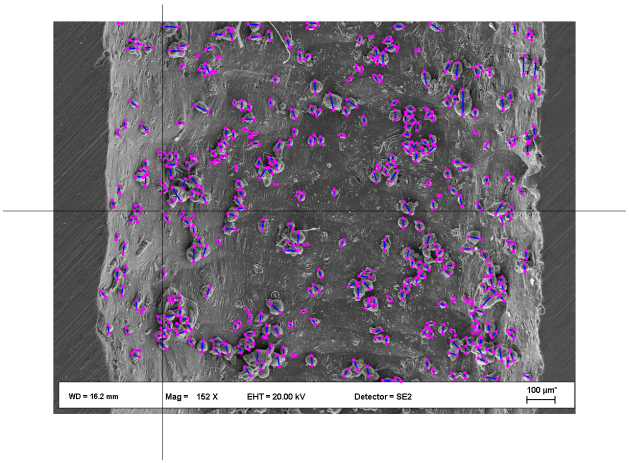

Figure 3.3: Rough element diameters selection

1. An histogram plot to visually represent the number of spheres for a certain interval of diameters is plotted

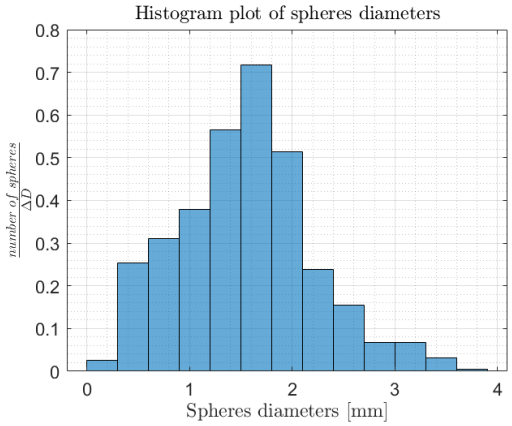

Figure 3.4: Histogram plot for the measured spheres diameters

2. A Kernel Power Density Function (K-PDF) is plotted over the histogram diagram. Using a Kernel Density Estimate (KDE) is beneficial to estimate the probability density function of a dataset, especially when the data may not follow a known parametric distribution [43]. KDE provides a non-parametric way to visualize and analyse the underlying distribution of data, which can be valuable for data exploration, modelling, and hypothesis testing. It helps to uncover patterns and structures in data without making strong assumptions about the distribution, making it a versatile tool in statistics and data analysis. To understand if it is suitable to describe the measured values distribution, a quantile plot is created. Usually a Quantile-Quantile plot (QQ plot) is a graphical tool used in statistics to assess whether a dataset follows a particu-

lar theoretical distribution, typically the normal distribution. It compares the quantiles of the dataset to the expected quantiles of the theoretical distribution. If the points in the QQ plot closely follow a straight line, it suggests that the data is well-modeled by the chosen distribution; deviations from the line indicate departures from that distribution. In our case, the values from the K-PDF are not in line with the measured ones as it can be noticed in Figure 3.5b. Thus, another distribution must be investigated.

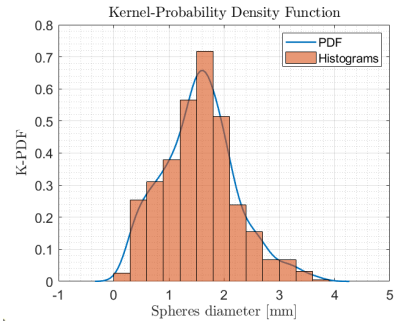

(a) K-PDF of upscaled diameters

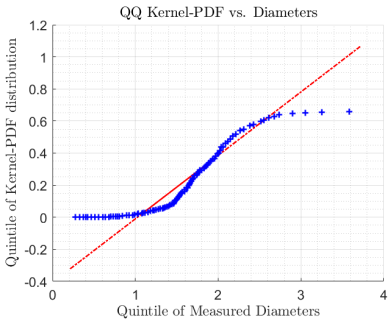

(b) QQ plot K-PDF

Figure 3.5: Statistical properties of k-PDF

3. Due to the distance of the measured values from the values given by the K-PDF, a Gaussian PDF, or Normal PDF, is used to fit the data. Generally, a Normal PDF is the most important probability distribution: if $X \in \Re$ is a standard normal random variable (in our case the diameters), its PDF is given by

$$p(x) = \frac{1}{\sqrt{2\pi\sigma^2}} \exp\left(\frac{-(x-\mu)^2}{2\sigma^2}\right) \tag{3.3}$$

In which σ is the standard deviation calculated as $\sigma = \sqrt{\frac{\sum_{i=1}^{N}(x_i-\mu)^2}{N}}$ and μ is the average of the variable distribution given by $\mu = \frac{\sum_{i=1}^{N} x_i}{N}$. For the manually measured diameters the values of the standard deviation and the average are reported in Table 3.5. The Normal PDF, along with the histogram plot, are presented in this section to give a perspective of the diameters distribution. In this case, the QQ plot 3.6b shows a reliable pattern of the Normal distribution, because the values are in the same straight line of the measured ones, except for few outliers in the far edges of the distribution.

Furthermore, the Cumulative Distribution Function (CDF) 3.6c is plotted. Given a certain diameter, the CDF tells what is the probability that a diameter D_i will take a value between two set limits. If X is the set random diameter

Diameters PDF parameters	
σ	0.66 $[mm]$
μ	1.55 $\pm 0.03[mm]$

Table 3.5: Standard deviation and mean value of diameters distribution for the first model of upscaled rough surface

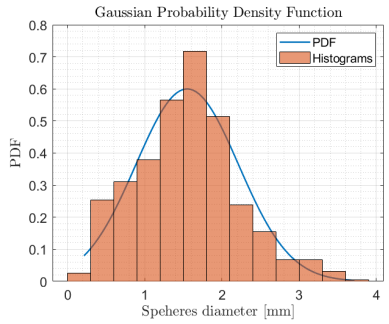

(a) Normal PDF upscaled diameters

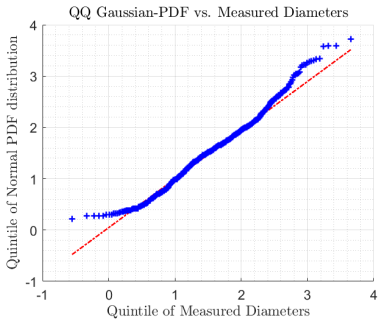

(b) QQ plot Normal PDF

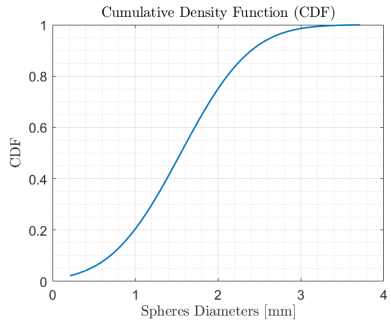

(c) Cumulative Density Function

Figure 3.6: Statistical properties of the Normal PDF fro upscaled diameters

distribution and x is a value of the distribution:

$$P(X_a \leq x \leq X_b) = \int_{X_a}^{X_b} \frac{1}{\sqrt{2\pi\sigma^2}} \exp\left(\frac{-(x-\mu)^2}{2\sigma^2}\right) dx \tag{3.4}$$

The values of a CDF are never negative. From Figure 3.6c we can see, for example, that the probability for a spherical rough element to have a diameter between 1 mm and 2 mm is around 55%, thus more than half of the spheres will be in this interval on our analogue rough surface.

$$\begin{aligned} P(1 \leq D \leq 2) &= 0.75 - 0.25 \\ &= 0.55 \end{aligned} \tag{3.5}$$

Offsets PDF parameters	
σ	0.47
μ	0.5

Table 3.6: Statistical parameters for a Normal offset distribution

3.1.2.1 Rough Elements Density

To create a surrogate rough surface representative of the real-size channel, the density of the spheres should match. This parameters can simply be calculated knowing the surface area of the manually picked up diameters. Taking into account Figure 3.3, the area is given by $A = \frac{\pi}{2} R \cdot L = 3.06\ mm^2$ where R is the radius of the channel and L is the sample image length. The 733 spheres are the total elements manually picked up using the *Matlab* code. Thus, the density of the rough elements ρ_s for the analogue rough surface considering the upscaling factor s is given by

$$\rho_s = \frac{number\ of\ spheres}{A \cdot s^2} = 0.06 \left[\frac{spheres}{mm^2} \right] \tag{3.6}$$

3.1.3 First Analogue Rough Surface Generation

The generation of the rough surface is accomplished using a macro in *Siemens NX*. The working principle of the code is to take as input the spheres density, diameter distribution and offset distribution to create spherical rough element over a selected surface. Despite the diameter distribution and the spheres density has already been calculated, the offset distribution must be discussed before going on with the roughness generation.
Firstly, the offset is defined as the ratio of the vertical position of the sphere center z over the radius of the sphere.

$$off = \frac{z}{D/2} \tag{3.7}$$

To replicate the heights pattern of a random rough surface the spheres must be put at different offsets. On this purpose, the offset input is set to be a Normal PDF as Equation 3.3 with variables given in Table 3.6.
With the input presented so far, the coarse analogue rough surface presents some spheres hanging out of the edges and some spheres are over the reference points needed for the post processing of the IR videos. This is sorted out manually moving

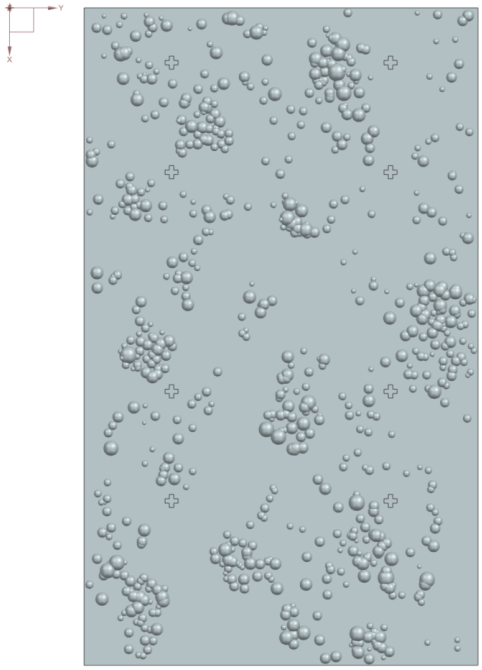

Figure 3.7: Analogue rough surface generated from the spheres density, upscaled diameters distribution and offset distribution.

the spheres inside the edges and far from the reference points. The definitive rough surface is presented in Figure 3.7.

3.1.4 Analogue Rough Surface Parameters

To understand whether the analogue rough surface is representative of the real size channel, the roughness parameters must be checked. To calculate them, a *Python* code is used, which working principle is to generate a mesh grid of the surface and calculate the roughness heights. The output analogue SR parameters are shown in Table 3.7 with the percent relative errors calculated as $E\% = \frac{|(R_i)_{analogue} - (R_i)_{real}|}{(R_i)_{real}} \cdot 100$

	R_a $[mm]$	R_q $[mm]$	R_z $[mm]$	R_{sk}	R_{ku}
Real SR parameters (upscaled)	0.37	0.47	2.32	0.22	3.47
Analogue SR parameters	0.37	0.49	2.35	2.00	5.80
Percent Error	0%	4.25 %	0.8%	814%	67.27%

Table 3.7: Upscaled roughness parameters

As we can see from the results in Table 3.7 the relative error for R_a, R_q, R_z are small. The skewness R_{sk} and kurtosis R_{ku} have an high error, which is due to how the roughness is modelled, since the real AM surface has some more complex structures rather then spheres randomly located over a flat plate. However, both the skewness values are positive and both the kurtosis values are more than three, which means we have wide valleys (which in the analogue surface are the smooth spots) and little peaks.
Furthermore, one of the most important aspect of the analogue rough surface is the presence of clusters, i.e. rough elements grouped together leaving wide smooth spots. This can be a fundamental aspect in the HT investigation, thus it needs to be replicated.

3.1.5 Second Analogue Rough Surface Generation

Following the same process described in the previous section, another rough surface is generated. In this model, the R_{sk} and R_{ku} have to be matched. In a trivial way, the diameters distribution and offset distributions are adjusted to match the skewness and kurtosis of the analogue rough surface. For sake of clarity, in the future work this process aims to study what are the main parameters affecting the enhancement of heat transfer related to AM. For instance, the first analogue surface matches the mean, standard deviation and maximum distance from peak to valley, but it doesn't match the skewness and kurtosis. The second surface matches better the kurtosis and skewness instead. The experimental investigation, key of future research, will clarify the most relevant parameters in convective HT enhancement. In the following tables the input parameters of diameters distribution and offset distributions (which are remarkably different from the real ones) along with the resulting rough parameters and the error with respect to the real rough surface measurement are presented.

Diameters distribution

Type of distribution	Gamma		
Equation	$f(x;k,\theta) = \frac{x^{k-1}e^{-x/\theta}}{\theta^k \Gamma(k)}$		
Parameters	$k = 0.509$	$\theta = 2.40$	$\Gamma(k) = \int_0^\infty t^{k-1}e^{-t}\,dt$

Table 3.8: Diameters distribution in input for the roughness generation. $x \in \Re$ represents the diameters while k is the shape factor and θ is the scaling parameter for the Gamma distribution

Offsets distribution

Type of distribution	Normal	
Parameters	$\mu = 0.10$	$\sigma = 0.20$

Table 3.9: Offsets distribution for the second analogue rough surface.μ is the offsets average, while σ is the standard deviation of the distribution.

	$R_a\ [mm]$	$R_q\ [mm]$	$R_z\ [mm]$	R_{sk}	R_{ku}
Real SR parameters (upscaled)	0.37	0.47	2.32	0.218	3.47
Analogue SR parameters	0.62	0.69	2.48	0.29	3.50
Percent Error	66.7%	46.81 %	7.27%	1.36%	0.94%

Table 3.10: Upscaled roughness parameters

3.1.6 Limitations

In the analogue rough surface generation there are several limitations that have to be taken into account, such as:

- The stylus-profilometer data are acquired along a straight line so they are not representative of the 3D parameters, even if six measurement in different positions were taken;
- The SR elements are chosen to be spheres, but there are many other different shapes that could be tried, such as ellipsoids;
- The roughness parameters for a datum material depends on the printing pa-

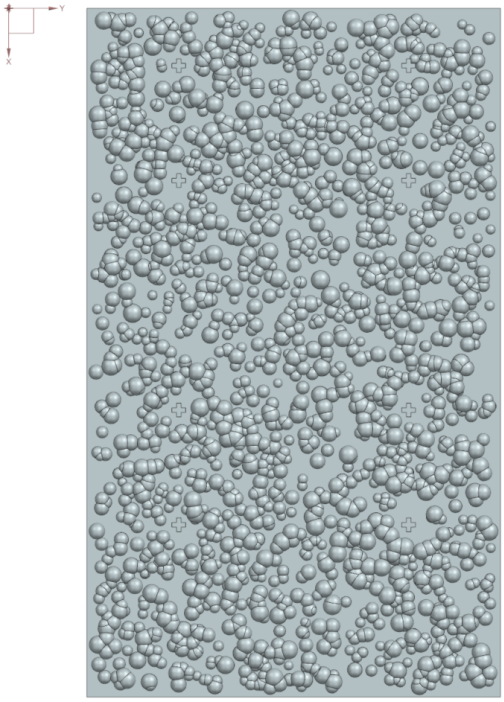

Figure 3.8: Second analogue rough surface

rameters (i.e. direction, velocity, etc ...), thus the study can be limited to only one case of study.

3.1.7 3D printing and painting of the analogue rough surfaces

The analogue models of SR are printed from an external company. The 3D model is sent in a *.stp* format and then printed using Stereolitghography (SLA) . The material used is *Accura Xtreme Grey* whose main technical features can be found in Table 3.11. It is important to highlight the difference between radial and axial properties: axial properties are referred to the behaviour through the layers, while the behavior along the layers is given by the radial properties. Since there are variations in the values of thermal conductivity k and heat capacity C_p for radial and axial direction, both of the values are presented.
Since the experiments are done with hot air and an IR camera is used to measure the wall temperature, the material must fulfill some requirements:

- Resist to high temperatures without melting;
- Do not present high temperature gradients.

$T\ [°C]$	$k_{ax}\ [W/mK]$	$k_{rad}\ [W/mK]$	$C_p\ [J/kgK]$
23	0.224	0.211	1442.4
50	0.227	0.237	1735.9

Table 3.11: Accura Xtreme Grey properties in axial and radial direction

Furthermore, one of the most important aspect is the emissivity of the test object. For instance, while performing IR thermography one has to take into account that the test object should behave as much as possible as a perfect BB . This allows to have high accuracy of the measured temperature. Thus, a black paint resistant to high temperatures (provided by *Senotherm*) is used to cover the test objects and the inner surface of the duct with a thin layer. The thermal properties of the paint, which will be used to calculate the wall temperature in the following sections, has been calculated during a process of calibration by Lehamann [26], which will be clarified in Section 3.2, and can be found in Table 3.12. It has to be remarked that an ideal BB has a coefficient of absorptivity α ideally equal to one, so that the transmittivity τ and reflectivity ϱ are zero, because it is always valid that the sum of the coefficients is equal to one

$$\alpha + \varrho + \tau = 1 \tag{3.8}$$

In reality, as previously presented in Section 2.5, ideal BB doesn't exist, thus the real coefficients for the *Senotherm* paint have to be determined through calibration. Furthermore, the Kirchhoff first Law is valid, so that the thermal emissivity ε is equal to the coefficient of absorptivity.

$$\alpha = \varepsilon \tag{3.9}$$

	ε_{paint}	τ_{paint}	ϱ_{paint}
Senotherm paint	0.9072 ± 0.0274	0	0.0540 ± 0.0062

Table 3.12: Paint coefficients

3.2 Calibration Process

For the test-rig in use three different calibrations are needed:

Parameter	A	B	C	D	T_0
Value [**K**]	-0.1893	1.5596e-5	-5.612e-8	37.15	-0.4323
Uncertainty [**K**]	± 0.0721	$\pm 9.850e-6$	$\pm 5.855e-8$	± 0.3736	± 0.4671

Table 3.13: Calibration coefficient

1. Camera calibration to determine the calibration function which relates the radiometric signal measured by the camera and the value of temperature corresponding to that signal (more details about the camera can be found in Section 3.5.2);

2. Paint calibration to determine the values of the optical coefficients τ_{paint}, ϱ_{paint}, ε_{paint};

3. Infrared Window (IRW) calibration to find the optical coefficients τ_{IRW}, ϱ_{IRW}, ε_{IRW};

Generally, a process of calibration is used to create a correlation between two physical quantities which are unrelated a priori. For instance, when performing IR thermography a detected radiometric signal measured by a sensitive sensor can be translated into a value of temperature through a process of calibration, which culminates with the definition of a calibration equation referred as $F_{S\to T}$. It is remarkably important to underline that the detected signal is a general radiometric signal received by the camera, but it is not only given by the signal emitted by the test objects.
Curve-fitting is a common practice to find continuous functions between the measured radiometric signal and the corresponding values of temperatures. During this work, the correlation in Equation 3.10 proposed by Liebmann [44] was used. From now on $F_{S\to T}$ will be referred to the equation that allows to go from the values of the signal to the one of the temperature and $F_{T\to S}$ the opposite.

$$T = AS^{\frac{1}{2}} + BS^{\frac{3}{2}} + CS^2 + Dln(S) + T_0 \tag{3.10}$$

In [26] all the process of calibration has been undergone, since it was the first time an IR camera was used for this test rig. In this work all the process of calibration is not meant to be carried out again, but the results are used in order to make the investigation repeatable. The calibration coefficients for the camera can be found in Table 3.13 with the respective uncertainty.
Equation 3.10 will be used in *Matlab* to process the IR camera data once the radiometric signal from the test object S_B is known. In the next paragraph the reason

why the pure radiometric signal detected by the camera cannot be used to determine the wall temperature will be better clarified.
For instance, the test objects, considered as a BB, are not the only source of radiometric signal. Also the ambient plays a fundamental role, as important as the emissions of the internal walls of the channel. The signal detected from the camera sensor, considering the ambient, the walls and the test objects as ideal BB, is

$$S_{det} = \varepsilon_{paint}\tau_{IRW}S_B + \varrho_{IRW}S_{amb} + \varrho_{paint}\tau_{IRW}^2 S_{amb} + \varepsilon_{paint}\varrho_{paint}\tau_{IRW}S_c \qquad (3.11)$$

The different terms of Equation 3.11 respectively refer to the signal emitted from the test object covered with paint S_B and transmitted through the Infrared Window (IRW) , the ambient signal S_{amb} (considering the ambient with $\tau_{amb} = 1$ since the distance is small [45]) reflected on the IRW, the ambient signal transmitted through the IRW then reflected over the test objects covered of paint and again transmitted through the IRW, and the inner channel signals emitted by all the surfaces S_c (except the test objects) reflected by the test objects and transmitted through the IRW. The unknown parameter that has to be calculated from Equation 3.12 is the radiometric signal of the test object S_B.

$$S_B = \frac{S_{det} - (\varrho_{IRW} + \varrho_{paint}\tau_{IRW}^2)S_{amb} - \varrho_{paint}\varepsilon_{paint}\tau_{IRW}S_c}{\varrho_{paint}\tau_{IRW}} \qquad (3.12)$$

The optical parameters of the IRW as well as the optical parameters of the paint where a priori unknown, but Lhemann [26] was able to determine them with a process of calibration. Their values can be found in Table 3.14

Object	*Emissivity*	*Transmissivity*	*Reflectivity*
Senotherm paint	0.9072 ± 0.0274	0	0.0540 ± 0.0062
IRW	0	0.9489 ± 0.0334	0.0501 ± 0.0068

Table 3.14: Paint and IRW coefficients

To calculate the signal emitted by the ambient and by the internal walls, the temperatures T_{amb} and T_c must be known. The first term is easy to know from a thermometer in the test chamber, while the wall temperature is hard to be measured, thus it is approximately chosen as the temperature over smooth plates test objects, since also the internal walls are smooth. The inverse function $F_{T\to S}$ is then used to determine S_c and S_{amb}.

Eventually, the only unknown is the signal from the test objects S_B which can be calculated using Equation 3.12 and leads to the wall temperature through $F_{S\to T}$, i.e. Equation 3.10

3.3 Introduction to Experimental Study

In Section 2.6 the hydrodynamic and thermal characteristics for channel flows have been presented. The QSSHT test-rig, presented in Riccardo Pagani's work, show that the behavior of friction factor and Nusselt number change with the material of the specimen, i.e. with the SR parameters.
While the main scope of the thesis is the local study of the HT over additively manufactured rough surfaces, another objective is to understand what are the most influencing roughness parameters in HT enhancement. Similarity of wall surfaces requires to properly upscale the surface roughness in order to get similar relative roughness. Furthermore, flow similarity requires to run the tests at same Reynolds. On this purpose, the fundamental dimensionless parameter to describe the local HT is the Nusselt number. As previously explained, it is the ratio of convective to conductive heat transfer and in nature there are only few cases in which it can be analytically calculated.

$$Nu = \frac{hD_h}{k_{air}} \tag{3.13}$$

In our case, the Nusselt number can only be indirectly measured by investigating the heat conduction at the wall. Even if the solver used for smooth and rough surfaces is different, the basic principle is related to finding the convective HTC by measuring the distribution of T_w over the plates in a transient experiment. Generally, when a massflow with temperature T_∞ streams over a surface of temperature T_w a thermal boundary layer develops. As the Newton's law states, the convective heat flux $\dot{q_w}$ is given by the product between the convective HTC and the difference between the wall temperature and the flow temperature. Due to the fact that at the surface there is only conduction, the same quantity of convective heat flux can be expressed in therms of conductive heat transfer using Fourier's law.

$$\dot{q_w} = h(T_w - T_\infty) = -k_{material}\nabla T\big|_w \tag{3.14}$$

Inverting the Newton's law of cooling, the HTC is given by the ratio of the surface heat flux $\dot{q}$ and the difference between the surface temperature T_w and the flow

temperature T_∞.

$$h = \frac{\dot{q_w}}{T_w - T_\infty} \tag{3.15}$$

Given the thermal conductivity of the fluid k_{air} (which is a property that can be found in tables), as previously said, the Nusselt number can be calculated solving a transient conductive problem over a surface to find the convective HTC.

$$\begin{aligned} Nu &= \frac{hD_h}{k_{air}} \\ &= \frac{-\nabla T\big|_w}{(T_w - T_\infty)/D_h} \end{aligned} \tag{3.16}$$

The SRHT uses this basic concept to calculate the local HTC of smooth and rough surfaces positioned on the bottom of a rectangular duct, but the proper solver needs to be studied in depth to understand the underlying assumptions and relations that constitute the SRHT test rig.

3.4 Underlying Equations

To properly understand how to proceed with the post-processing of acquired data, it is important to understand the equations that allow to obtain the results in term of local HTC and Nusselt number over the surface. As explained in Section 3.6, despite the acquired data for rough and smooth plates are the same, the results are obtained in different ways. In this section the main solver will be presented in order to have the basics to understand the post-processing of data.

3.4.1 1D Heat Transfer for Smooth Plates

The local HTC of the smooth plates located on the bottom of the channel is one of the numerous case of study of transient conduction, where the thermal partial differential equation in rectangular coordinates yields [39].

$$\frac{\partial^2 T}{\partial^2 x} + \frac{\partial^2 T}{\partial^2 y} + \frac{\partial^2 T}{\partial^2 z} + \frac{q}{k} = \frac{1}{\alpha}\frac{\partial T}{\partial t} \tag{3.17}$$

In 1D heat transfer problems, with no internal generation and the assumption of constant thermal conductivity, the Equation 3.17 reduces to Equation 3.18. Furthermore, this is the case of a semi-infinit solid: a simple geometry for which an analytical solutions may be obtained. In principle, the solid extends to infinity in all but one direction, thus it can be characterized by a single identifiable surface. If a sudden change in temperature is imposed at this surface, transient, one-dimensional

conduction will occur within the solid. This is used, for example, to determine transient heat transfer near the surface of the earth or to approximate the transient response of a finite solid, such as a slab. This last case is similar to our problem of smooth plates, but only for the early portion of the transient, during which temperatures in the plates interior are essentially uninfluenced by the change in surface conditions. The heat equation for transient conduction in a semi-infinite body is the following

$$\frac{\partial^2 T}{\partial^2 z} = \frac{1}{\alpha}\frac{\partial T}{\partial t} \tag{3.18}$$

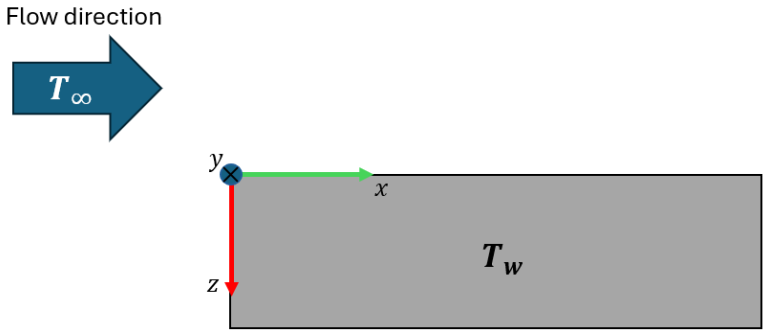

Figure 3.9: Schematic view of the model used for 1D solution. x coordinate is parallel to the streamwise direction nd the z axis is pointing inside the plate

Taking into consideration the model in Figure 3.9, where z is the perpendicular coordinate to the streamwise direction x of the air and T_∞ is the mainflow air temperature over the flat plate (Figure 3.9), to understand how the local temperature of the wall varies with respect of time and spatial coordinate we need to specify one initial condition and two Cauchy boundary conditions. For a typical transient conduction problem, the initial condition presumes a uniform initial temperature T_i along coordinate z at time $t = 0$

$$T(z, t = 0) = T_i \tag{3.19}$$

the first interior boundary condition is

$$T(z \to \infty, t) = T_i \tag{3.20}$$

and the second boundary conditions combines Newton's law of convection and the Fourier's law of conduction, which is related to the problem of surface exposed to a temperature of the fluid $T_\infty \neq T_i$ (a step change in temperature):

$$-k\frac{\partial T}{\partial z}\Big|_{z=0} = h[T(0, t) - T_\infty] \tag{3.21}$$

An analytical solution for this case of study can be found yielding to Equation 3.22

$$\frac{T(z,t)-T_i}{T_\infty - T_i} = erfc\left(\frac{z}{2\sqrt{\alpha t}}\right) - \left[exp\left(\frac{hz}{k}+\frac{h^2\alpha t}{k^2}\right)\right]\left[erfc\left(\frac{z}{2\sqrt{\alpha t}}+\frac{h\sqrt{\alpha t}}{k}\right)\right] \quad (3.22)$$

where the physical quantities $\alpha = k/\rho c_p$ is the thermal diffusivity of the material, h is the HTC unknown variable of the investigation, k is the thermal conductivity of the material, and $T(z,t)$ is the wall temperature T_w measured through the IR camera. So, the surface temperature varies for each position in the streamwise direction and this equation will be solved iteratively, through a non linear solver, for each pixel in order to get the HTC. The resolution of the surface temperature relies on the resolution of the IR camera. The complementary error function $erfc(W) = 1 - erf(w)$. In the case of surface convection, with a step change of temperature the surface temperature and the temperature within the medium approach the fluid temperature T_∞ with increasing time. Thus, the maximum elapsed time t_{max} depends on the material properties (Xtreme Accura Grey), i.e. thermal diffusivity in the worst case scenario $\alpha = 1.43 \cdot 10^{-7}$ $[m^2/s]$ as well as the thickness $\delta = 1.5$ cm of the plates, and it can be demonstrated that it must be

$$t_{max} < \frac{\delta^2}{16\alpha} \approxeq 120 \ s \quad (3.23)$$

3.4.2 3D Heat Transfer for Rough Plates

While investigating the analogue rough plates, a 1D HT solver is no longer able to capture the real HT phenomena. For instance, the spherical rough elements are 3D structures. Therefore, 3D effects must be taken into account to obtain reasonable results. An helpful tool, in these cases, is Finite Element Method (FEM) analysis. Generally, the procedure consists in mapping the surface temperature measured by the IR camera onto the mesh model of the rough plate. Then the HTC of the rough surface is calculated inversely by solving a direct problem and an ad-joint problem to obtain the difference between the measured and calculated temperature in order to minimize the difference between them. This is done by an internal company software called *C3D*.

3.4.2.1 Mesh and Mapping Method of the CAD Model

A tetrahedral mesh model is created over the rough plate model described in Section 3.1 using *Siemens NX*. In Table 3.15 the mesh information are listed.

The mapping process of the IR camera data onto the 3D mesh model, requires some knowledge on how the camera projects a real world object onto a 2D image.

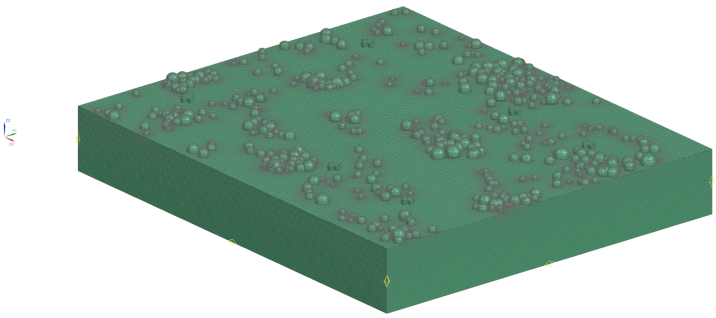

Figure 3.10: Mesh example for the first analogue rough surface

The camera model is generally expressed by Equation 3.24

$$\begin{bmatrix} u \\ v \\ 1 \end{bmatrix} = \begin{bmatrix} p_{11} & p_{12} & p_{13} \\ p_{21} & p_{22} & p_{23} \\ p_{31} & p_{32} & p_{33} \end{bmatrix} \begin{bmatrix} X \\ Y \\ Z \\ 1 \end{bmatrix} \tag{3.24}$$

Where (u, v) are the image coordinates of the camera and (X, Y, Z) are the world coordinates. The generic projection matrix P can be expressed as $P = K[R\ t]$, where K is the calibration matrix containing the distortion information of the camera, R is the rotation matrix describing how the world frame is rotated relative to the camera frame, and the vector t describes the translation between the world frame and the camera frame. There are twelve unknowns in the P matrix. To estimate P, the image coordinates must be known variables as long as the real world coordinates of at least six points (they must not be on the same plane), which must be manually selected from the CAD model. The solution process is summarized below [46].
Firstly, the matrix P is rewritten as a vector p, where

$$p = \begin{bmatrix} p_{11} & p_{12} & p_{13} & p_{21} & p_{22} & p_{23} & p_{31} & p_{32} & p_{33} \end{bmatrix}^T \tag{3.25}$$

For a given point with coordinates (u_1, v_1) and (X_1, Y_1, Z_1), the yielding relation is:

$$\begin{bmatrix} X_1 & Y_1 & Z_1 & 1 & 0 & 0 & 0 & 0 & -u_1X_1 & -u_1Y_1 & -u_1Z_1 & -u_1 \\ 0 & 0 & 0 & 0 & X_1 & Y_1 & Z_1 & 1 & -v_1X_1 & -v_1Y_1 & -v_1Z_1 & -v_1 \end{bmatrix} p = \begin{bmatrix} 0 \\ 0 \end{bmatrix} \tag{3.26}$$

Mesh Parameters	
Element Type	$DC3D10$
Element Size	1.5 mm
Surface Maximum Growth Rate	1.5
Surface Meshing Method	*Mesh from Facets*
Surface Mesh Settings	
Minimum Element Size (% of Target Element Size)	2.6
Minimum Element Size (Read-Only)	0.039
Level of Discretization Based on Curvature	25
Volume Mesh Settings	
Internal Mesh Gradation	1
Minimum Two Elements Through Thickness	True
Model Cleanup Options	
Small Feature Tolerance (% of Element Size)	15.5
Minimum Element Length (Read-Only)	0.2325

Table 3.15: 3D tetrahedral mesh information

So each point contributes with two equations to the linear system. Even tough six reference points are enough for solving the problem, to improve the accuracy of the solution, two extra points are added to the system. They are chosen from some points that can be easily detected in the IR image. In Figure 3.11 the results for one of the calibrations are shown. The green dots are in the region of interest (ROI), which is the part of the plate that the camera can see from the window. The blue dots are the original points taken from the image, and the black dots are the calculated image coordinates from the resulting camera matrix.

Afterwards, an interpolated wall temperature value from the IR image is fixed on the mesh points within the ROI. Since the mesh points of the rough plate where we desire to do the calibration are selected manually, sometimes there are miscalculations of the wall temperature, leading to errors in the HTC results. The mapping error will be deeply discussed further in Section (), but for now it must be reminded

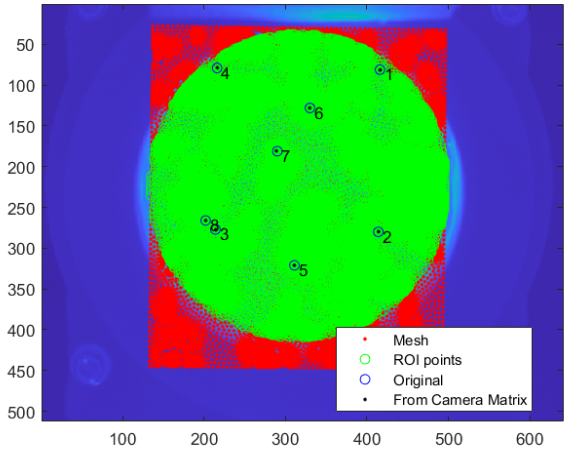

Figure 3.11: Mapping points inside the ROI

that to avoid these errors we have to carefully select the points where we want to do the calibration. Some general rules can be:

- Avoid the connective points between flat parts and spheres;
- Avoid the point that are not seen by the camera;

Furthermore, the mesh refinement, i.e. the mapped points, should be denser in the areas where the temperature gradients are high, otherwise the temperature measured from the IR camera will be mapped in wrong positions over the mesh. For instance, the spheres directly after a smooth part are more affected by high temperature gradients, thus if the mesh is not well refined the risk is to map the smooth temperature over the spheres which is completely incorrect, because generally a sphere has an higher surface temperature, since the upstream part is hit by the hot air flow.
Eventually, all the selected points will be used as reference in solving the inverse problem using six different time steps: $t = 0,\ 10,\ 20,\ 40,\ 70,\ 100$

3.4.2.2 The Calibration Solver

Once the wall temperature data collected from the IR camera are mapped onto the selected nodes of the mesh, the HTC of each element of the mesh can then be adjusted to ensure that the temperature profiles of the nodes align with the mapped values from the IR camera. This problem is identified as an inverse problem, since the HTC is determined in reverse order from the wall temperature data. The objective of this problem is to optimize and identify the most accurate HTC for each

element, trying to minimize any discrepancies between measured and calculated wall temperature values. This process primarily requires solving a direct HT problem, along with its associated adjoint problem [47]. Equations 3.27 can be identified as the direct problem.

$$\begin{cases} \rho c \frac{\partial T}{\partial t} = \nabla \cdot (k \nabla T) \quad in\ \Omega \quad 0 \leq t \leq t_f \\ k \frac{\partial T}{\partial n} = h(T - T_g) \quad on\ \Gamma \quad 0 \leq t \leq t_f \\ T(x, t = 0) = T_0(x) \quad in\ \Omega \end{cases} \tag{3.27}$$

The transient heat transfer problem is defined by convective boundary conditions and an initial condition, as given in Equations 3.27. In these equations, the terms $k(x,T)$, $\rho(x,T)$, $c(x,T)$, $h(x,t)$, $T_g(x,t)$, n, Γ, and Ω represent heat conductivity of the material, material's density, air heat capacity, heat transfer coefficient, bulk gas temperature (usually indicated as T_∞ in the smooth surfaces solver), the outward normal vector on the boundary surface, the body's surface, and the object's body, respectively. The objective is to find the optimal $h(x,t)$ on a subset of Γ that minimizes the target function J.

$$J = \frac{1}{2} \int_0^{t_f} \int_\Gamma (T(x,t) - T_m(x,t))^2 \, d\Gamma dt \tag{3.28}$$

In Equation 3.28, $T_m(x,t)$ stands for the measured wall temperature. Based on the dimensional analysis of the convective heat transfer problem, $h(x)$ is assumed to be time-independent, as the Re and Pr remain constant during the test. Thus, also the Nu will be time independent:

$$Nu \neq f(t) \tag{3.29}$$

In optimization problems, Lagrangian function is often used in the solving process, thus the challenge becomes locating the stationary points of this function

$$\mathfrak{L}(h, \lambda) = J + \int_0^{t_f} \int_\Omega \lambda(x,t) \Big(\rho c \frac{\partial T}{\partial t} - \nabla \cdot (k \nabla T) \Big) \, d\Omega dt \tag{3.30}$$

where λ is the Lagrangian multiplier. $\mathfrak{L}$ is dependent on h and λ even though h is not expressed in the equation, since a small change δh will directly cause a δT. To find the stationary points of $\mathfrak{L}$, the partial derivatives of $\mathfrak{L}$, $\partial\mathfrak{L}/\partial h$ and $\partial\mathfrak{L}/\partial\lambda$ must be equal to zero. As in normal numerical problem the partial derivative $\partial\mathfrak{L}/\partial h$ is approximated by the forward difference $\partial\mathfrak{L}/\partial h = (\mathfrak{L}(h+\delta h) - \mathfrak{L}(h))/\delta h$. After some

transformations [47], $\delta\mathfrak{L}_h$ can be written as

$$\begin{aligned}\delta\mathfrak{L}_h = &\int_0^{t_f}\int_\Omega \delta T\Big(-\rho c\frac{\partial\lambda}{\partial t}\Big)\,d\Omega dt \\ &+\int_0^{t_f}\int_\Gamma \delta T(T-T_m+k\frac{\partial\lambda}{\partial n}-h\lambda)\,d\Gamma dt+\int_\Omega \lambda\rho c\delta T(t=t_f)\,d\Omega \\ &+\int_0^{t_f}\int_\Gamma -\lambda\delta h(T-T_g)\,d\Gamma dt\end{aligned} \tag{3.31}$$

To make sure $\delta\mathfrak{L}_h = 0$ with an infinitely small δh, λ is chosen to satisfy the following equations, since δT is rather unpredictable.

$$\begin{cases} -\rho c\frac{\partial\lambda}{\partial t} = \nabla\cdot(k\nabla\lambda) & in\ \Omega \quad 0\le t\le t_f \\ k\frac{\partial\lambda}{\partial n} = h\lambda-(T-T_m) & on\ \Gamma \quad 0\le t\le t_f \\ \lambda(x,t_f)=0 & in\ \Omega \end{cases} \tag{3.32}$$

So now $\delta\mathfrak{L}_h$ can be written as

$$\delta\mathfrak{L}_h = \int_0^{t_f}\int_\Gamma -\lambda\delta h(T-T_g)\,d\Gamma dt \tag{3.33}$$

And after a variable transformation $\tau = t_f - t$, 3.32 can be written as

$$\begin{cases} \rho c\frac{\partial\lambda}{\partial\tau} = \nabla\cdot(k\nabla\lambda) & in\ \Omega \quad 0\le \tau\le t_f \\ k\frac{\partial\lambda}{\partial n} = h\lambda-(T-T_m) & on\ \Gamma \quad 0\le \tau\le t_f \\ \lambda(x,0)=0 & in\ \Omega \end{cases} \tag{3.34}$$

The system of Equations 3.34 is referred as the adjoint problem. It is really similar to 3.27, which is the direct problem. While solving $\delta\mathfrak{L}_h$ leads to the adjoint problem, solving $\delta\mathfrak{L}_h$ will lead back to the direct problem. To know how δh will cause the change in the target function J, we need to find the sensitivity of J which is defined as the derivative of J with respect to h at a certain point x and time t denoted as J'_h. From equation 3.30 and the fact that T always satisfies the direct problem, it implies that $J'_h \equiv \mathfrak{L}'_h$. And from equation 3.33, $\mathfrak{L}'_h$ can be written as

$$\mathfrak{L}'_h = -\lambda(T-T_g) \tag{3.35}$$

So the solution process can be summarized as follows:

1. Give an initial guess of h and solve the direct problem to obtain the temperature data $T(x,t)$;

2. With the obtained T and the measured T_m as reference values, solve the adjoint problem to obtain $\lambda(x,t)$;

3. Calculate the sensitivity $J'_h(x,t)$ from λ and T, and use it in a gradient-based optimization method to update h and obtain a sufficient reduction of J;

4. Repeat the process with the updated h.

The problem has to be iterated several times to reduce the error. This algorithm has been implemented in *Siemens Energy AB*'s software *C3D* by Jaksch [47].

3.5 Experimental Set-up

The apparatus shown in Figure 3.12 has been used in making the tests. The same apparatus was employed by my predecessor in the investigation of HT enhancement for an analogue rough surface of an *Inconel 939* specimen. A brief description of all the components and the basic working principle will be presented in the following section.

3.5.1 Working Principle

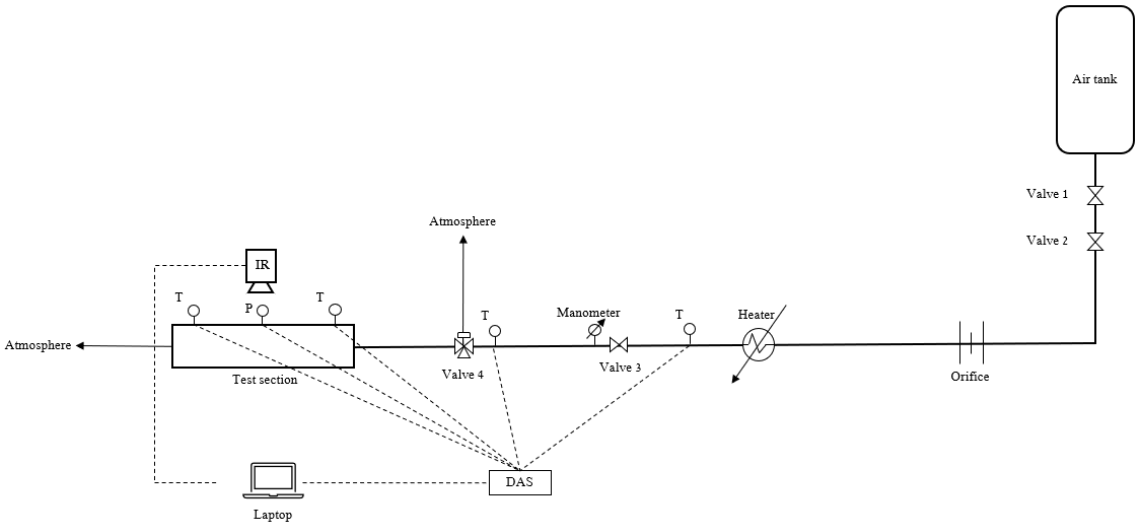

Figure 3.12: Process flow diagram for the SRHT test rig.

After setting up the IR camera using the software *FLIR Research*, the main valves 1 and 2, connected to an 8 bar air supply system, are opened. The first valve is linked to a pneumatic actuator to open the hatch, while the second valve is directly sending air to the test section. Once they're opened, the mass flow passes through an orifice meter where the pressure difference is used to calculate the mass flow, which can be adjusted with a regulator positioned upstream of the flow straightener. The main flow is heated up by an heater and the pressure is reduced to 1.5 bar through a pressure valve regulator (valve 3). Temperature and mass flow are adjusted to obtain the desired Reynolds number.

$$Re = \frac{\dot{m} D_h}{\mu_{air} A} \tag{3.36}$$

Where $\dot{m} = \rho u_\infty A \left[\frac{kg}{s}\right]$ is the measured mass flow, A is the cross section of the duct, ρ is the air density, μ is the dynamic viscosity calculated using Sutherland's

law, P is the inner duct perimeter, and D_h is the hydraulic diameter given by $D_h = \frac{4A}{P}$.

$$\frac{\mu_{air}}{\mu_0} = \left(\frac{T}{T_0}\right)\frac{3}{2}\frac{T_0 + S_\mu}{T + S_\mu} \tag{3.37}$$

The temperature at the outlet of the heater is measured by a thermocouple and the value is only used for safety reasons to check if there is any anomalies in the heating process. The mainflow continues its path toward a three-way valve (valve 4), made of a pneumatic actuator, an hatch and a bypass, installed upstream of the test section. When the main flow reaches the desired temperature value, measured with a Pt100 thermocouple upstream of the three-way valve, a switch is used to open the hatch and the mass flow enters the test section. In non-nominal conditions, i.e. the temperature isn't at the desired value, the hatch is closed and the bypass directs the mass flow out of the test section and into the atmosphere (see Figure 3.13 3.14). However, as soon as the hatch is opened, the hot air passes over the rough surfaces positioned in the bottom plate of the test section and the IR camera positioned in one of the windows starts to record the time variation of the wall temperature T_w and for a period of 110 s. Two thermocouples located at the inlet and outlet of the test section in the centre of the cross section are used to measure the bulk temperature in order to calculate the mass flow temperature T_∞ by linear interpolation.

In the following sections the acquired data and the way they will be used to obtain the results will be presented.

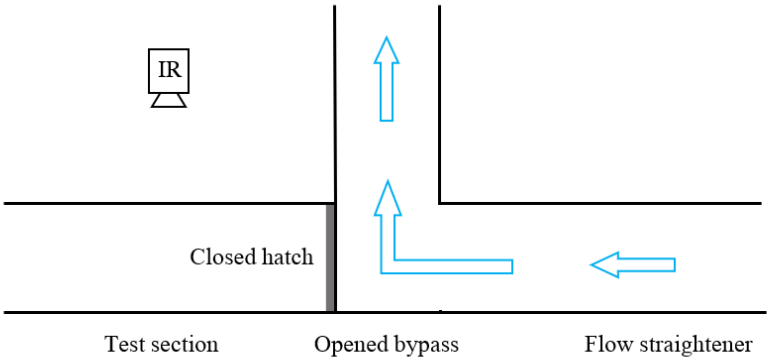

Figure 3.13: Schematic configuration of the flow behaviour when the bypass is opened and the hatch is closed

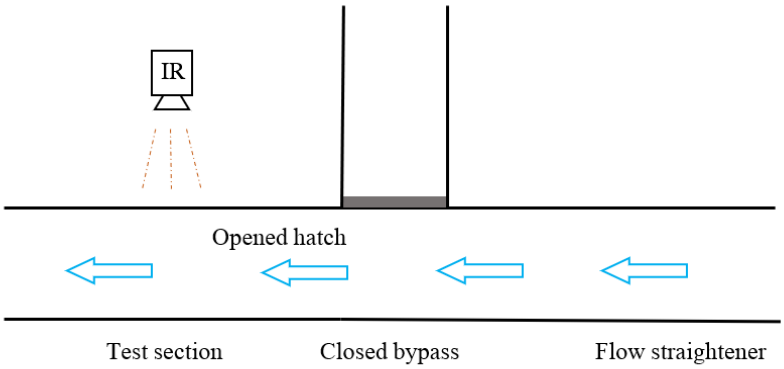

Figure 3.14: Schematic configuration of the flow behaviour when the bypass is closed and the hatch is opened

3.5.2 Components

The main components of the test rig will be described in the following section. This can be useful for a deeper understanding of the working principle, but more information can be found in literature.

- **IR camera**: the model in use for the experiments is a *Titanium 560M by Cedip Infrared Systems* specifically designed for academic and industrial R&D applications to have high sensitivity, accuracy, spatial resolution and speed at an affordable cost. The camera is coupled with the software *FLIR ResearchIR*, which allows a easy interface for the user in order to acquire IR data and change settings. The camera settings can be found in Table 3.16.

Figure 3.15: IR camera and Calibration Device

IR Camera Type	*Titanium 560M*
Sensor Type	$InSb$
Waveband	$3-5\ \mu m$ *or* $8-12\ \mu m$
Pixel Resolution	640×512
Integration Time	$1200\ \mu s$
Frame Per Second (FPS)	$10\ Hz$
Calibration Temperature Range	$-15 \div 110°C$
Calibration Device	*Dias CS110*

Table 3.16: IR camera technical characteristics

- **Heater**: The heater consists of a power supply system connected to some resistors to heat the main duct. By controlling the power supply, it is possible to regulate the temperature of the air inside the duct, allowing us to have different Re in the test section.

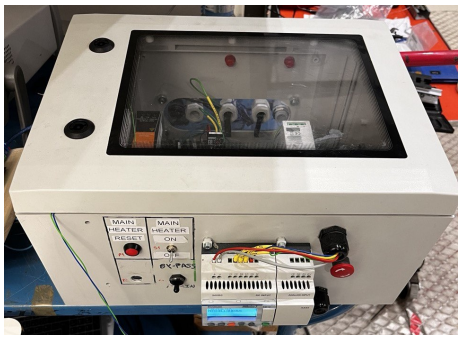

Figure 3.16: Inside the heater control there is a thermal relay and a power control system plus the electronic to make the air heater work

- **Flow straightener**: the flow straightener is located upstream of the test section and is used to align the main flow with the flow direction. It is 190 cm long, 17 cm wide and 12 cm high.

- **Three-way valve**: it is an Aluminum block with a pneumatic actuator that applies a torque for the opening or closing of the hatch. The bypass consists

of a pipe that releases the warmed up air in atmosphere when the desired temperature hasn't been reached, thus when the hatch is closed;

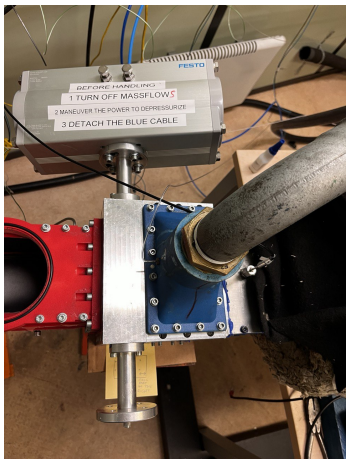

Figure 3.17: Three way valve

- **Test section**: the core of the test-rig is the test section, mainly composed of a rectangular duct with a bottom plate in which the 3D printed rough surfaces are positioned (in total there are 5 plates) and a top plate that can be found in two configurations: one with five windows and one with four windows, as it can be seen in Figure 3.19. The configuration depends from the region of the plate that wants to be investigated. For instance, if the entire central part of the plate needs to be studied the five windows top plate will be chosen, while if the connective part between two plates wants to be studied the four windows top plate will be used. The test objects, i.e. rough or smooth surfaces on the bottom plate, can be changed manually by unscrewing some allen screws. The geometric dimensions of the test section are given in Table 3.17.

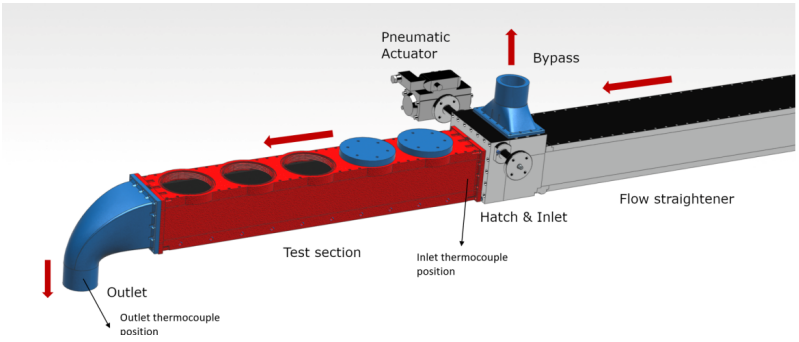

Figure 3.18: Schematic representation of the test rig

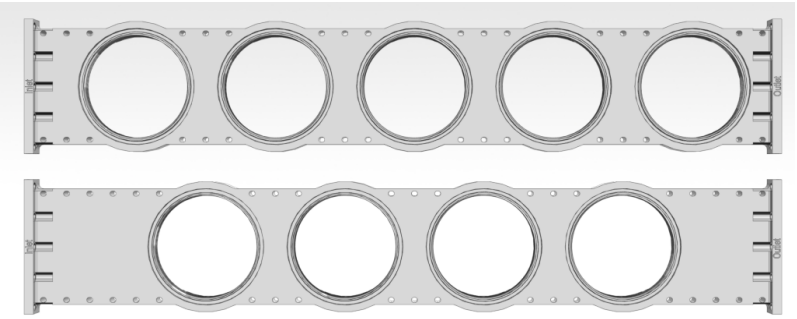

Figure 3.19: Top plates

Length	81.5 cm
Internal height	9 cm
Internal width	10 cm

Table 3.17: Geometric characteristics of the test section

- **Thermocouples**: the thermocouple used for this experiment are type K with technical features reported in Table 3.18. The thermocouple working principle is based on the Seeback Effect. This effect states that when a closed circuit is formed by jointing two dissimilar metals at two junctions, and junctions are maintained at different temperatures then an electromotive force (e.m.f.) is induced in this closed circuit. The amount of induced e.m.f. is different for different metal combinations and is proportional to the temperature difference of the junctions. This is the basic thermocouple working principle.

Temperature range	
Thermocouple grade wire	$-270 \div 1260$
Extension wire	$0 \div 200$
Accuracy	
Standard	$\pm 2.2°C$
Special limits of Error	$\pm 1.1°C$

Table 3.18: Technical characteristics Thermocouple type K

- **Data Acquisition System (DAS)**: every DAS is made of sensors to measure

a physical quantity, a signal conditioner that filters and reduce the noise amplifying the signal if needed, an Analogue-to-Digital device to convert analog signals to digital (bit) and a Laptop with an integrated software to visualize and store data 3.20. Figure 3.21 shows the Data Acquisition Systems used

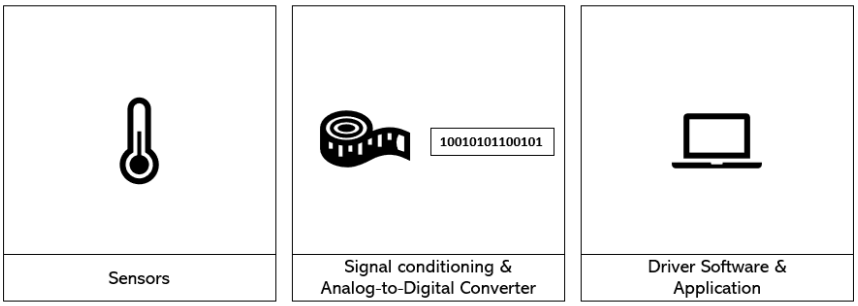

Figure 3.20: Data Acquisition System block diagram

in the present investigation. The pressure are measured with a 16-channel piezoresistive transducer. The device is a *Netscanner 9116* (Figure 3.21a) with an accuracy of $\pm 0.05\%$ FS and a pressure ranging between $-5860 \div 5860$ kPa. More features can be found in the user data-sheet [48]. The measured values are calibrated using a precision measurement instrument, i.e. a *Rosemount 2088 Absolute and Gauge Pressure Transmitter* (Figure 3.21b). The main features can be found in the user data-sheet [49]. The devices are connected to an *Agilent 34972A* data logger (Figure 3.21c) that is the main interface with the laptop where *RigView* is used to collect the data. This software is an in-hose data collection software similar to *LabView* and allows to log temperature and pressure data and collect them in a *.txt* file. For the mainflow temperature measurement a *Datascan 7220 Measurement Processor* (Figure 3.21d) with 16 bit resolution converts an analogue voltage, measured by the thermocouples Type K, in a digital signal .

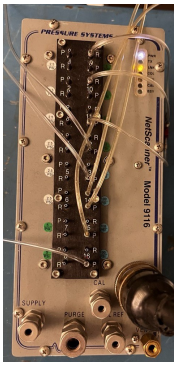

(a) Netscanner 9116

(b) Rosemount 2088 Absolute and Gauge Pressure Transmitter

(c) Cumulative Density Function

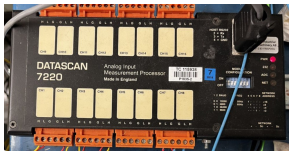

(d) Datascan 7220 Measurement Processor

Figure 3.21: Data Acquisition Systems

3.6 Data Acquisition

When explaining the data acquisition it is fundamental to clarify what data are acquired, as well as how the process of acquisition is carried out to understand how to use the acquired data. Despite the difference in the post processing of the data between smooth surfaces and rough surfaces, the acquired data are the same.

3.6.1 Test Preliminaries and Steps

In the present study, to keep in line with my predecessor, the experiments have been conducted at four different Reynolds numbers, respectively $Re = 10000$, $Re = 15000$, $Re = 20000$, $Re = 25000$. From Equation 3.36, as the hydraulic diameter D_h and the cross section A are constants of the channel found in Table 3.17, the Reynolds number is only defined by the air viscosity μ (i.e. the air temperature T_∞), which can be calculated from Sutherland's law with Equation 3.37 using T_∞, and the air mass flow $\dot{m}$, which can be regulated through a valve and it is measured through an orifice meter.
The experiment was conducted according to the following steps:

1. Positioning the IR Camera to the location of interest;
2. Opening the mainflow valve and checking for leakages in the test section;

3. Setting the flow to bypass by closing the test section with the hatch;
4. Activating the flow heater and monitoring the flow temperature rise;
5. Opening the hatch and starting the recording once the desired temperature is reached;
6. Deactivating the flow heater and setting the flow to bypass after td has passed.

The recording time was set to $t = 110\ s$ according to the semi-infinite hypothesis which requires to avoid the bottom plates reaching the main flow temperature. Moreover, the frame rate was set to 10 Hz which means that for each second 10 pictures/frames are captured.

Each run of the experiment could only be conducted for one window of the top plates. This means that in order to capture the whole length of the test section for one Reynolds number, nine separate runs had to be performed including a change of top plates in the meantime.

3.6.2 Acquired Data

Taking into consideration Equations 3.22 3.34, which are respectively the underlying equation used for the smooth plates and the equation used for rough plates, the unknown variable is in both cases the HTC which is then used to determine the Nusselt number through Equation 3.43

$$Nu = \frac{hD_h}{k_{air}} \tag{3.38}$$

The thermal diffusivity α_{air} and thermal conductivity k_{air} of the air are constant properties and can be looked up in online data sheets. Their values can be found in Table 3.19

α_{air}	$2.17 \cdot 10^{-5}\ \left[m^2/s\right]$
k_{air}	$0.029\ \left[W/(m \cdot K)\right]$

Table 3.19: Air thermal properties

Consequently, the needed data to extract local Nusselt and HTC are the wall temperatures over the plates in different positions along the channel and the bulk

temperature of air at the inlet and outlet of the channel. The wall temperature data are indirectly measured through the IR camera for each window i.e. positions along the channel. The video provides the time history of the radiometric signal converted in temperature through Equation 3.10 for each pixel (depending on the camera resolution).
The time history of bulk temperature T_∞ is measured through two thermocouples Pt100 type K positioned at the center of the outlet and inlet of the channel where the temperature can be approximated to the bulk temperature of the air. These values are key to determine the air temperature over the plates at different positions, which is performed with a linear interpolation, considering the temperature of the main flow varies linearly along the channel. The raw bulk temperature data at inlet and outlet are recorded in the software *RigView*, stored in a *.txt* file and imported into *Matlab* after the experiment.

To sum up, once fixed the Reynolds number, a video for each of the nine windows is recorded. For each frame of the video the raw data, presented in Table 3.20 and later used in the post processing, corresponds to a matrix of radiometric digital signal which is converted in wall temperature values T_w using the calibration equation $F_{S\to T}$ for each pixel. Thus the matrix will have as many elements as the camera resolution. Furthermore, the time history of the bulk temperature at inlet and outlet of the channel is acquired and stored in a *.txt* file.

Frame = ...		
Flow Settings	$T_\infty = \ldots$ $\dot{m} = \ldots$ $Re = \ldots$	
Acquired Data	*Wall Temperature*	*Bulk Temperature*
	$T_{w_{m\times n}}$ (matrix)	$T_{\infty_{inlet}} = \ldots / T_{\infty_{outlet}} = \ldots$

Table 3.20: Preliminary example of acquired data for each frame of the recorded video at given flow settings

The next step is to reduce the values of wall temperature data to the number of points included inside the ROI. These will be the values used in the post processing to determine the HTC. To accomplish so, a mask is applied using *Matlab*.

3.7 Post-Processing

In this section, the post-processing procedure for 1D solver and 3D solver will be presented in order to understand how we get from the raw data, underlined in the previous section, to the resulting HTC. There is a mechanical procedure to elaborate the acquired data, which leverages *Matlab* and *Python* codes to calculate the HTC.

3.7.1 General Procedure

Before going into the fundamentals of the smooth and the rough solvers, a general post-processing procedure has to be explained to achieve a better understanding. This phase includes the video processing and the bulk temperature processing. In fact, for the HTC computation the procedure differs for smooth and rough plates as already stated many times.

3.7.1.1 IR Video Processing

In the IR imaging software used, *FLIR's ResearchIR*, the video was stored and displayed as *.PTW* file. The first step was to determine the start frame of the experiment. This was made possible by means of a light bulb placed near the IR Window and connected to the switch which controlled the pneumatic actuator. At the start of the experiments, a flashing light could be easily detected in the recording, as shown in Figure 3.22a. The second step was to select the region of interest (ROI).

(a) Captured frame (b) ROI mask

Figure 3.22: ROI selection example

In each frame with resolution of 640×512 pixels, not only the lower plate of the test section was captured, but also the area around the IR Window, as shown in Figure 3.22a. For the calculation of the HTC, only a specific region of the image was of interest. The location was determined manually by placing an ellipse on the ROI. A mask containing binary information about the ROI was then exported, resulting in a black and white image as shown in Figure 3.22b. For this ROI the digital level of

the radiometric signal is translated into wall temperature data using the calibration function $F_{S \to T}$.

3.7.1.2 Bulk Temperature Processing

The bulk temperature T_∞ at the inlet and outlet of the channel was previously stored in a *.txt* file, as explained in Section 3.6.2. Taking into consideration Equation 3.22 and 3.34 the bulk temperature over every plate at every time-step is needed to calculate the HTC. Assuming the bulk temperature varies linearly along the channel, and assuming the response during time is roughly the one showed in Figure 3.24, for each time-step the bulk temperature above the desired plate is calculated by linear interpolation, where Δx is the distance between two windows, w is the number of the tested window, and L is the channel length.

$$T_{\infty,w} = T_{\infty_{inlet}} - (T_{\infty_{inlet}} - T_{\infty_{outlet}}) \frac{\Delta x \cdot w}{L} \tag{3.39}$$

3.7.2 1D Solver Post-Processing

The 1D solver for heat conduction uses Equation 3.22, applied in the ROI selected in the video, to calculate the only unknown variable of the problem: the HTC. The local wall temperature for each pixel varies in time as shown in Figure 3.23. Also, the mainflow temperature, i.e. the bulk temperature, varies in time as well as in space. Assuming the mainflow temperature to vary within limited time-steps as shown in Figure 3.24, the Duahamel solver can be used in accordance with the work done by Metzger and Larson [50]. In this case the mainflow temperature over each window is approximately given by several discrete temperature step changes $\Delta T_{\infty_{j,j-1}}$. Thus, the difference between the wall temperature and the initial temperature for each time-step can be expressed by Equation 3.40. Where the term $U(t-\tau_j)$ is given by Equation 3.41.

$$T_w - T_i = \sum_{j=1}^{N} U(t-\tau_j) \Delta T_{\infty_{j,j-1}} \tag{3.40}$$

$$U(t-\tau_j) = 1 - \exp\left(\frac{h^2}{k^2}\alpha(t-\tau_j)\right) erfc\left(\frac{h}{k}\sqrt{\alpha(t-\tau_j)}\right) \tag{3.41}$$

Combining Equations 3.40 and 3.41 the main solver equation can be obtained.

$$T_w - T_i = \sum_{j=1}^{N} \left[1 - \exp\left(\frac{h^2}{k^2}\alpha(t-\tau_j)\right) erfc\left(\frac{h}{k}\sqrt{\alpha(t-\tau_j)}\right)\right] \Delta T_{\infty_{j,j-1}} \tag{3.42}$$

This equation must be solved for the unknown variable h, thus it requires a non-linear solver. By using the `fsolve` function in *Matlab*, implemented for non linear

systems of equations in the form of $F(\mathbf{x}) = 0$, the non linear equation is solved for each pixel in the ROI, obtaining the local HTC over the smooth plate in the desired window.

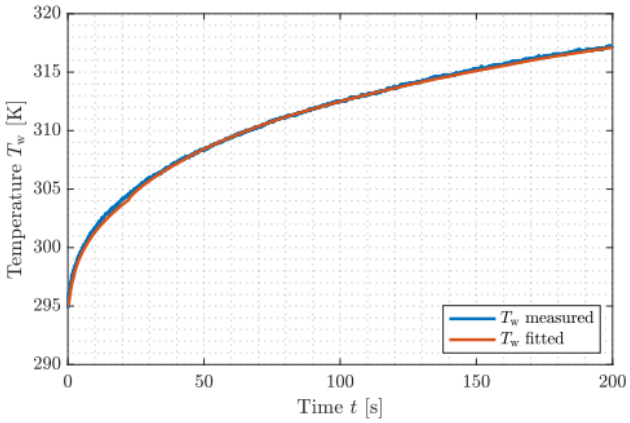

Figure 3.23: Variation in time of the wall temperature for one pixel. The calculated wall temperature fits the measured one with an accuracy of $R^2 = 0.99$

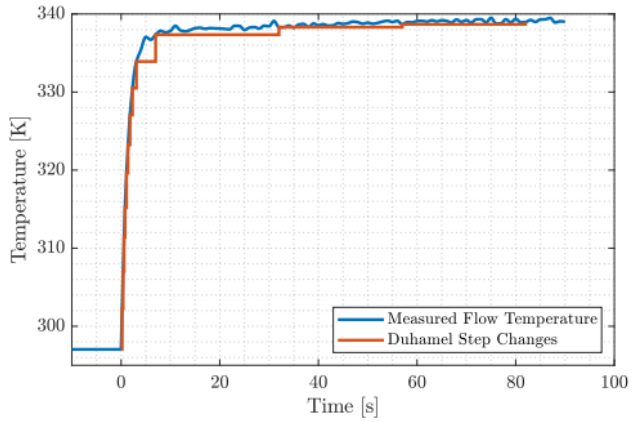

Figure 3.24: Variation in time of the mainflow temperature, i.e. bulk temperature

The Nusselt number for every pixel in the ROI is then calculated through the Equation 3.43

$$Nu = \frac{hD_h}{k_{air}} \tag{3.43}$$

Furthermore, the HTC and Nusselt number needs to be laterally averaged along each position x_i in streamwise direction. This means that for every line of pixels perpendicular to the streamwise coordinate, thus along each x_i, the HTC and Nu

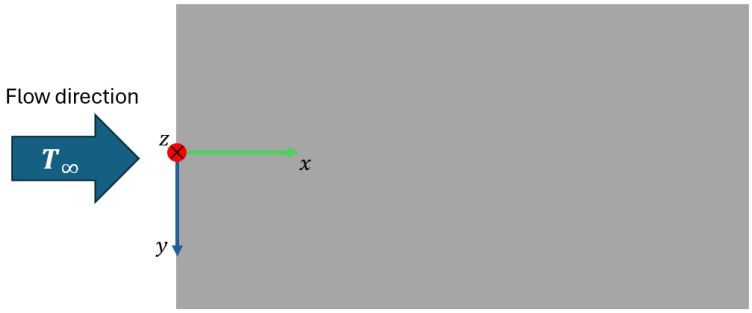

Figure 3.25: Visualization of the coordinates: z is perpendicular to the surface, x is the streamwise coordinate, and y to close the system

are averaged. This process is carried out for each window as in Equation 3.44 3.45

$$\overline{h_i} = \frac{\sum_{j=1}^{N} h(x_i, y_j)}{N} \tag{3.44}$$

$$\overline{Nu_i} = \frac{\sum_{j=1}^{N} Nu(x_i, y_j)}{N} \tag{3.45}$$

From the laterally averaged values the global average for each window can be calculated averaging the values on the streamwise direction

$$\overline{h_0} = \frac{\sum_{i=1}^{M} \overline{h_i}}{M} \tag{3.46}$$

$$\overline{Nu_0} = \frac{\sum_{i=1}^{M} \overline{Nu_i}}{M} \tag{3.47}$$

An example for one window can be seen in Figure 3.26.

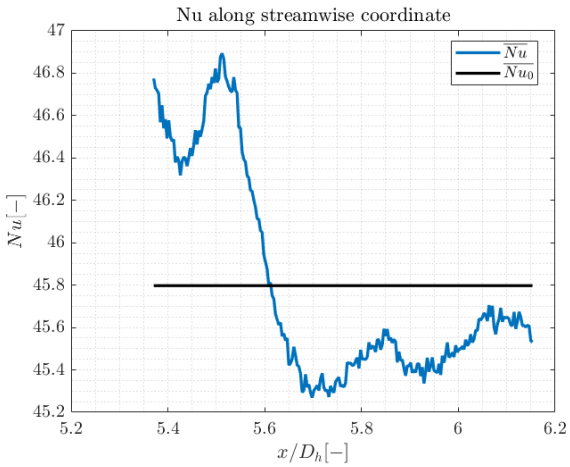

Figure 3.26: Laterally averaged Nusselt $\overline{Nu}$ and globally averaged $\overline{Nu_0}$ for a window

3.7.3 3D Solver Post-processing

The approach is different in the case of rough surfaces due to the presence of 3D effects, which are not taken into account in Equation 3.42. At the beginning, the IR Videos are processed following the procedure previously described in Section 3.7.1. Subsequently, the measured wall temperature, obtained by converting the radiometric signal measured by the IR Camera using Equation 3.10, is used in the *C3D* solver along with the bulk temperature, obtained by linear interpolation, to solve the adjoint problem. This procedure is carried out in the built-in solver which allows to numerically calculate the local HTC, while comparing the calculated surface temperature with the measured one. The calibration proceeds for every time step ($t = 0\ 10\ 20\ 40\ 70\ 100\ [s]$), and stops when the residuals, i.e. the difference between calculated and measured wall temperatures, are under a certain tolerance, usually set to $tol = 0.5$.
Thus, the resulting HTC for every node in the model can be displayed and plotted for every Reynolds and each window. As it has been done for the smooth plates, the Nusselt number can be calculated through Equation 3.48 and plotted as in Figure 3.27.

$$Nu = \frac{hD_h}{k_{air}} \tag{3.48}$$

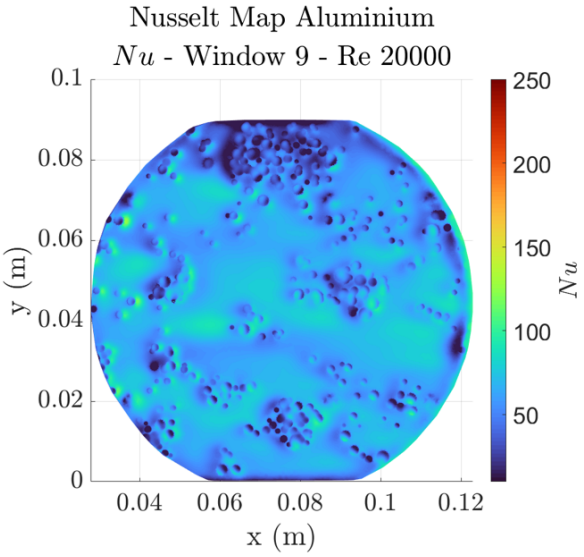

Figure 3.27: Example of Nusselt number plot in the ROI

Consequently, as it has been carried out for smooth surfaces, the HTC and Nusselt number are laterally averaged and globally averaged for each window at a given Reynolds. The Equations used are 3.44 3.45 3.46 3.47.

Chapter 4

Results

In the following chapter, the results will be presented. In the first part, the main focus will be on smooth surfaces with the objective to validate the rig by comparing the resulting globally averaged Nusselt number from experiments with the Gnielinski correlation. In the second part, the analogue *Aluminium* rough plates will be investigated. In particular the focus will be on the comparison with Kaibin's results obtained for *IN939*, the evaluation of the local HT enhancement, i.e. the ratio between the local Nusselt over the rough plates and the Nusselt of the smooth surface. This is done to discuss about the main effect of HT enhancement.

4.1 Smooth Surfaces

The smooth channel, with plates covered in thermal paint, has been tested for four different Reynolds numbers. The HTC for the entire bottom surface at each window has been characterized as well as the lateral average trend in the streamwise direction. Furthermore, the Nusselt number in the last region of the channel, where the thermal boundary layer is supposed to be fully developed, has been compared with the Gnielinski correlation for thermally fully developed flows in smooth channels. All the results are shown in term of Nusselt number, since it is directly proportional to the HTC through the equation $Nu = \frac{hD_h}{k_{air}}$.

4.1.1 Nusselt Results

Using the calibration Equation 3.10, the wall temperature values over the plates have been determined. This, with the medium thermal properties and the bulk temperature measurements, allows to calculate the HTC distribution. Consequently, the Nusselt distribution on every window has been plotted using Equation 3.43, so

that the variation of the Nusselt along the streamwise coordinates can be visualized. The black side lines represent the edges of the channel and within them the interested region is studied. For a given Reynolds, the Nusselt number decreases going from the inlet to the outlet of the channel. On the other hand, for a given window, an increase in the Reynolds number results in an increased Nusselt number, i.e. heat transfer. This is as expected from theory and it is in line with the previous work of Lhemann and Wen [26] [27]. Only a limited number of windows have been tested due to an unavailability of the camera. However, the behavior of the Nusselt number over the smooth surfaces is as expected from theory, so one can properly guess the Nusselt value over the untested windows. The Nusselt decreasing trend along the channel

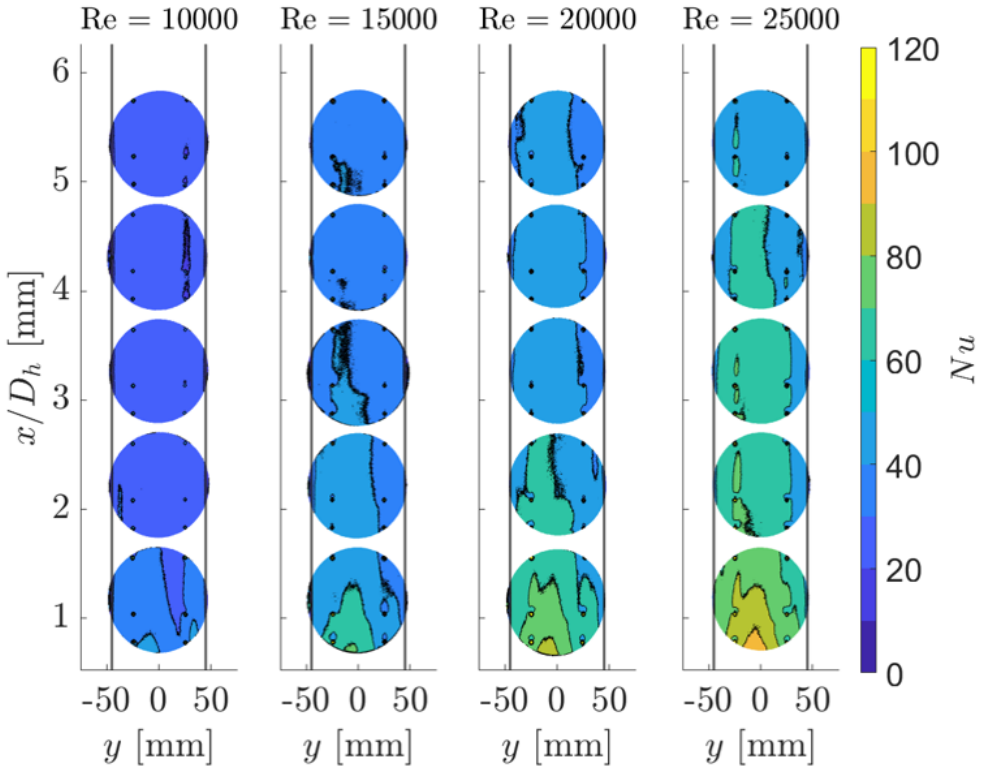

Figure 4.1: Contour plot over smooth surfaces for the different tested Reynolds numbers

can be appreciated looking at the laterally averaged Nusselt along the streamwise coordinate, as in Figure 4.2. At the inlet, the temperature step is translated into a high heat transfer, which in turns gives a high Nusselt. Further downstream, the thermal boundary layer starts to become more fully developed and the Nusselt decreases reaching a plateau. For example, at Reynolds 25000 the Nusselt value goes from $Nu \approx 85$ in the first window to around $Nu \approx 57$ in the last window. This decreasing trend tends to reach a plateau when the flow reaches the thermally fully

developed conditions, so when the Nusselt is constant along the streamwise channel direction. From theory, the higher the Reynolds the more downstream this plateau is reached. In fact, if looking at Reynolds 10000 the plateau seems to be reached at 4 diameters from the inlet, while at Reynolds 25000 the plateau is not reached in the last window. However, the HTC and Nu values seem to stabilize around $x/D_h \approx 5$ with a tendency to decrease more. Since entry lengths for turbulent flow are typically short, around 10 diameters from the inlet, it is often reasonable to assume that the average Nusselt number for the entire channel is equal to the value associated with the fully developed region. In our case of study, the channel is not long enough to reach this value. This would explain the reason why the Nusselt have a tendency to slightly decrease also in the last portion of the channel. However, the values seem to be stable and only a small decrease can be expected. Furthermore, the higher the Reynolds number, the higher the heat transfer, thus the Nusselt number. This can be seen considering a given position downstream, and increasing the Reynolds number. For example, for $x/D_h \approx 0.45$, which is around half of the channel, the globally averaged Nu increases from $\overline{Nu_0} \approx 37$ to $\overline{Nu_0} \approx 74$ going from $Re = 10000$ to $Re = 25000$.

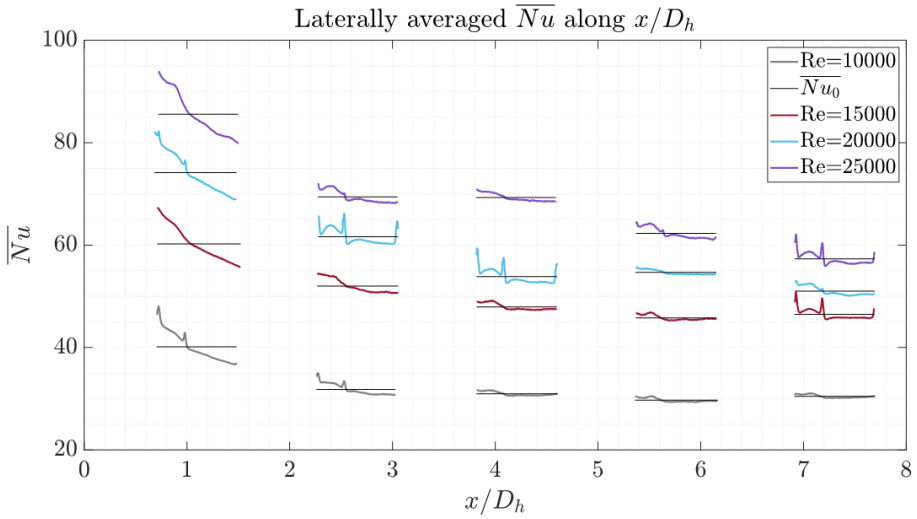

Figure 4.2: Plot of the laterally averaged $\overline{Nu}$ and the globally averaged $\overline{Nu_0}$ along the streamwise coordinate for different Reynolds numbers

4.1.2 Validation of the Test Rig

The validity of heat transfer results for the channel needs to be investigated. To accomplish so, Mills [51] approach for smooth channels with long calming section was used. In our study, the last portion of the channel is considered to be slightly in

the thermally fully developed region. Thus, the globally averaged Nusselt number $\overline{Nu_0}$ in this portion can be compared with one of the in literature correlations, such as Dittus-Boelter or Gnielinski, valid for a fully developed flow condition. The latter is used in the following form:

$$Nu_\infty = \frac{(\lambda/8)(Re-1000)Pr}{1+12.7\sqrt{\lambda/8}(Pr^{2/3}-1)}\Big[1+\Big(\frac{D_h}{L}\Big)^{2/3}\Big]K \tag{4.1}$$

Which is considered as the Nusselt number at the position x if no entry effects are present.The friction factor λ and the costant K are calculated as in Section 2.6.3. The length of the channel L is considered to be the distance between the inlet and the center of the last window, and the Prandtl number is the values for the air $Pr = 0.71$.

Hence, the ratio $\overline{Nu_0}/Nu_\infty$, calculated for the last portion of the channel,i.e. the last window, is an indicator of the validity of our results with respect to a channel with fully developed heat transfer conditions. The comparison of this values are shown in Table 4.1. With and uncertainty of Gnielinski's correlation around 25%,

Re	$\overline{\mathbf{Nu_0}}$	$\mathbf{Nu}_\infty$	$\overline{\mathbf{Nu_0}}/\mathbf{Nu}_\infty$ [%]
10000	30.46	37.30	18.35
15000	46.47	51.45	9.67
20000	51.01	64.38	20.77
25000	67.40	76.53	11.94

Table 4.1: Comparison between globally averaged Nusselt $\overline{Nu_0}$ and Gnielinski correlation Nu_∞

we can consider our results valid in the range of the experimented Reynolds. For instance, the experimental data are in general lower than Gnielinski's results, but they are always within the range of uncertainty.

The experimental results have been correlated with a least square method as in Equation 4.2, resulting in a mean deviation of 3%. It was not possible to find a correlation as Gnielinski because more data points are needed. Thus a Dittus-Boelter-like correlation has been used [52].

$$\overline{Nu_0} = K \cdot Re^a \cdot Pr^b \tag{4.2}$$

The values of the constants are $K = 0.0181,\ a = 0.8272$, and $b = 0.33$ respectively. In Figure 4.3, the least square regression, with $R^2 = 0.9887$, is plotted over the

acquired data. Since the Prandtl effect is not relevant for air, because Prandtl is number is constant at low temperatures, the only important exponent is a. Its value is in line with other in literature results for turbulent flows over smooth channel, where usually $a = 0.8$ is accepted.

Eventually, the ratio $\overline{Nu_0}/Nu_{\infty_{mine}}$ is plotted for all the dimensionless positions

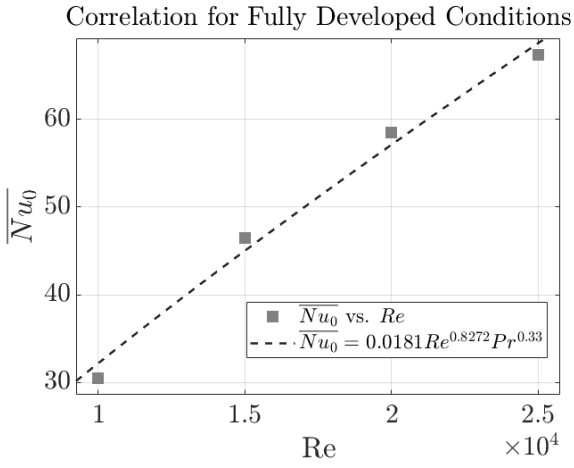

Figure 4.3: Correlation of heat transfer under fully developed conditions

x/D_h to grasp a full understanding of the entrance region effect. Figure 4.4 , takes inspiration from [51] results. At the inlet $x/D_h \approx 0$, the heat transfer tends to have high values because of the sudden step change in temperature. Proceeding downstream, the values of the ratio $\overline{Nu_0}/Nu_{\infty_{mine}}$ tend to reach a plateau close to the unity. Some errors in the measurements can affect the results, but they are still within the range of uncertainty given by Gnielinski. This remarks the validity of considering the last portion of the channel as thermally fully developed. Furthermore, as highlighted in Section 2.6.3, the entrance region is longer for higher Reynolds numbers.

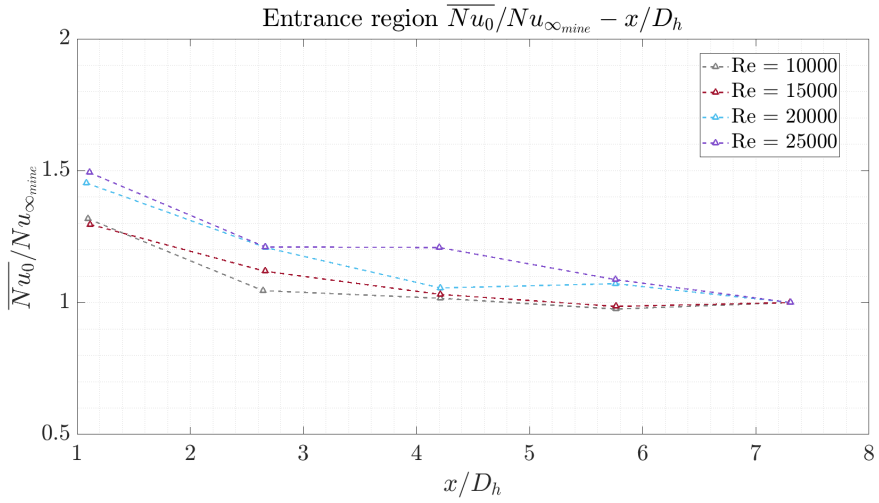

Figure 4.4: Values of the ration $\overline{Nu_0}/Nu_{\infty_{mine}}$ along the streamwise dimensionless coordinate

4.2 Rough Surface

The rough surface results for the *Aluminium* are firstly presented to understand the general behaviour along the streamwise coordinate. These results are later used for a comparison with smooth and *Inconel 939* in terms of laterally averaged Nusselt. To conclude, the local Nusselt enhancement is studied to understand the main effects of heat transfer enhancement.
As in the previous section, only the Nusselt number results are presented, since it's directly proportional to the HTC through Equation 4.3.

$$Nu = \frac{hD_h}{k_{air}} \tag{4.3}$$

4.2.1 Nusselt Results

The laterally averaged Nu has been plotted over the dimensionless streamwise coordinate. As in the smooth channel the decreasing trend from the inlet to the outlet is confirmed. For instance, under Reynolds 25000 the Nusselt goes from a value of $Nu \approx 100$ to $Nu \approx 80$. This is due to the entrance region effect. Accordingly with what said for smooth results, the Nusselt is not constant in this region but tends to decrease until reaching a plateau over thermally fully developed condition. Furthermore, the higher the Reynolds number, the higher the heat transfer which in turns gives an increased Nusselt number. In $x/D_h \approx 5$, the Nusselt is $Nu \approx 40$ for Reynolds 10000 and reaches the value of $Nu \approx 90$ for Reynolds 25000. A new important feature in this graph is the presence of oscillations in the laterally aver-

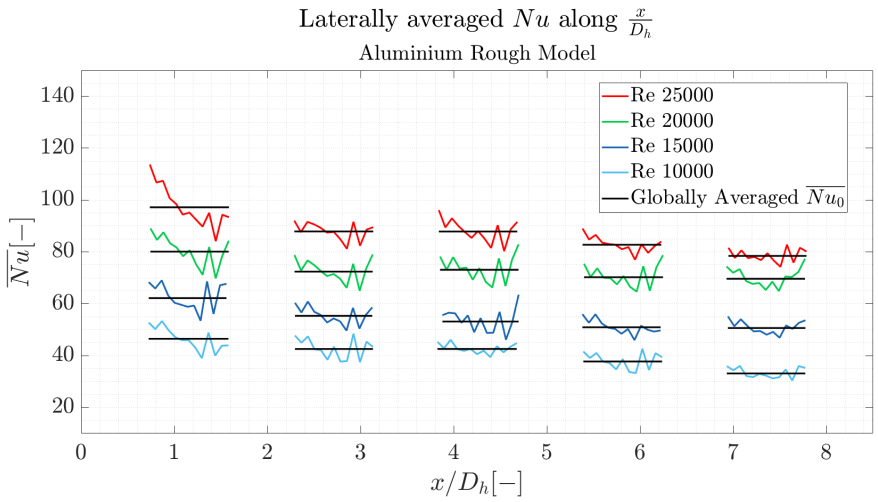

Figure 4.5: Laterally averaged $\overline{Nu}$ for all the tested flow conditions for the *Aluminium* rough surface model.

aged Nusselt. As expected, the rough elements creates a non uniform heat transfer condition over the plates. This is translated into a non uniform Nusselt distribution which can be appreciated in the Nusselt maps in Figure 4.6. The main reasons for this non omogeneus distribution are the effect of turbulence and vortices generated by the rough elements, but also the effect of the flow impacting directly on the rough elements.

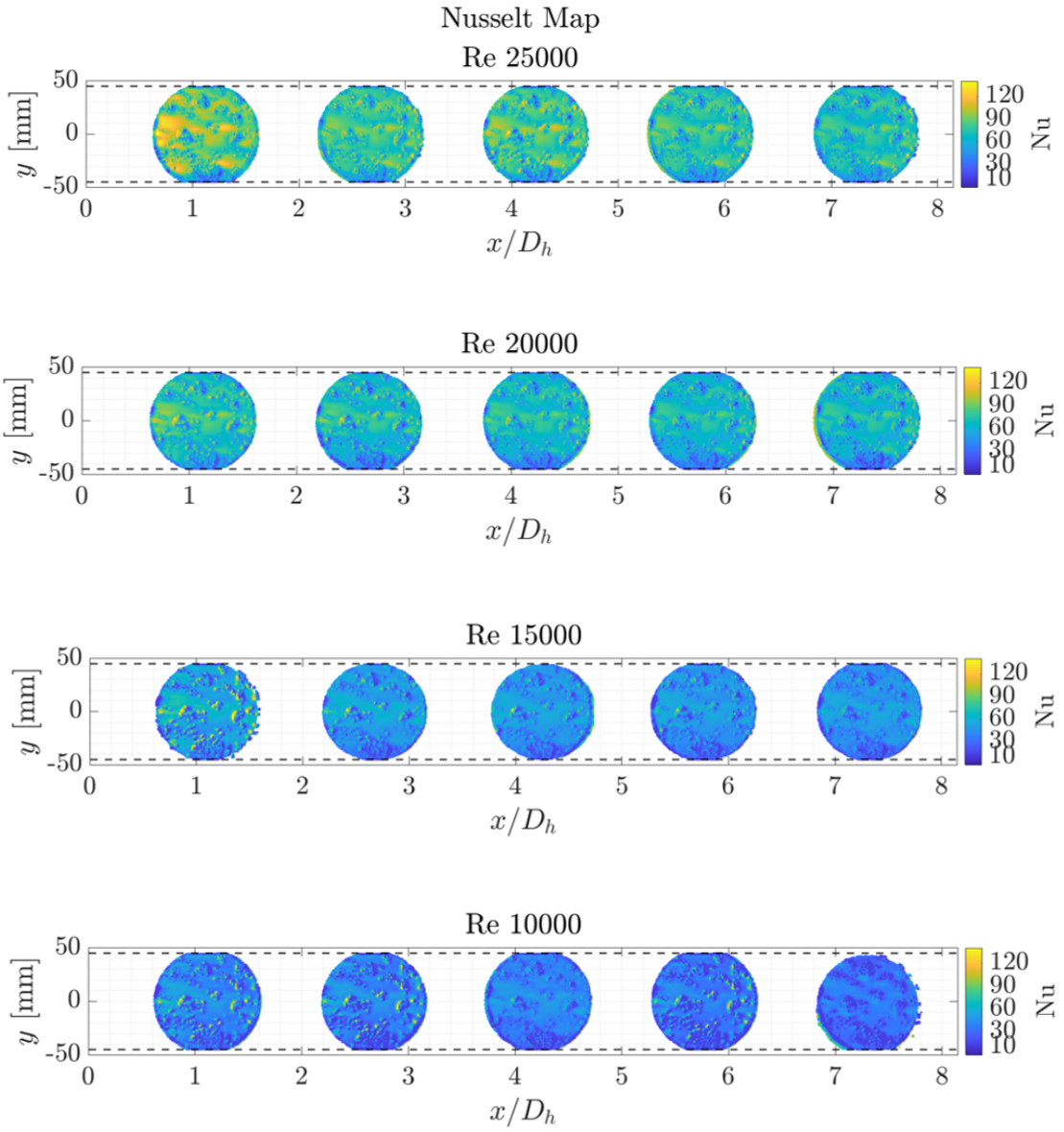

Figure 4.6: Local Nusselt distribution for all the tested flow conditions for the analogue rough surface

4.2.2 Comparison Smooth, Aluminium, Inconel 939

The main purpose of this section is to point out the differences in heat transfer over different materials models. For instance, *Inconel 939* is characterized by an high roughness, where little satellites are attached to big rough elements. On the other hand, *Aluminium* has wide smooth spots and little rough elements that tend to create some clusters. In Figure 4.7 we can see the real scale roughness over *Aluminium* and *Inconel*. Furthermore, considering the same analogue rough surface

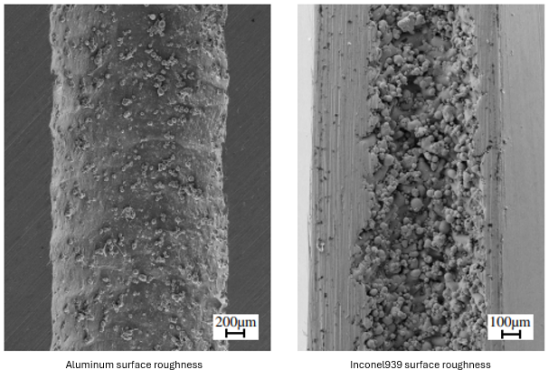

Figure 4.7: Real size roughness for *Aluminium* (left) and *Inconel 939* (right)

modelling, Figure4.8 shows the up-scaled version of this rough models. The smooth spots over the model are evident and very different from the highly concentrated roughness of *Inconel 939*.

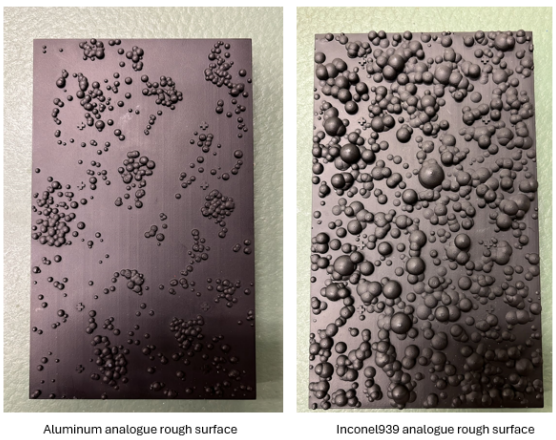

Figure 4.8: Comparison of analogue rough surface models for *Aluminium* (left) and *Inconel 939* (right)

The heat transfer over the different models, included the smooth channel, is very different. The higher the roughness, the higher heat transfer, i.e. the Nusselt number.

In Table 4.2 , are summed up all the parameters (matching with the real SR) for the two different materials in the up-scaled configuration. *Inconel 939* is characterized by the highest roughness.

Surface	$\mathbf{R_a}$ **[mm]**	$\mathbf{R_z}$ **[mm]**	$\mathbf{R_q}$ **[mm]**
Smooth	0	0	0
Aluminium	0.37	2.35	0.49
Inconel 939	1.10	5.74	1.30

Table 4.2: Surface roughness parameters for different materials in the up-scaled configuration

4.2.2.1 Laterally averaged Nu

This said, the results are shown in terms of laterally averaged Nusselt number over the dimensionless streamwise coordinate for all the different flow conditions.

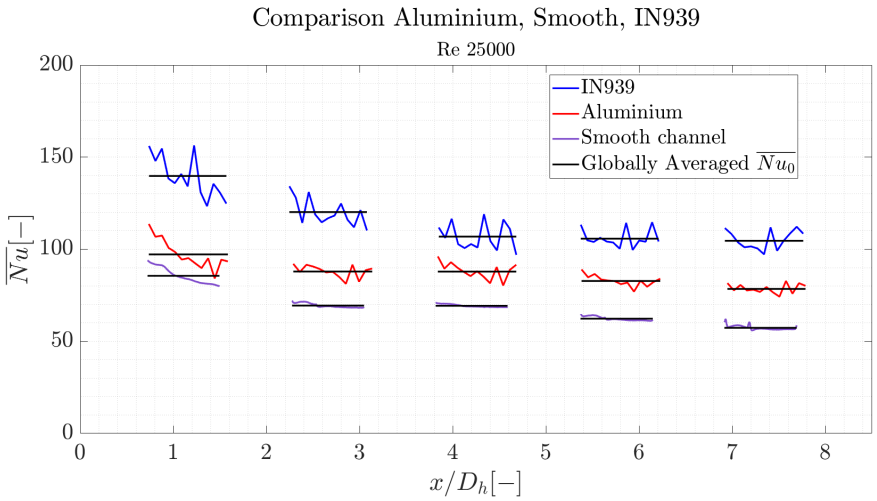

Figure 4.9: Laterally averaged Nusselt $\overline{Nu}$ for different analogue rough surface models at Reynolds 25000

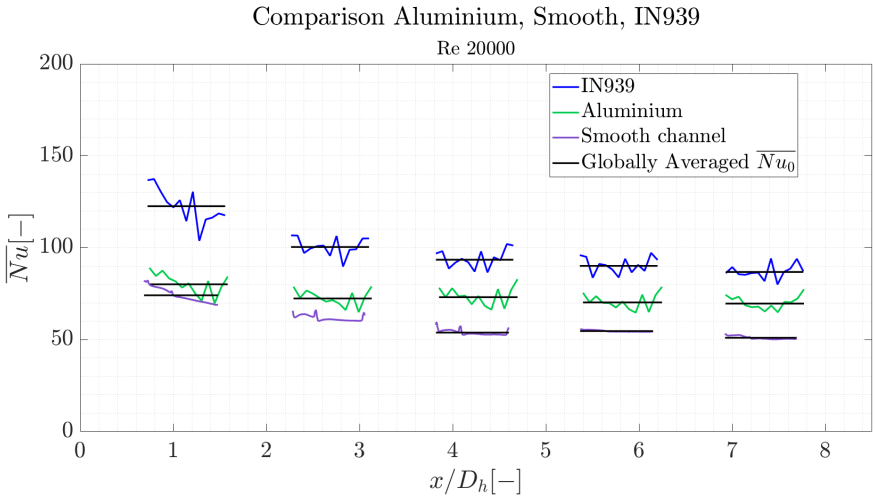

Figure 4.10: Laterally averaged Nusselt $\overline{Nu}$ for different analogue rough surface models at Reynolds 20000

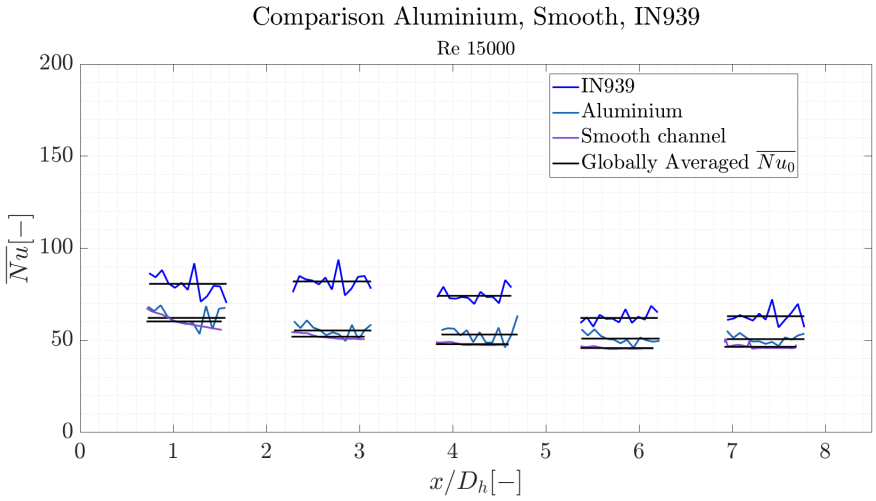

Figure 4.11: Laterally averaged Nusselt $\overline{Nu}$ for different analogue rough surface models at Reynolds 15000

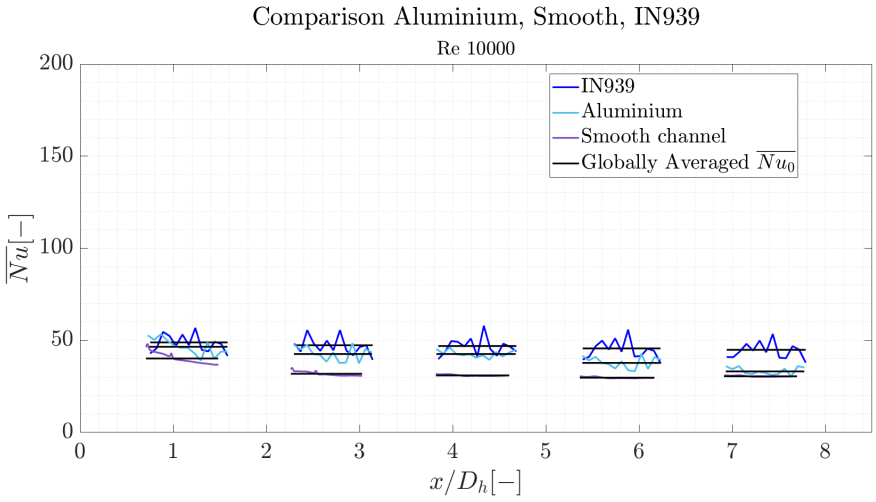

Figure 4.12: Laterally averaged Nusselt $\overline{Nu}$ for different analogue rough surface models at Reynolds 10000

There are several effects to take into account looking at Figures 4.12 4.11 4.10 4.9 :

- **Reynolds effect**: the Reynolds has a direct impact on the heat transfer, thus in the Nusselt number, for all the different roughness given by different materials. For instance, the higher the Reynolds number, the higher the Nusselt.
- **Entrance region**: the general pattern of the laterally averaged Nusselt number along the streamwise coordinate is characterized by the entrance region effect. At a given Reynolds, the Nusselt tend to decrease from the inlet to the outlet, until reaching a plateau. For lower Reynolds the entrance region is shorter with respect to higher Reynolds. This can be seen for every kind of roughness.
- **Relative roughness effect**: the most significant effect is the one given by the material type. It is known that an increased roughness leads to an increased heat transfer, i.e. Nusselt. This is confirmed in the course of this experimental investigation. In fact, the Nusselt number for *Inconel 939* stands upon *Aluminium*, which stands upon the smooth channel. Furthermore, an increased roughness brings higher oscillations in the laterally averaged Nusselt. This are given by the local variation of the HTC due to the presence of alternatively rough elements and smooth spots.

4.2.2.2 Local Thermal Characteristics

The local thermal characteristics are studied in therms of Nusselt number over the *Aluminium* and *Inconel 939* models. In particular, only the results for the last window are displayed, because it is considered to be in the thermally fully developed region. Besides the Reynolds effect, which has already been totally discussed, it is now fundamental to discuss the effect of the SR on the heat transfer. In Figures 4.13, 4.14, 4.15, 4.16, the local Nusselt is compared between the two SR models for all the tested flow conditions. The **flow direction** is from the right to the left.

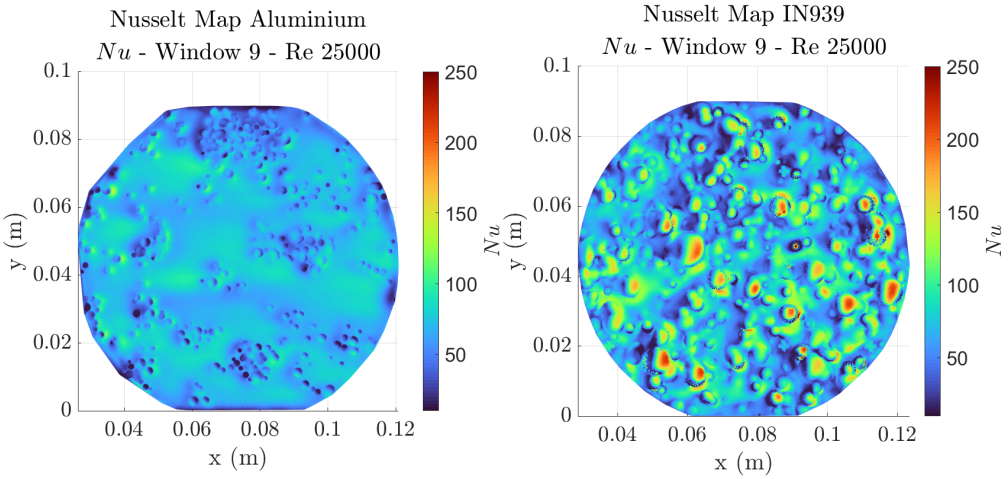

Figure 4.13

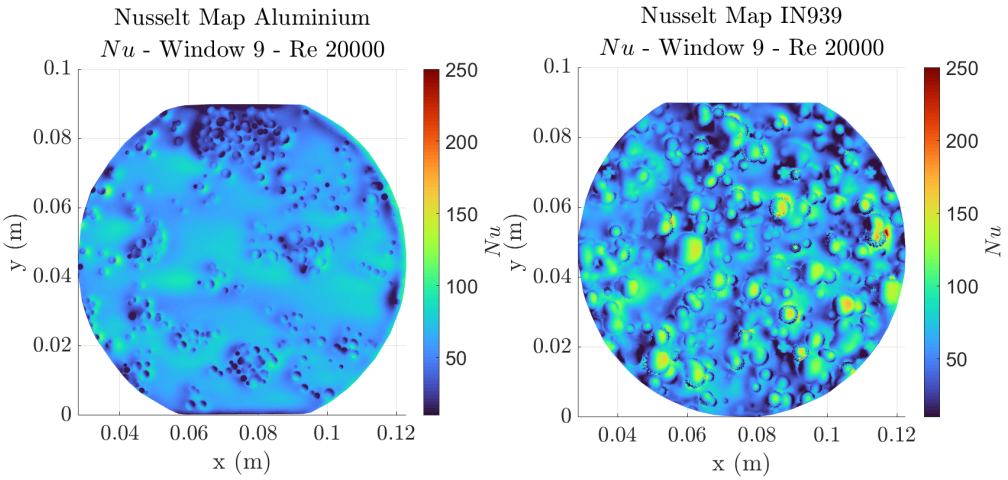

Figure 4.14

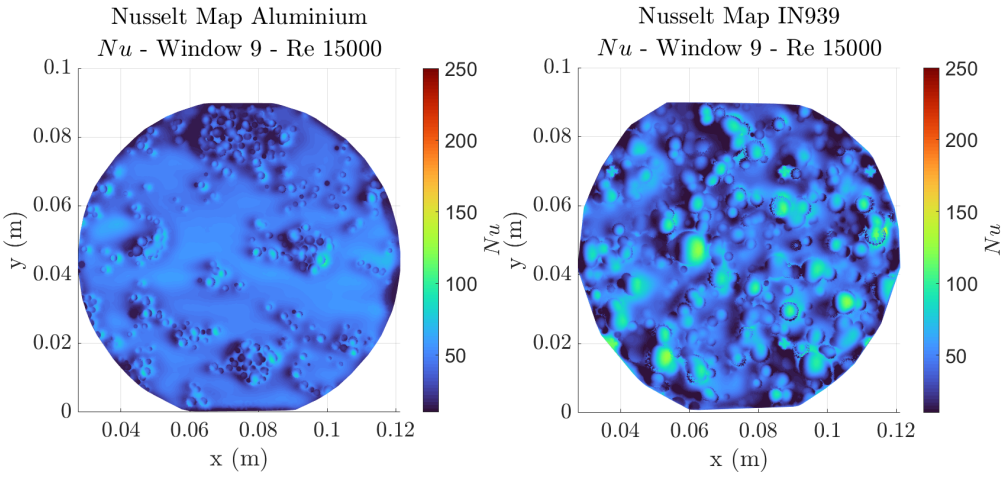

Figure 4.15

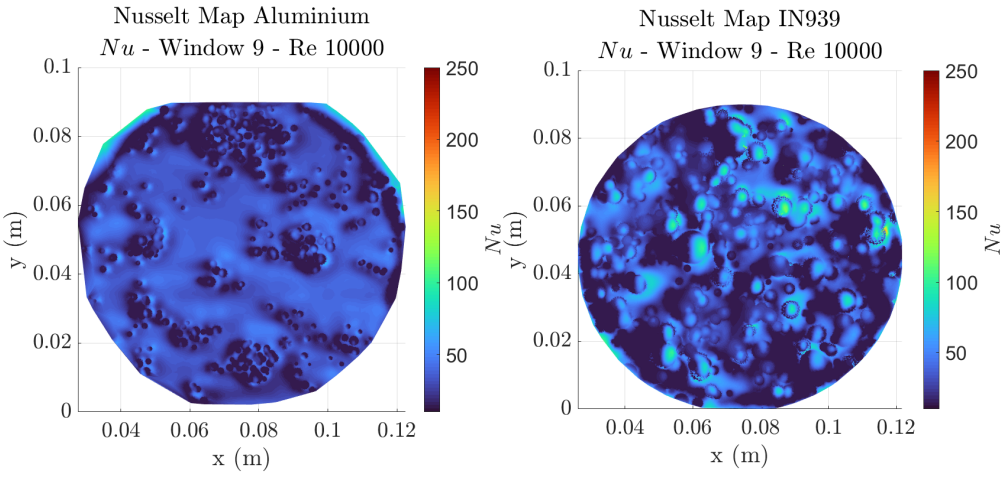

Figure 4.16

Focusing on $Re = 25000$ in Figure 4.13, the *Aluminium* presents lower values of heat transfer compared with *IN939*. In particular the wide smooth spots are characterized by low level of Nu. In contrast, *IN939* don't present considerable smooth spots. The rough elements invested by the air flow are characterized by higher Nu, but in some cases the HT in rough elements is clearly low. Without flow characterization over the rough surface, it is difficult to state whether the low Nu areas are related to corner flows, separated flow or other effects. The *IN939*, characterized by higher relative roughness than *Aluminium*, presents higher Nu on the rough elements directly invested by the air flow. This is due to a protrusion of the rough elements on areas where the velocity is higher.

4.2.2.3 Local Nusselt Enhancement

It is of high interest to understand the local HT enhancement with respect to the smooth surface results. The local Nusselt obtained for *Aluminium* and *IN939* are plotted over the smooth plates results. The ration $\frac{Nu_{rough}}{Nu_{smooth}}$ is fundamental to balance the effect of secondary flow and get a significant visualization of high or low HT enhancement areas.

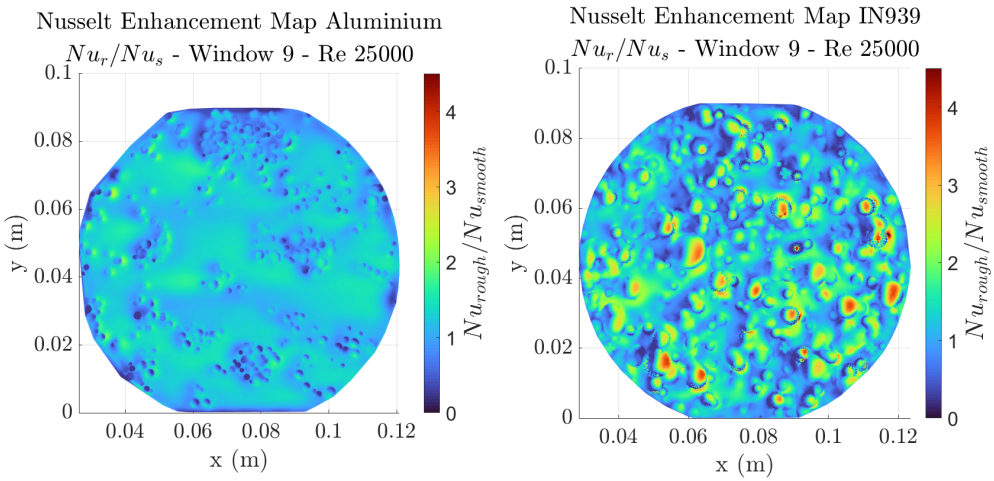

Figure 4.17

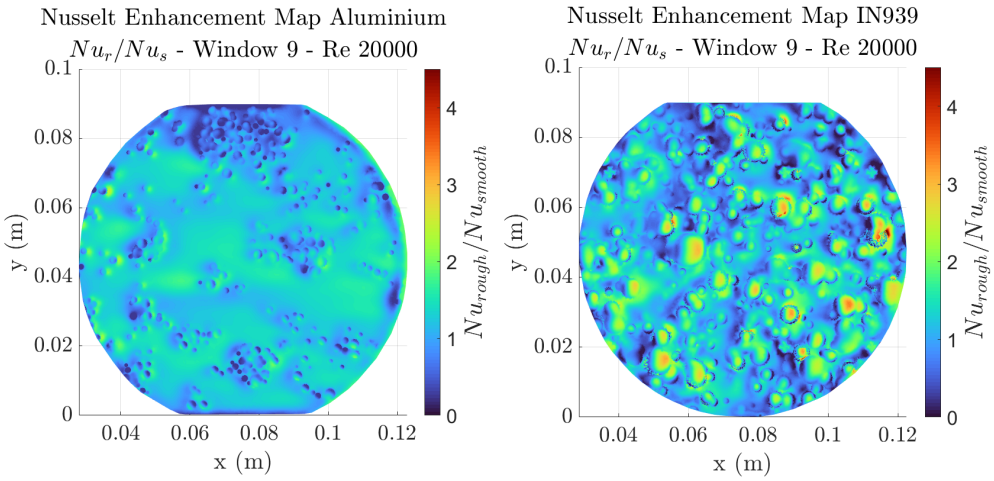

Figure 4.18

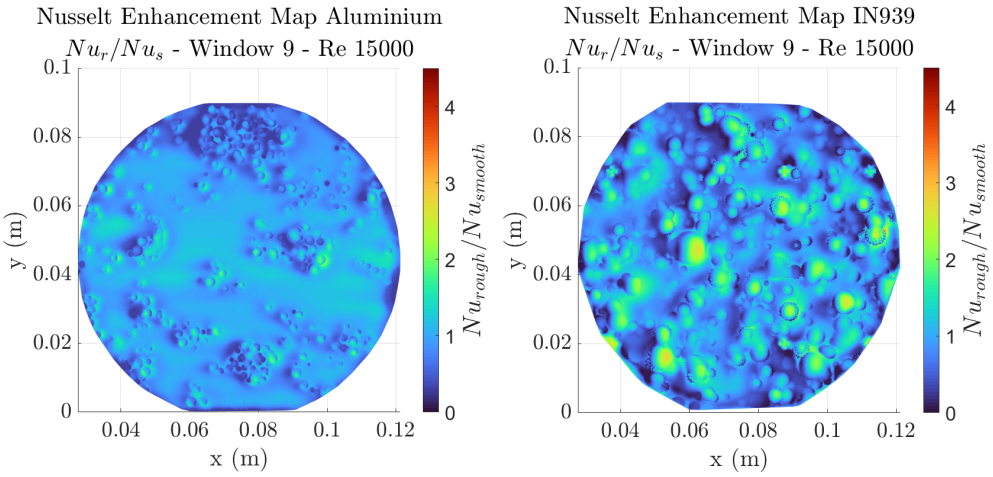

Figure 4.19

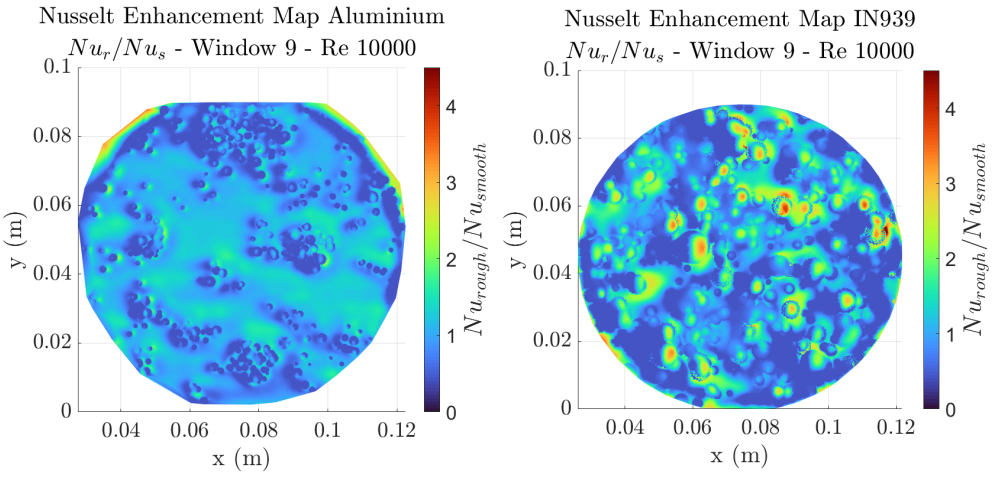

Figure 4.20

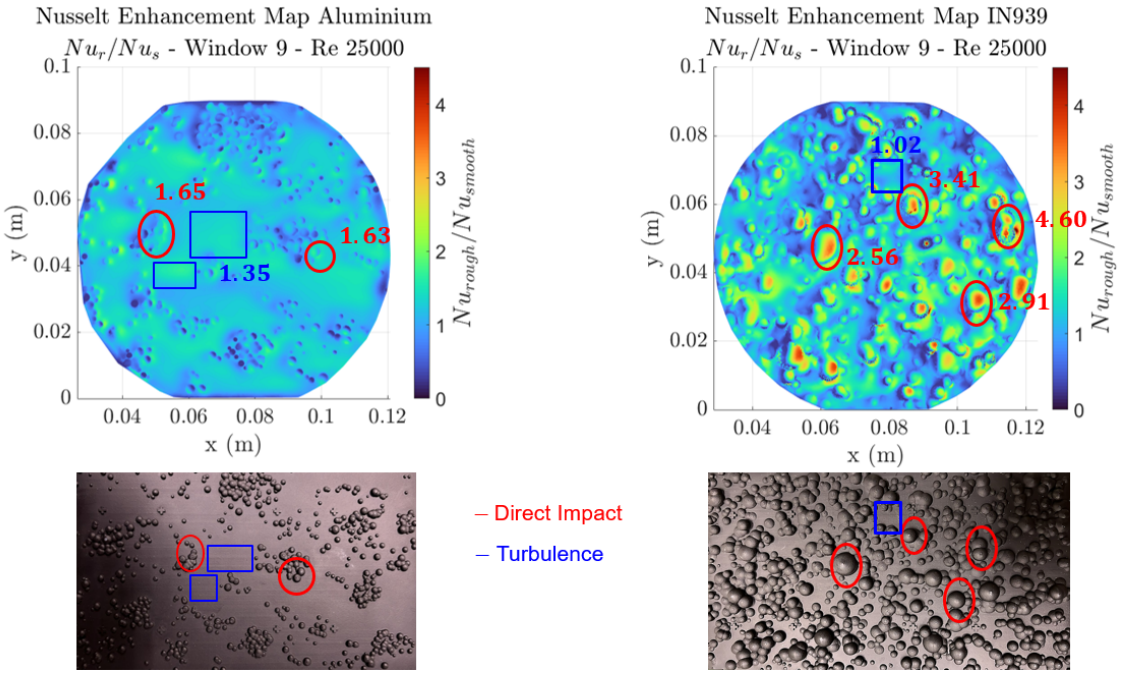

Figure 4.21: Local values of Nusselt enhancement and main effects

Looking into the maps for $Re = 25000$ in Figure 4.21, there are several considerations that can be done. First of all, the main effects to be observed are related to:

- **Turbulence**: the roughness induced turbulence, i.e. downstream vortices, is responsible for HT enhancement over smooth spots by increasing the wall shear stress, and consequently the heat transfer.
- **Direct impact**: the air flow impacting on the rough elements have a stagnation point where the heat transfer is at its peak. The higher the velocity the higher the heat transfer.

Understanding where one effect is more relevant than the other is difficult without flow characterization, but this thesis serves to highlight some guidelines for future studies over the rough plates, which will include also Particle Image Velocimetry (PIV).
Over the *Aluminium* plates, the wide smooth spots are mainly affected by induced turbulence. In these regions the HT enhancement is low, with a maximum value in these areas of $Nu_r/Nu_s \approx 1.35$. Conversely, the roughness clusters have a higher HT enhancement in the region where the flow impact directly, but in some regions the value is even lower than the unity. This might highlight a flow separation induced by rough elements which in turns decrease the HT.
The *Inconel 939* plates, with an high relative roughness, present more regions where

the flow impacts directly. There are not wide smooth spots, but only little smooth spots between rough elements where the flow might behave as in a cavity, and the Nusselt enhancement value reaches a maximum of $Nu_r/Nu_s \approx 1.02$. Furthermore, the values of Nusselt enhancement are much higher than in the *Aluminium*. This might be related to a protrusion of rough elements in higher velocity regions. In fact, the maximum values for the Aluminium is around $Nu_r/Nu_s \approx 1.65$, while for the *Inconel 939* the maximum is $Nu_r/Nu_s \approx 4.60$.

Zooming in the region with highest HT enhancement in the *IN939* model, it can be noticed that there is an overhanging element that tends to create recirculation, and it is also the highest rough element over the entire surface. Here the value reaches $Nu_r/Nu_s \approx 4.60$.

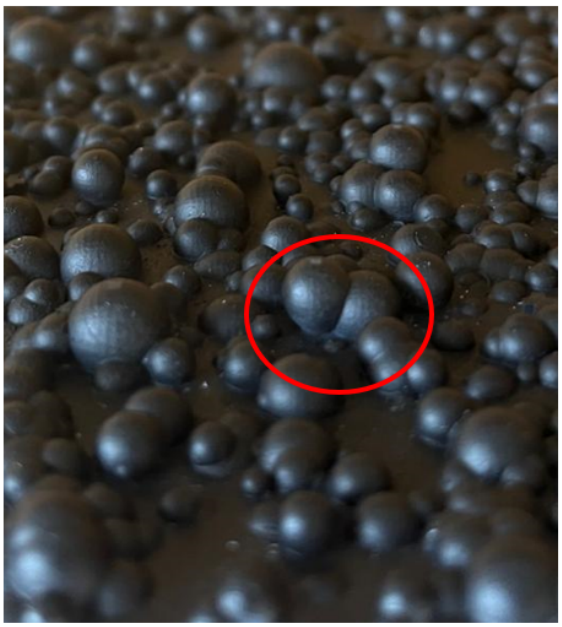

Figure 4.22: Rough element with highest HT enhancement over *IN939* plates

4.2.3 Comparison with the QSSHT rig

The QSSHT rig is used to test real size channels. The output of the QSSHT thermal tests is the global Nusselt for different Reynolds numbers of the channel with a given geometry and material, i.e. SR. In the present work, the results for the *Aluminium* test object, 90 mm long and with a $D_h = 1.53\ mm$, are compared with the upscaled model of the SRHT rig.
In Table 4.3 are found the results in terms of global Nusselt of the channel. For the SRHT rig, the global Nusselt $\overline{Nu_0}$ over the last window has been considered as the global Nusselt of the channel, since the channel is very short. The results align very well.

Re	***Nu QSSHT***	***Nu SRHT***
10000	38.36	33.14
15000	52.75	50.65
20000	64.14	69.63
25000	74.47	78.45

Table 4.3: Comparison between QSSHT and SRHT rigs

Chapter 5

Conclusions and Future Work

In this chapter the conclusions of the present work are drawn as long as the presentation of future work.

5.1 Conclusions

A rough surface model for *Aluminium* has been developed, with the main hypothesis of spherical rough elements. This has been done using the statistical distribution of spheres diameters, picked up from SEM images, spheres density, and vertical position as input of a macro in *Siemens NX*. The first model in output is representative of three main roughness parameters: R_a, R_z and R_q. A second model has been developed to match R_{sk} and R_{ku}. The last step on this subject has been to develop an optimization algorithm based on GA to try optimizing the sphere's vertical position in order to match all the SR parameters.
The smooth channel and the *Aluminium* roughness model have been tested at a flow temperature of $T_{\infty_{inlet}} = 70°C$ for four different Reynolds number, i.e. $Re = 10000$, $Re = 15000$, $Re = 20000$ and $Re = 250000$. The HTC and Nusselt number have been locally determined through IR thermography and two different solvers, based on smooth or rough channel. Overall, the achieved results can be summed up as follows:

- The **smooth channel** has been thermally characterized for all the different flow conditions. The laterally averaged Nusselt has been plotted along the dimensionless streamwise coordinate. The Nusselt value in the last window, which is considered to be in the thermally fully developed region, has been compared with the Gnielinski's correlation for smooth channels in order to validate the results. On this matter, the highest error with respect to Gnielinski is around 20%, which stands within the 25% uncertainty of the correlation.

Thus the channel is validated. Furthermore, the entrance region effect has been highlighted, showing the decreasing Nusselt along the channel.

- The **Aluminium roughness model** has been thermally characterized. It has been compared with *Inconel 939* roughness model and the smooth channel to understand how an increased relative roughness determines an higher HT. The *Inconel 939* showed higher Nusselt levels with respect to *Aluminium* and the smooth channel. The main effects in HT enhancement has been discussed focusing on turbulence and direct impact of air on the rough elements. The main reason for HT enhancement has been identified on the direct impact of air in the rough elements.

- **Comparison with QSSHT rig**: the results for the SRHT rig have been compared with the QSSHT rig. This gives an idea on how the real size channel results align with the results of the upscaled rough surface model. In the current work the *Aluminium* rough surface model align very well with the real size *Aluminium* channel.

5.2 Future Work

For the future, it will be important to investigate the flow characteristics over the rough surface models in order to determine the main effect of HT enhancement. So far, the direct impact has been considered as the main reason, but more insights can be seen from the PIV-rig that has been built in the *Fluid Dynamics Laboratory*. The flow characteristics could be the vortices generated downstream rough elements, turbulence characterisation, the presence of secondary flows in the channels, etc... It will also be interesting to understand what kind of material characteristics, or parameter, is more responsible for HT enhancement. Might it be the skewness R_{sk}, R_a, or other features that will come up in the future.

Bibliography

[1] Hannah Ritchie, Pablo Rosado, and Max Roser. "Energy Production and Consumption". In: *Our World in Data* (2020). https://ourworldindata.org/energy-production-consumption.

[2] Energy Institute. "Statistical Review of World Energy". In: (2023). URL: https://www.energyinst.org/statistical-review.

[3] IEA. *World Energy Outlook 2022*. IEA, 2022. URL: https://www.iea.org/reports/world-energy-outlook-2022.

[4] Professor Lakshmi Kantha Curt Hanson. "Land Based Gas Turbine for Power Generation". In: *ASEN 5063* (2009).

[5] Meherwan P. Boyce. *Gas Turbine Engineering Handbook*. Gulf Professional Publishing, 2006.

[6] Guohua ZHANG et al. "Optimization of cooling structures in gas turbines: A review". In: *Chinese Journal of Aeronautics* 35.6 (2022), pp. 18–46. ISSN: 1000-9361. DOI: https://doi.org/10.1016/j.cja.2021.08.029. URL: https://www.sciencedirect.com/science/article/pii/S1000936121003289.

[7] *Additive Manufacturing for the Manufacture of Gas Turbine Engine Components: Literature Review and Future Perspectives*. Vol. Volume 6: Ceramics; Controls, Diagnostics, and Instrumentation; Education; Manufacturing Materials and Metallurgy. Turbo Expo: Power for Land, Sea, and Air. June 2018, V006T24A021. DOI: 10.1115/GT2018-76686. URL: https://doi.org/10.1115/GT2018-76686.

[8] Dirk Herzog et al. "Additive manufacturing of metals". In: *Acta Materialia* 117 (2016), pp. 371–392. ISSN: 1359-6454. DOI: https://doi.org/10.1016/j.actamat.2016.07.019. URL: https://www.sciencedirect.com/science/article/pii/S1359645416305158.

[9] Mohammadreza Kadivar, David Tormey, and Gerard McGranaghan. "A review on turbulent flow over rough surfaces: Fundamentals and theories". In: *International Journal of Thermofluids* 10 (2021), p. 100077. ISSN: 2666-2027. DOI: https://doi.org/10.1016/j.ijft.2021.100077. URL: https://www.sciencedirect.com/science/article/pii/S266620272100015X.

[10] Ludwig Prandtl. "Turbulenz und ihre Entstehung". In: *J. Aeronaut. Res. Inst* 65 (1930).

[11] Th. von Kármán. "Mechanische Aenlichkeit und Turbulenz". In: *Nachrichten von der Gesellschaft der Wissenschaften zu Göttingen, Mathematisch-Physikalische Klasse* 1930 (1930), pp. 58–76. URL: http://eudml.org/doc/59299.

[12] N Darcy. "Recherches experimentales relatives au mouvement de l'eau dans des tuyaux". In: *Mem. savants etrangers Acad. Sci. Inst. Fr.* 15 (1858), p. 141.

[13] J. Nikuradse. "Strömungsgesetze in rauhen Rohren". In: 1933. URL: https://api.semanticscholar.org/CorpusID%3A232667976.

[14] C. F. Colebrook and C M White. "Experiments with Fluid Friction in Roughened Pipes". In: *Proceedings of The Royal Society A: Mathematical, Physical and Engineering Sciences* 161 (1937), pp. 367–381. URL: https://api.semanticscholar.org/CorpusID:136598986.

[15] Lewis F. Moody. "Friction Factors for Pipe Flow". In: *Journal of Fluids Engineering* (1944). URL: https://api.semanticscholar.org/CorpusID:254712400.

[16] J. P. Bons. "A Review of Surface Roughness Effects in Gas Turbines". In: *Journal of Turbomachinery* 132.2 (Jan. 2010), p. 021004. ISSN: 0889-504X. DOI: 10.1115/1.3066315. eprint: https://asmedigitalcollection.asme.org/turbomachinery/article-pdf/132/2/021004/5754570/021004_1.pdf. URL: https://doi.org/10.1115/1.3066315.

[17] Yi Zhu et al. "On friction factor of fluid channels fabricated using selective laser melting". In: *Virtual and Physical Prototyping* 15.4 (2020), pp. 496–509. DOI: 10.1080/17452759.2020.1823093. eprint: https://doi.org/10.1080/17452759.2020.1823093. URL: https://doi.org/10.1080/17452759.2020.1823093.

[18] Hamidreza Rastan et al. "Heat transfer study of enhanced additively manufactured minichannel heat exchangers". In: *International Journal of Heat and Mass Transfer* 161 (2020), p. 120271.

[19] Logan Tecson and Stephen T McClain. "Modeling of realistic ice roughness element distributions to characterize convective heat transfer". In: *5th AIAA Atmospheric and Space Environments Conference*. 2013, p. 3059.

[20] John-Mark Clemenson, Timothy A Shannon, and Stephen T McClain. "A Novel Method for Constructing Analog Roughness Patterns to Replicate Ice Accretion Characteristics". In: *2018 Atmospheric and Space Environments Conference*. 2018, p. 3015.

[21] ES Gadelmawla et al. "Roughness parameters". In: *Journal of materials processing Technology* 123.1 (2002), pp. 133–145.

[22] Karen A Flack and Michael P Schultz. "Review of hydraulic roughness scales in the fully rough regime". In: (2010).

[23] David R Hanson et al. "Flow in a scaled turbine coolant channel with roughness due to additive manufacturing". In: *Turbo Expo: Power for Land, Sea, and Air*. Vol. 58653. American Society of Mechanical Engineers. 2019, V05BT21A004.

[24] Curtis K Stimpson et al. "Roughness effects on flow and heat transfer for additively manufactured channels". In: *Journal of Turbomachinery* 138.5 (2016), p. 051008.

[25] Curtis K Stimpson et al. "Scaling roughness effects on pressure loss and heat transfer of additively manufactured channels". In: *Journal of Turbomachinery* 139.2 (2017), p. 021003.

[26] Lehmann Patrick. "Investigation of the local heat transfer characteristics on additively manufactured surfaces using infrared thermography". Technical Universitu of Munich, 2023.

[27] Kaibin Wen. "Investigation of Roughness Effects on Heat Transfer of Upscaled Additively Manufactured Channels in the Turbulent Region Using Infrared Thermography". KTH Royal Institute of Technology, 2023.

[28] Saravanamuttoo. *Gas Turbine Theory*. Pearson, 1951.

[29] Md Mustafizur Rahman et al. "Influence of operation conditions and ambient temperature on performance of gas turbine power plant". In: *Advanced Materials Research* 189 (2011), pp. 3007–3013.

[30] Anhay Vir Singh and Ravi Ranjan Singh. "Turbine blade cooling techniques". In: *International Journal of Research in Aeronautical and Mechanical Engineering* (2010).

[31] J. B. Young and J. H. Horlock. "Defining the Efficiency of a Cooled Turbine". In: *Journal of Turbomachinery* 128.4 (Mar. 2006), pp. 658–667. ISSN: 0889-504X. DOI: 10.1115/1.2218890. eprint: https://asmedigitalcollection.asme.org/turbomachinery/article-pdf/128/4/658/6930526/658_1.pdf. URL: https://doi.org/10.1115/1.2218890.

[32] Je-Chin Han. "Turbine Blade Cooling Studies at Texas AM University: 1980-2004". In: *Journal of Thermophysics and Heat Transfer - J THERMOPHYS HEAT TRANSFER* 20 (Apr. 2006), pp. 161–187. DOI: 10.2514/1.15403.

[33] Peter Ajersch. "Detailed measurements on a row of jets in a crossflow : With applications". PhD thesis. Apr. 1995. DOI: 10.14288/1.0081025.

[34] Sumanta Acharya and Yousef Kanani. "Chapter Three - Advances in Film Cooling Heat Transfer". In: ed. by Ephraim M. Sparrow, John P. Abraham, and John M. Gorman. Vol. 49. Advances in Heat Transfer. Elsevier, 2017, pp. 91–156. DOI: https://doi.org/10.1016/bs.aiht.2017.10.001. URL: https://www.sciencedirect.com/science/article/pii/S0065271717300059.

[35] Syed A.M. Tofail et al. "Additive manufacturing: scientific and technological challenges, market uptake and opportunities". In: *Materials Today* 21.1 (2018), pp. 22–37. DOI: https://doi.org/10.1016/j.mattod.2017.07.001. URL: https://www.sciencedirect.com/science/article/pii/S1369702117301773.

[36] Abbas Razavykia et al. "An Overview of Additive Manufacturing Technologies—A Review to Technical Synthesis in Numerical Study of Selective Laser Melting". In: *Materials* 13.17 (2020). ISSN: 19961944. DOI: 10.3390/ma13173895. URL: https://www.mdpi.com/1996-1944/13/17/3895.

[37] Lishi Jiao et al. "Femtosecond Laser Produced Hydrophobic Hierarchical Structures on Additive Manufacturing Parts". In: *Nanomaterials* 8 (Aug. 2018), p. 601. DOI: 10.3390/nano8080601.

[38] *EOS M 400 Series Production Platform for Additive Manufacturing of High Quality Metal Parts*.

[39] Theodore L Bergman. *Fundamentals of heat and mass transfer*. John Wiley & Sons, 2011. ISBN: 0470504811.

[40] Brunello P. *Lezioni di Fisica Tecnica*. Edises, 2017. ISBN: 9788879599436.

[41] Jürgen Zierep. "Similarity laws and modeling". In: (1971).

[42] *JEOL JSM-IT500*. https://www.jeol.com/products/scientific/sem/JSM-IT500.php.

[43] Yen Chi Chen. "Lecture 6 Density Estimation Histogram and Kernel Density Estimator". In: (2018).

[44] Frank Liebmann and Tom Kolat. "Exploration of alternative methods for fitting radiation thermometer signal to blackbody temperature". In: *Fluke Calibration, American Fork, Utah, USA. Accessed: Jan* 10 (2021).

[45] Krzysztof Dziarski and Arkadiusz Hulewicz. "Determination of Transmittance of IR Windows made of CaF2 within Operational Temperatures of Electric Devices". In: *Pomiary Automatyka Robotyka* 25.4 (2021).

[46] Thomas Opsahl. *The camera matrix P*. Lecture 5.1.

[47] Peter Jaksch. "Implementation of an adjoint thermal solver for inverse problems". In: *Proceedings of the 12th European Conference on Turbomachinery Fluid Dynamics & Thermodynamics, Stockholm, Sweden*. 2017, pp. 3–7.

[48] *NetScanner™ System 9116*. URL: `https://unisens.pl/en/product/254-9116-Netscanner?lang=en`.

[49] *Rosemount 2088 Absolute and Gage Pressure Transmitter*. URL: `https://www.emerson.com/documents/automation/product-data-sheet-rosemount-2088-absolute-gage-pressure-transmitter-en-73236.pdf`.

[50] DoE Metzger and DE Larson. "Use of melting point surface coatings for local convection heat transfer measurements in rectangular channel flows with 90-deg turns". In: (1986).

[51] AF Mills. "Experimental investigation of turbulent heat transfer in the entrance region of a circular conduit". In: *Journal of Mechanical Engineering Science* 4.1 (1962), pp. 63–77.

[52] Dawid Taler and Jan Taler. "Simple heat transfer correlations for turbulent tube flow". In: *E3S Web of conferences*. Vol. 13. EDP Sciences. 2017, p. 02008.

[53] Hugh W Coleman and W Glenn Steele. *Experimentation, validation, and uncertainty analysis for engineers*. John Wiley & Sons, 2018.

[54] Tom V Mathew. "Genetic algorithm". In: *Report submitted at IIT Bombay* 53 (2012).

Appendix

A Uncertainty Analysis

Nowadays, results cannot be presented without the uncertainty analysis, which allows to give a rough perspective of the error in the results. The previous colleagues have already accomplished such an ambitious task, and in the present work, the same approach will be followed, to obtain consistent results and give continuity to their work. In the first part some basic theory of errors will be described, followed by a second part where the methods and analysis will be presented.

A.A Introduction to UA

During experiments it is impossible to make perfect measurements. All the measurements of physical quantities are affected by inaccuracies. According to [53] there are two methods for evaluating inaccuracies encountered in experimental studies. One is the Monte Carlo Method (MCM) , which assumes different input variables distributions to get an output distributions with the related level of uncertainty. The second is the Taylor Series Method (TSM) , which is based on the calculation of the derivatives of the measured physical quantity with respect to the variables that influence the experiment, negleting higher order terms.

When measuring a physical quantity X we might not know the real value X_{real}. Moreover, trying to measure it, perturbations in the result are created, giving birth to an error. As a consequence, only the best estimate value X_{best} of that quantity can be given, while suggesting a certain level of error δ_x, which can tell the interval where the measurements are more likely to fall.

$$X = X_{best} \pm \delta_x \tag{A.1}$$

If several measurements are taken, the real value is supposed to be the best estimation. Yet, if the real value is not known there will always be a difference with the best estimation.

$$X_{real} \neq X_{best} \tag{A.2}$$

In case of several measurement, the best estimation is given by the average of the measurements

$$X_{best} = \overline{X} = \frac{\sum(X_i)}{N} \tag{A.3}$$

When only one measurement is done the best estimation is given by the measured value, and the error is given by the instruments inaccuracy.

The sources of error are divided in two main categories:

- Systematic errors: intrinsic to the measurement instruments which causes a bias in the estimation of the physical quantity. The only way to reduce them is to get more accurate instruments.
- Random errors: they are related to the operator of the experimental study, or the measurement instrument which has its own error. The approach to evaluate them is a statistic approach whenever the number of measurements is high.

The more variables influence the result, the more complicated is to calculate the error. In fact, the result is function of several quantities

$$X = X(\alpha_1, \alpha_2, \alpha_3, ...) \tag{A.4}$$

Every variable can bring an error, which will impact in the result. The evaluation of this errors can be done with one of the mentioned techniques.

A.B Uncertainties in HTC-Nu-Re

The method for uncertainties calculation was implemented by my previous colleagues in their thesis. In this case a brief recap of the problem will be presented as well as the uncertainty levels on the results. There is a slight difference between rough and smooth surfaces, because the presence of 3D rough elements necessitates the use of a thermal solver which introduces more inaccuracies.

A.B.1 Smooth Surfaces

For smooth surfaces the MCM method was chosen due to the high number of variable influencing the results. The contributions to the overall uncertainty is shown in the flowchart in Figure A.1. The HTC is indirectly calculated from Equation 3.22, thus the inaccuracies in the input quantities are responsible for the output's uncertainty. The inputs in 3.22 are material or gas properties , and directly and indirectly measured temperatures.

According to the MCM, given a physical quantity $X = X(\alpha_1, \alpha_2, \alpha_3, ..., \alpha_N)$ the objective is to set a probability density function for each of the N input variable. M iterations from each of the N distributions need to be done in order to get in output a representative PDF of the physical quantity. From the PDF in output the

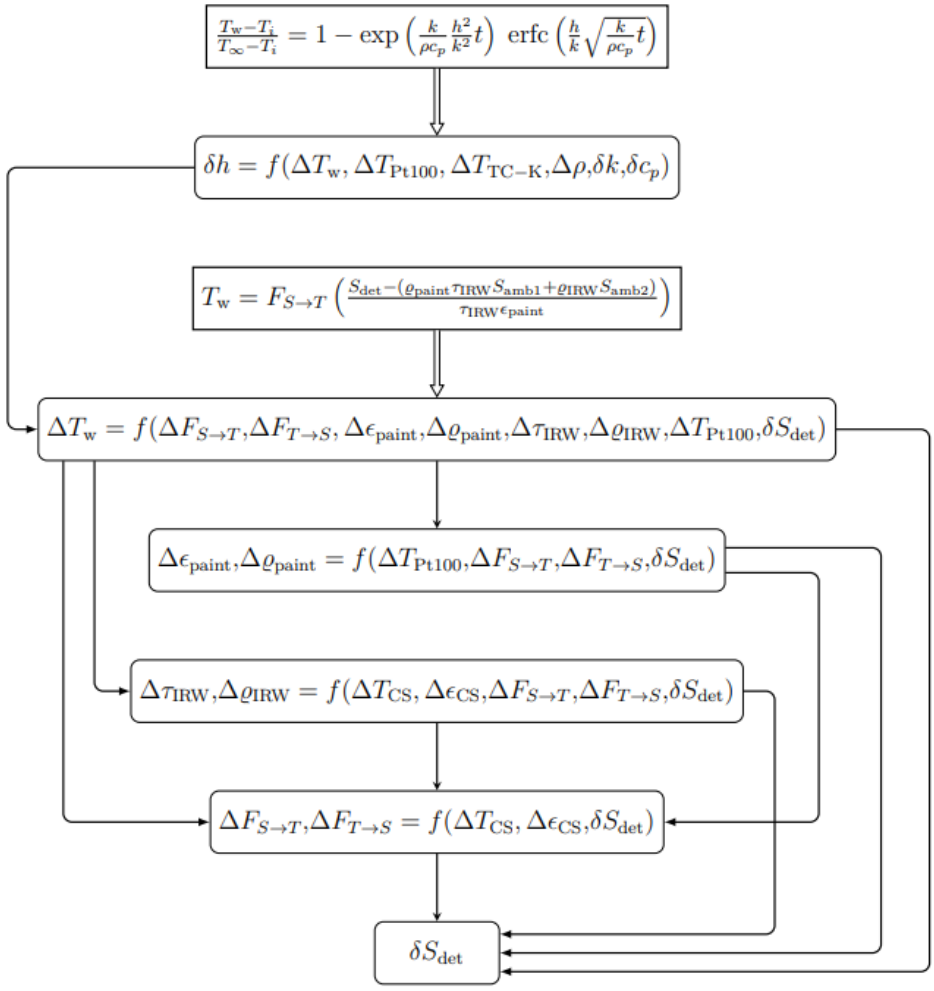

Figure A.1: Flowchart for uncertainty analysis

statistical quantities can be calculated: mean, standard deviation and the confidence level, usually taken as double of the standard deviation which is the region with 95% of the measured values. The final result will be always presented considering the standard deviation of the output distribution as the error, as in Equation A.5.

$$h = \overline{h} \pm \sigma \tag{A.5}$$

Considering the flowchart A.1, even if the main quantity is the HTC, the fundamental quantity that needs to be indirectly measured is the wall temperature uncertainty ΔT_w. Its calculation depends on several contributions: the correlation functions $\Delta F_{S\to T}$ and $\Delta F_{T\to S}$, the paint optical properties $\Delta\varepsilon_{paint}$, $\Delta\varrho_{paint}$ and the window optical properties $\Delta\tau_{IRW}$, ϱ_{IRW}. Moreover, the detected radiometric signal S_{det} has an inaccuracy of $\delta S_{det} = 1\%$ given by the IR Camera manufacturer.

The paint and window optical properties distributions are taken from Lehmann [26], and can be used as an input for the wall temperature uncertainty calculation. This

Property	μ [−]	2σ [−]	Rel. Uncertainty [%]
ε_{paint}	0.9072	0.0274	3.020
ϱ_{paint}	0.0540	0.0094	11.48
τ_{IRW}	0.9489	0.0334	3.412
ϱ_{IRW}	0.0501	0.0068	13.57

Table A.1: PDF properties for paint and IRW

distribution is then used for each Reynolds number and each window to solve the Equation 3.22 on the top of the flowchart. $M = 10^5$ iterations has been carried out for each position along the test section, picking up only the time history of the digital level of one pixel at the center of the region of interest. The resulting level of uncertainty δh, mean μ and confidence level 2σ of the output distributions are presented in Table A.2 and A.3.

Iterations = 10^5

	Re=10000			**Re=15000**		
Position	μ $\left[\frac{W}{m^2K}\right]$	$\mathbf{2\sigma}$ $\left[\frac{W}{m^2K}\right]$	$\delta\mathbf{h}$ [%]	μ $\left[\frac{W}{m^2K}\right]$	$\mathbf{2\sigma}$ $\left[\frac{W}{m^2K}\right]$	$\delta\mathbf{h}$ [%]
1	12.18	1.69	6.95	17.83	2.34	6.56
3	10.74	1.58	7.35	16.63	2.42	7.29
5	10.34	1.51	7.29	14.28	1.94	6.85
7	10.90	1.51	6.90	15.34	2.12	6.91
9	9.51	1.24	6.64	15.10	2.13	6.97

Table A.2: PDF properties and uncertainties for $Re = 10000$ and $Re = 15000$ at the various tested windows

Iterations = 10^5

	Re=20000			**Re=25000**		
Position	$\mu\ \left[\frac{W}{m^2K}\right]$	$\mathbf{2}\sigma\ \left[\frac{W}{m^2K}\right]$	$\delta\mathbf{h}\ [\%]$	$\mu\ \left[\frac{W}{m^2K}\right]$	$\mathbf{2}\sigma\ \left[\frac{W}{m^2K}\right]$	$\delta\mathbf{h}\ [\%]$
1	21.58	2.92	6.94	22.46	3.01	7.90
2	21.46	3.09	7.17	21.93	2.92	6.68
4	20.51	2.93	7.22	19.85	2.69	6.72
6	17.42	2.52	7.42	20.24	2.81	6.93
8	17.83	2.42	6.81	19.45	2.89	7.39

Table A.3: PDF properties and uncertainties for $Re = 20000$ and $Re = 25000$ at the various tested windows

A.B.2 Rough Surfaces

For rough surfaces the uncertainty depends on several factors, and a single method, such as the MCM, is not enough. In this case both the MCM and the TSM are used. If for the MCM the N variables influencing the physical measured quantities are set to be in a PDF, and the output PDF is calculated going through M iterations taking the input values from the variables PDF, for the TSM there is the need to calculate the variation of the output with respect to the influencing variables, i.e. the partial derivatives of the output with respect to the input. Once the derivatives are known, the result can be calculated with Equation A.6 , neglecting higher order elements.

$$\delta_x = \sqrt{\left(\delta\alpha_1 \frac{\partial X}{\partial \alpha_1}\right)^2 + \left(\delta\alpha_2 \frac{\partial X}{\partial \alpha_2}\right)^2 + ... + \left(\delta\alpha_N \frac{\partial X}{\partial \alpha_N}\right)^2} \tag{A.6}$$

In the course of this work the uncertainty of each variable is presented as U_i, i.e. $\delta\alpha_i = U_i$, so that

$$U_x = \sqrt{\left(U_1 \frac{\partial X}{\partial \alpha_1}\right)^2 + \left(U_2 \frac{\partial X}{\partial \alpha_2}\right)^2 + ... + \left(U_N \frac{\partial X}{\partial \alpha_N}\right)^2} \tag{A.7}$$

As we know from the theory presented in Section 3.4.2, the HTC for rough surfaces has been calculated using the thermal solver *C3D* which relies on the calibration of the wall temperature T_w over the model region of interest and the solving of an adjoint problem to calculate the *HTC*.
When following this process, it is fundamental to understand what influences the

result. For instance, from the adjoint problem 3.34 the HTC is only function of the mainflow temperature and the wall temperature

$$h = h(T_w, T_b) \tag{A.8}$$

Thus, the uncertainty in the HTC can be calculated starting from the uncertainties on these two variables using the TSM method:

$$U_h = \sqrt{\left(U_{T_w}\frac{\partial h}{\partial T_w}\right)^2 + \left(U_{T_b}\frac{\partial h}{\partial T_b}\right)^2} \tag{A.9}$$

The mainflow uncertainty is related to the Type-K thermocouple accuracy, which is given by the manufacturer and it's around $U_{T_b} = 1.1\ [K]$. Hence only the sensitivity with respect to the mainflow temperature has to be determined; this could be done by calculating the finite difference δh with different mainflow temperatures. For instance, by comparing two different windows, the sensitivity results in $\frac{\Delta h}{\Delta T_b} \approx \frac{\partial h}{\partial T_b} = -0.167$.

The process for the uncertainty evaluation on the wall temperature is slightly more complicated, since the influencing variables are a lot, and a MC analysis has to be carried out. For instance, the measured wall temperature uncertainty U_{T_w}, is function of the paint and the IR Window optical properties variation, but also of the correlation functions variation as in Equation A.10, as well as the calibration errors, which are measured as the root mean square of the temperature difference between the measured temperature and the *C3D* results.

$$T_w = T_w(\varrho_{paint}, \varepsilon_{paint}, \tau_{IRW}, \varrho_{IRW}, \Delta F_{S\to T}, S_{det}, S_{amb}) \tag{A.10}$$

The total uncertainty is calculated as the Euclidean norm of the MCM error and the C3D error:

$$U_{T_w} = \sqrt{(U_{T_w})^2_{MCM} + (U_{T_w})^2_{C3D}} \tag{A.11}$$

For each Reynolds number, the error in the calibration $(U_{T_w})_{C3D}$ is the average, among the tested windows, of the root mean square of the temperature difference between the measured and the numerically calculated ones.

On the other hand, to calculate the MCM uncertainty $(U_{T_w})_{MCM}$, for each Reynolds number and for each window, $M = 10^5$ iterations are carried out on the N input variables from Equation A.10. For a given Reynolds, the average of the root mean square over each window temperature distribution is taken as the total uncertainty $(U_{T_w})_{MCM}$.

Once the values of U_{T_w} for each Reynolds number are known, the last term to be calculated in Equation A.9 is the sensitivity of the HTC with respect to the wall

temperature. This can be accomplished by comparing the calibration of different windows and approximate $\frac{\Delta h}{\Delta T_w} = 0.442 \approx \frac{\partial h}{\partial T_w}$

B Genetic Algorithm to Optimize Roughness Modelling

The rough surface modelling has the objective of creating a surrogate model that matches the surface roughness parameters of the real surface. For instance, the five parameter found in Table 2.2 needs to be replicated to have the same fluid and thermal characteristics. Despite the effort in developing a procedure with such an ambitious result, none good model have been developed yet.
While creating models following the process in Section 3.1, a new method has been developed. This consist of an optimization algorithm base in GA, which tries to optimize the vertical position of the rough elements to match the surface roughness parameters. Before delving into the followed procedure, a short introduction of GAs is presented.

B.A Genetic Algorithms

GAs are computational models inspired by natural evolution [54]. The solution is encoded in chromosomes, which evolve preserving critical informations, to find an optimal solution. In this process, the natural selection takes place. Therefore, only the near optimal or optimal individuals survive in each lifecycle.
The main process followed by GAs can be summed up as follows:

1. **Initialization**: begin with a randomly generated population of chromosomes, each representing a pssible solution to the problem;

2. **Evaluation**: each chromosome is evaluated using a fitness function, which determines how good the solution is compared to others in the population;

3. **Selection**: chromosomes are selected for reproduction based on their fitness. Better solutions have a higher chance of being selected, simulating Darwin's principle of survival of the fittest.

4. **Crossover**: pairs of chromosomes are combined to produce new offspring. This is typically done by selecting a random crossover point and exchanging segments of the parent chromosomes. These variations such as one-site or two-site crossover depending on the problem's complexity.

5. **Mutation**: with small probability, random changes are introduced to the offspring's chromosomes to maintain genetic diversity and avoid local optima. This involves flipping bits in the chromosome's binary representation.

6. **New Generation**: the new population of chromosomes, which includes offpring from the crossover and mutation steps, replaces old population

7. **Iteration**: Steps 2 to 6 are repeated for a number of generations or until a satisfactory solution is found. Each iteration is called generation.

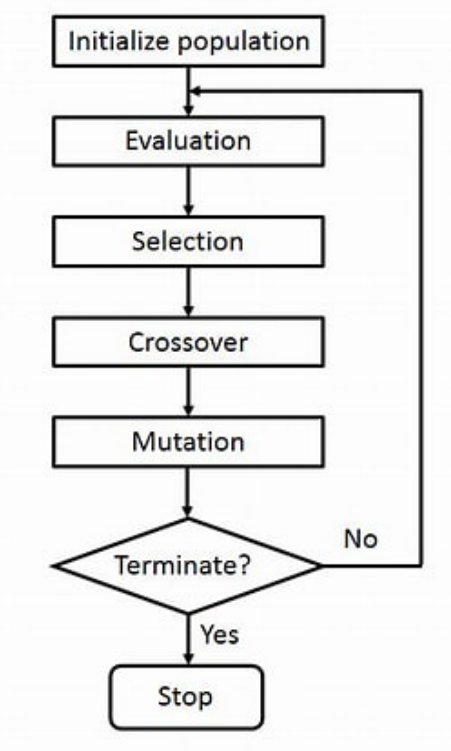

Figure B.1: GAs block diagram

B.B GAs for Surface Roughness Modelling

After a general description of GAs working principle, it is now important to link it with the procedure followed for the height optimization. The main hypothesis is that the rough elements are ideally spherical, which stems from SEM images. Following the presented steps for general GAs, and using *DEAP* library:

1. **Initialization**: the initial population are a set of individual, each given by spheres with fixed x, y position, diameters and density. The different individuals varies for the vertical position z of each sphere;

2. **Evaluation**: for each individual the surface roughness parameters are evaluated by using a *Python* code that simulates the experimental measurements. The 2D SR parameters are measured along five lines and the average parameters are calculated. The error between the real parameters and the ones for each individual are calculated and used to get a weighted relative error [1]. The fitness is then calculated as the ratio in Equation B.1

$$fitness = \frac{1}{1 + weighted\ relative\ err} \tag{B.1}$$

3. **Selection**: this is done using a tournament selection among a randomly chosen subset of the population. In each tournament, the individual with the highest fitness is selected. In this case only three individuals compete in each tournament;

4. **Crossover**: the crossover is done by swapping two segments of two different parents between two crossover points to create a new offspring;

5. **Mutation**: alters individual attribute by adding random values drawn from a Gaussian distribution with a specified mean and standard deviation, with a certain probability for each attribute;

6. **New Generation**: a new population is created from offspring and parents;

7. **Iterations**: the algorithm iterates for a given number of iterations and extracts the best individual.

[1] Weighted relative error: it consists in the sum of the relative error for each parameter multiplied by the desired weight (sum of the weights must be one)